



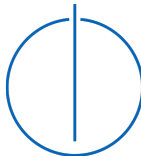
DEPARTMENT OF INFORMATICS

TECHNICAL UNIVERSITY OF MUNICH

Doktors der Naturwissenschaften (Dr. rer. nat.)

**Deep Learning Methods for Cardiac
Magnetic Resonance Imaging
Reconstruction**

Hossam El-Rewaidy



Deep Learning Methods for Cardiac Magnetic Resonance Imaging Reconstruction

Hossam Ahmed Mohammad Elrewaidy

Vollständiger Abdruck der von der Fakultät für Informatik der Technischen
Universität München zur Erlangung des akademischen Grades eines

Doktors der Naturwissenschaften (Dr. rer. nat.)

genehmigten Dissertation.

Vorsitzender:

Prof. Dr. Daniel Rückert

Prüfende der Dissertation:

1. Prof. Dr. Björn Menze
2. Prof. Dr. Mehdi Hedjazi Moghari

Die Dissertation wurde am 19.04.2021 bei der Technischen Universität München
eingereicht und durch die Fakultät für Informatik am 22.09.2021 angenommen.

*To my parents and family.
To all those who taught me good.*

ABSTRACT

Cardiovascular diseases are the leading cause of death worldwide, causing about 1 in 3 deaths. Cardiovascular Magnetic Resonance Imaging (MRI) is a valuable tool for non-invasive assessment of the function and structure of the cardiovascular system, with comprehensive tissue characterization and viability tests for the cardiac muscle. However, cardiac MRI is challenged by its inherent slow acquisition process, leading to long scan time, elevated scan cost, uncomfortable examination experience, and therefore limits its clinical utility. Several image reconstruction techniques were developed to accelerate MRI acquisition, however, most of these techniques (i.e. compressed-sensing and dictionary learning) are not yet fully adopted in the clinical workflow, as they require expensive processing time and resources. Recently, machine learning has emerged as an automatic method for many image processing tasks. In this thesis, we present novel techniques based on machine learning for fast reconstruction of the highly accelerated MRI acquisitions in different cardiac imaging protocols, such as late gadolinium enhancement (LGE), dynamic cine imaging, and myocardial T_1 mapping. To accelerate cardiac 3D LGE imaging, a complex-valued convolutional neural network (CNN) was utilized, in the first study, to preserve the complex nature of acquired MRI data throughout the entire reconstruction process and improve the reconstructed image quality. In the second study, to achieve high acceleration rates in dynamic cardiac imaging, a multi-domain CNN that processes the radial dynamic MRI data in the spatial-frequency, time, and image domains was developed. This network exploits the spatio-temporal correlations and k -space information sharing among neighboring time frames to enable high acceleration rates. In the third study, a rapid cardiac T_1 mapping technique based on neural networks was developed to allow accurate quantification of myocardial T_1 maps in a shorter breath-holding and scanning duration. The methods presented in this thesis demonstrate the ability of machine learning to accelerate cardiac MRI acquisition with minimal processing time and ultimately increase the clinical utility of cardiac MRI.

ZUSAMMENFASSUNG

Herz-Kreislauf-Erkrankungen sind weltweit die häufigste Todesursache und verursachen etwa 1 von 3 Todesfällen. Kardiale-Magnetresonanztomographie (MRT) ist ein wertvolles Werkzeug zur nicht-invasiven Beurteilung der Funktion und Struktur des Herz-Kreislauf-Systems, welche umfangreicher Gewebecharakterisierung und Viabilitätstestung des Herzmuskel ermöglicht. Das kardiale MRT wird jedoch durch seinen inhärenten langsamen Prozess der Bilderzeugung eingeschränkt, welche eine langsame Bilderfassung, erhöhte Bildgebungskosten, sowie eine unangenehme Untersuchungserfahrung für Patienten bedingt und dadurch zu einer Einschränkung der klinischen Anwendung führt. Mehrere Bildrekonstruktionstechniken wurden entwickelt, um die MRT-Erfassung zu beschleunigen. Die meisten dieser Techniken (z.B. "Compressed-Sensing" und Wörterbuchlernen) sind momentan jedoch nicht vollständig in den klinischen Ablauf integriert, da sie kostspielige Verarbeitungszeit und Ressourcen beanspruchen. Vor Kurzem wurde eine automatische Datenverarbeitungsmethode, das sogenannte "Deep Learning", entwickelt, welches in vielen Bildverarbeitungsaufgaben eingesetzt werden kann. In dieser Arbeit stellen wir mehrere neuartige Techniken vor, die auf dem besagten Deep Learning basieren und hochbeschleunigte MRT-Erfassung in verschiedenen kardialen Bildgebungsprotokollen, insbesondere in der verzögerten Gadolinium-Anreicherung (LGE), in der dynamischer Cine Bildgebung und in der Myokardialen T_1 -Kartierung, ermöglichen. Zum Zwecke der kardiale 3D-LGE-Bildgebung wurde in der ersten Studie ein komplexes konvolutionales neuronales Netzwerk (CNN) genutzt, welches ermöglichte die komplexe Natur der erfassten MRT-Daten während des gesamten Rekonstruktionsprozesses zu erhalten und die rekonstruierte Bildqualität zu verbessern. In der zweiten Studie wurde ein Multi-Domain-CNN entwickelt, das die radial-dynamischen MRT-Daten in den Raum-Frequenz-, Zeit- und Bilddomänen verarbeitet, um hohe Beschleunigungsraten in der dynamischen MRT-Bildgebung zu erreichen. Dieses Netzwerk nutzt die räumlich-zeitlichen Korrelationen und den Informationsaustausch zwischen benachbarten Zeitrahmen, um hohe Beschleunigungsraten zu erzielen. In der dritten Studie wurde eine schnelle kardiale T_1 -Kartierungstechnik auf Basis neuronaler Netzwerke entwickelt, um eine genaue Quantifizierung von Myokard- T_1 -Karten mit kürzerem Anhalten des Atems und einer verkürzten Scandauer zu ermöglichen. Die drei in dieser Arbeit vorgestellten Methoden demonstrieren insofern die Fähigkeit des Deep Learnings, die kardiale MRT-Erfassung durch Reduzierung der Daten-

verarbeitungszeit zu beschleunigen und letztlich so den klinischen Nutzen des kardialen MRT zu erhöhen.

ACKNOWLEDGEMENTS

During my PhD journey, I have met and worked with many passionate and talented colleagues who inspired me to be a better researcher. This dissertation would have not been possible without all the support and help I got from many friends to whom I have full gratitude and respect.

I would like to thank my mentor Prof. Reza Nezafat for his supervision and guidance during the course of my PhD. I am so grateful for the opportunity to join his diverse, talented, and multi-disciplinary group of researchers and for believing in my skills and capabilities to work independently and grow up in his lab. He has always motivated me to develop my skills and be a better researcher. I would like to express my sincere gratitude to my supervisor Prof. Bjoern Menze for his continuous support and invaluable guidance during my PhD. His support has made it possible for me to focus on my research and his discussions guided me through my PhD. Thanks to Prof. Dimitrios Karampinos for his support and supervision of my PhD.

I would also like to thank Dr. Ahmed Fahmy for being a great source of inspiration and endless support. I was so fortunate to work with him and learn from him before and after joining the PhD. I am deeply grateful to him for being the best teacher and for always being there for me when I needed help or advice. Big thanks to Dr. Ulf Neisius for teaching me a lot about clinical research and for his continuous support and help. It has been a great pleasure working with him. Thanks to Dr. Jihye Jang for introducing me to TUM and helping me with the PhD process at TUM. Her advice was precious. Thanks to all BIDMC lab members for their friendship and kindness. They were always supportive and a great source of joy and fun. Thanks to Julia Knuerr and Andrej Voss for their help with the administrative process during my PhD.

Thanks to all my friends everywhere who shared with me their life experiences and made my life in Boston easier. Special thank you to my friends Karim Osman, Dr. Walid Abdelmoula, and Dr. Haitham El-Marakeby for their support and for their discussions that helped me through the challenging times of my PhD.

Last but most importantly, I would like to express my sincere gratitude to my family for the unconditional love and support. Thanks to my mother, father, and siblings for the endless care and continuous encouragement that inspires me to succeed. Thanks to my Ngan for her love, care, and support.

CONTENTS

Abstract	v
Zusammenfassung	vii
Acknowledgements	ix
1 Introduction	1
1.1 Problem Statement	1
1.2 Thesis Contribution	2
1.3 Thesis Outlines	2
2 Background	5
2.1 Heart: Structure and Function	5
2.1.1 Cardiac Diseases	7
2.1.1.1 Dilated Cardiomyopathy (DCM)	7
2.1.1.2 Hypertrophic Cardiomyopathy (HCM)	8
2.1.1.3 Hypertensive heart disease (HHD)	8
2.2 Magnetic Resonance Imaging Principles	8
2.2.1 Magnetization	9
2.2.2 Resonance and Excitation	9
2.2.3 Relaxation	10
2.2.4 Image Acquisition	11
2.2.5 Image Formation	12
2.3 Magnetic Resonance Imaging Reconstruction	13
2.3.1 Sampling Trajectories	13
2.3.1.1 Cartesian Sampling	13
2.3.1.2 Non-Cartesian Sampling	13
2.3.2 Reconstruction methods	15
2.3.2.1 Partial Fourier	15
2.3.2.2 Parallel Imaging	15
2.3.2.3 Compressed Sensing	17
2.3.2.4 Dictionary learning	18
2.3.2.5 Deep Learning	19

2.4	Cardiovascular Magnetic Resonance Imaging	20
2.4.1	Cine Imaging.	20
2.4.2	Late Gadolinium Enhancement Imaging.	22
2.4.3	Myocardial T_1 Mapping	22
3	Deep Complex Convolutional Network for Fast Reconstruction of 3D Late Gadolinium Enhancement Cardiac MRI	25
3.1	Introduction.	29
3.2	Methods.	29
3.2.1	Network Architecture	30
3.2.1.1	Complex Convolutional Layer:	30
3.2.1.2	Radial Batch Normalization Layer:	30
3.2.1.3	Down-sampling and Up-sampling Layers:	32
3.2.1.4	Complex Activation Function:	32
3.2.2	Image Acquisition and Pre-processing	32
3.2.3	Network Training	34
3.2.4	Experimental Evaluation	34
3.2.5	Data Analysis	34
3.3	Results.	35
3.4	Discussion.	36
3.5	Conclusion	40
3.6	Supporting Information.	42
4	Multi-Domain Convolutional Neural Network (MD-CNN) For Radial Reconstruction of Dynamic Cardiac MRI	45
4.1	Introduction.	49
4.2	Methods.	49
4.2.1	Network architecture	49
4.2.1.1	K-space subnetwork	49
4.2.1.2	Image domain subnetwork	50
4.2.2	Data acquisition.	50
4.2.3	Data preparation	51
4.2.4	Network training	52
4.2.5	Performance evaluation.	52
4.2.6	Data analysis	53
4.3	Results.	53
4.4	Discussion.	56
4.3	Conclusion	59
4.4	Supporting Information.	61

5	Neural Networks for Accelerating Myocardial T_1 Mapping	63
5.1	Introduction	64
5.2	Methods	65
5.2.1	MyoMapNet T_1 Mapping.	65
5.2.2	Numerical Simulation	65
5.2.3	In-vivo data	67
5.2.4	T_1 Estimation in MyoMapNet	69
5.2.5	MyoMapNet Training	69
5.2.6	MyoMapNet Evaluation	70
5.2.7	Data analysis.	70
5.3	Results	73
5.3.1	Network optimization	73
5.3.2	Numerical Simulations.	74
5.3.3	In-vivo Studies	74
5.3.4	T_1 Map Reconstruction Time	76
5.4	Discussion	77
5.5	Conclusion	80
6	Discussion and Conclusions	81
7	Outlook	85
	References	89
	References	89
	List of Figures	107
	List of Tables	115
	List of Publications	117

1

INTRODUCTION

1.1. PROBLEM STATEMENT

CARDIOVASCULAR diseases are the leading cause of mortality worldwide with 17.9 million deaths (32.1%) in 2015 [1]. Cardiovascular Magnetic Resonance Imaging (MRI) is a valuable non-invasive tool for assessing the cardiac morphology, function, viability, and tissue characterization with a major clinical rule in the diagnosis of several cardiac diseases [2, 3]. However, Cardiac MRI is challenged by its slow acquisition process which causes long scan time, elevated scan cost, uncomfortable examination experience, and less availability to more patients in need. Several techniques were developed to reconstruct cardiac images from undersampled MRI acquisitions such as partial Fourier, parallel imaging, compressed sensing, and dictionary learning. Partial Fourier and parallel imaging techniques are widely adopted in current clinical protocols, although they can achieve limited acceleration rates. On the other hand, current compressed-sensing and dictionary learning techniques can enable higher acceleration rates but require expensive processing times and resources. Recently, machine learning and artificial intelligence-based techniques were developed to allow the reconstruction of MR images from highly accelerated acquisitions in minimal processing time.

1.2. THESIS CONTRIBUTION

The main goal of this thesis is to present novel deep learning-based techniques for fast reconstruction of highly accelerated MR acquisitions of the heart. This thesis presents and investigates multiple deep neural network-based architectures to accelerate different cardiac MRI modalities such as 3D late gadolinium enhancement, dynamic cine cardiac imaging, and myocardial T_1 mapping, with comprehensive quantitative and qualitative validations to evaluate the performance of these methods by the clinical standards.

In the first study, a deep complex-valued convolutional neural network (CNN) was developed to reconstruct 3D late gadolinium enhancement cardiac MR image from undersampled acquisitions of up to an acceleration rate of 8 with a substantial reduction in processing time compared to compressed-sensing methods. This complex-valued network preserves the complex nature and optimal combination of real and imaginary components of MRI data throughout the entire reconstruction process. It utilizes complex-valued convolutional layers, novel radial batch normalization, and complex activation function layers to learn rich representations of the MR data. This study investigates this family of networks in comparison to the conventional real-valued networks to improve the reconstructed image quality and myocardial scar quantification as assessed by experienced cardiologists.

The second study extends the complex-valued CNN-based framework to build a multi-domain network that allows processing the MR data in the spatial-frequency, time, and image domains to achieve high acceleration rates (i.e. 14-folds) in radial dynamic cardiac imaging. This multi-domain network allows advanced data sharing strategies to learn spatio-temporal correlations among neighboring time frames and multi-coil data in both frequency and image domains. This study helps to understand the benefits of multi-domain processing in suppressing image-domain artifacts compared to image-domain-only networks and improving image quality compared to compressed-sensing techniques.

The last study presents a rapid myocardial T_1 mapping approach that uses neural networks (NN) to estimate voxel-wise myocardial T_1 and extracellular volume maps from T_1 -weighted images collected after a single inversion pulse over 4-5 heartbeats. This framework enables myocardial T_1 quantification in 4-5 heartbeats (i.e. compared to 11-12 heartbeats in standard techniques) with near-instantaneous map estimation time with similar accuracy and precision of standard modified look-locker inversion recovery myocardial T_1 mapping technique.

1.3. THESIS OUTLINES

This thesis is organized as follows:

Chapter 2 contains further introduction of the clinical and technical background relevant to the topics covered by this thesis.

Chapter 3 presents a deep complex convolutional neural network for fast reconstruction of 3D late gadolinium enhancement cardiac MRI.

Chapter 4 presents a multi-domain convolutional neural network (MD-CNN) for the radial reconstruction of dynamic cardiac MRI.

Chapter 5 presents a rapid myocardial T_1 mapping approach that uses neural networks (NN) to estimate voxel-wise myocardial T_1 and extracellular (ECV) from a reduced number of T_1 -weighted images (4-5 images) collected after a single inversion pulse.

Chapter 6 provides a summary and discussion of the studies presented in this thesis. In **Chapter 7**, conclusions and future work will be discussed.

2

BACKGROUND

2.1. HEART: STRUCTURE AND FUNCTION

THE heart is the main organ in the circulatory system with a muscular structure that is responsible for circulating the blood to the whole body [4]. The human heart has four chambers: right and left atria located at the upper part of the heart and are responsible for receiving blood into the heart, and right and left ventricles toward the bottom of the heart to pump blood back to the whole body (Figure 2.1). Among the different cardiac chambers, various cardiac conditions are manifested by alteration of left ventricular (LV) function, morphology, or pathophysiology [5]. LV walls are much thicker than that of the right ventricle with a more conical shape, and near oval cavity outline in the transverse section. The LV posterior wall is formed by the ventricular septum and LV free wall otherwise. Three distinct layers can be identified in the LV wall (Figure 2.2). The outermost layer is called epicardium (or visceral pericardium) and acts as a protective layer. Deeper to it is the myocardium, a muscular wall that contains blood vessels and nerves and is responsible for LV contraction. The myocardium consists of cardiac muscle cells (or cardiomyocytes) surrounded by the extracellular matrix. The innermost layer is called endocardium.

Cardiac function is the ability of the heart to fulfill the body demands of oxygenated blood and it can be assessed by measuring several cardiac parameters, such as ejection fraction, stroke volume ... etc. Assessing most of these parameters depends on measuring the LV myocardium and cavity sizes at the end-diastolic and end-systolic phases of

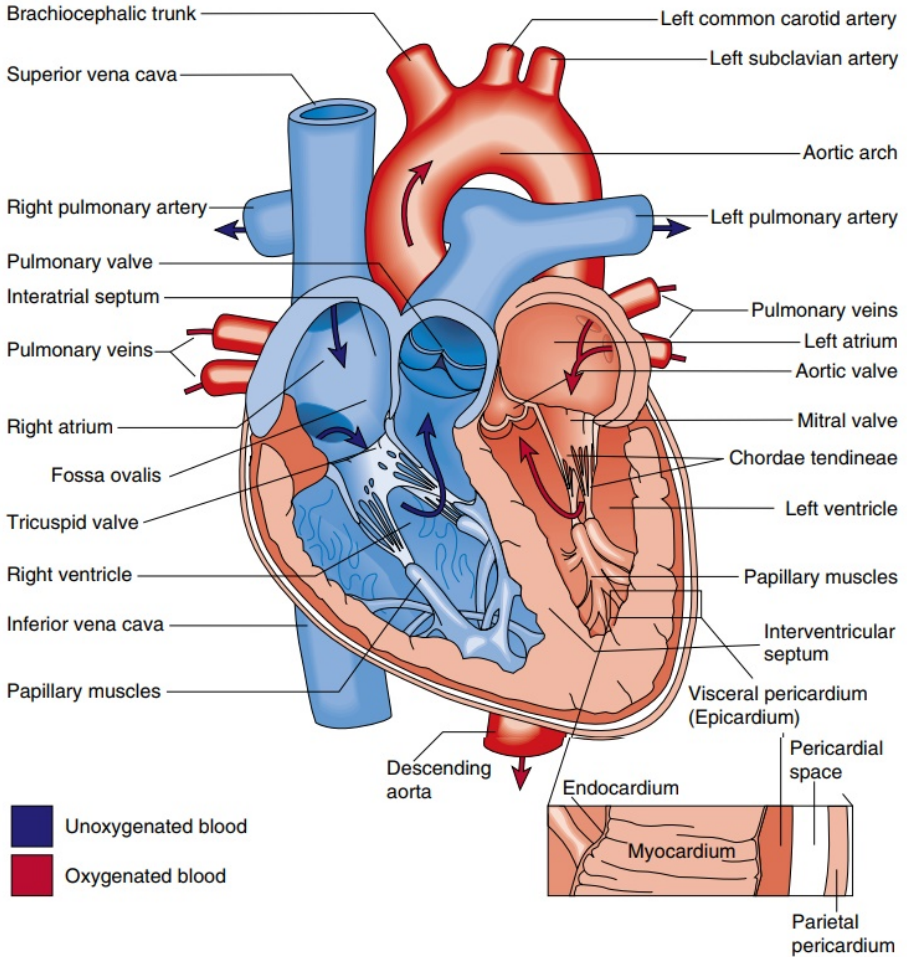


Figure 2.1: Heart structures [6].

the cardiac contraction. Different imaging modalities, such as Echocardiography, Computed Tomography, and Magnetic Resonance Imaging (MRI), . . . etc, are currently used for scanning the heart and measuring its different functional and morphological parameters. Cardiac MRI is the golden standard method for non-invasively measuring different cardiac parameters due to its excellent spatial and temporal resolutions and high reproducibility. The most important MRI protocols used to scan the heart are summarized in **section 2.2**.

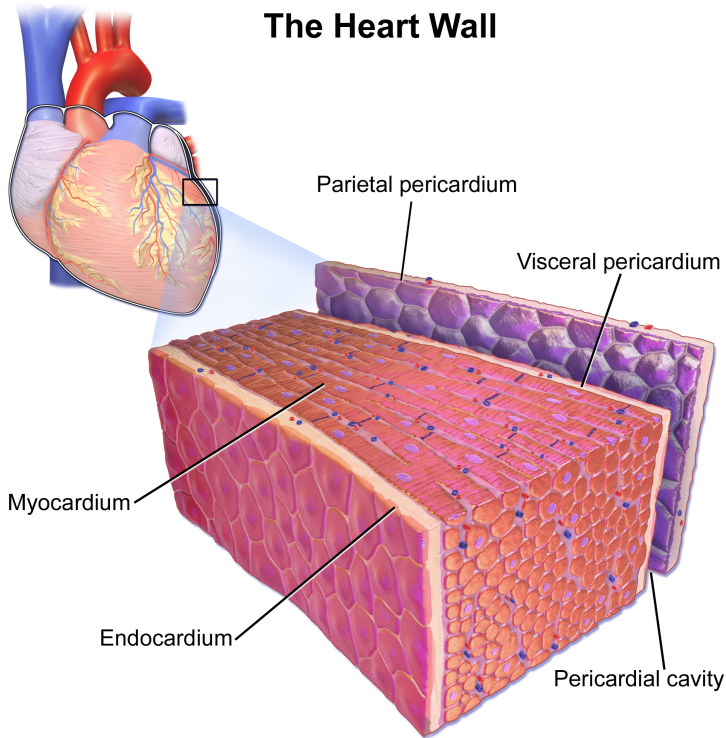


Figure 2.2: The heart wall [7].

2.1.1.1. CARDIAC DISEASES

Several types of heart diseases can alter the function, structure, or pathophysiology of the cardiac muscle [5]. Here are the details of a few diseases that are addressed in the coming chapters:

DILATED CARDIOMYOPATHY (DCM)

DCM is a common type of cardiac disease that affects the lower and upper chambers of the heart and occurs mostly in adults [8]. DCM is characterized by structural and functional abnormalities of the heart which can be manifested in enlargement and weakening of the LV muscle, limiting the heart's ability to pump blood to the body and can progressively affect the other heart chambers over time [8, 9]. Clinically, DCM patients are identified by a reduced ejection fraction of the LV (<45%) and an increase in LV diameter (>117%) [10, 11]. LV function and dimensions in DCM patients can be accurately assessed by cardiac MRI which is considered the gold standard method for left ventricular function and structure quantifications. In addition, other cardiac MRI modalities such as late gadolinium enhancement (LGE) [12–14] and interstitial diffuse fibrosis as-

assessment using myocardial T_1 mapping [15] play an important role in the prognosis of DCM-related adverse cardiac events.

HYPERTROPHIC CARDIOMYOPATHY (HCM)

HCM is the most common genetic disorder of the heart that affects the general population with an estimated prevalence of 0.16% to 0.29% [16] and is considered the leading cause of heart-related sudden death in the young generation. HCM is characterized by LV hypertrophy (i.e. increase in LV wall thickness unexplained by secondary causes such as systematic hypertension, valvular aortic stenosis, and infiltrative cardiomyopathies) and a non-dilated LV with preserved or increased ejection fraction [17, 18]. The cardiac MR cine imaging enables reproducible HCM diagnosis by identifying one or more hypertrophied segments (i.e. maximum LV wall thickness >15 mm) [19, 20]. Late gadolinium enhancement (LGE) also exists in 60% of HCM patients and is typically seen as a mid-wall pattern at hypertrophic areas of the LV myocardium, as well as right ventricular septal insertion point scars [21]. The LGE presence is suggestive of replacement fibrosis and is strongly correlated to the amount of collagen measured histologically [22]. Recent studies demonstrated an important rule for myocardial T_1 mapping imaging in quantifying and characterizing diffuse fibrosis content in HCM [23]. Results showed elevated T_1 values for HCM patients and a high correlation with the histological degree of fibrosis in HCM hearts [24].

HYPERTENSIVE HEART DISEASE (HHD)

HHD refers to a set of changes in the left ventricle, left atrium, and coronary arteries as a consequence of hypertension. Hypertension is a chronic blood pressure elevation that increases the workload of the heart causing functional and structural alterations in the myocardium such as LV hypertrophy. HHD patients can progress to heart failure and sudden cardiac death. HHD is defined as increased LV wall thickness (≥ 12 mm) [25] associated with the diagnosis of arterial hypertension [26] in the absence of severe chronic kidney disease, LV cavity dilatation, and cardiac disease that could result in a similar magnitude of hypertrophy (i.e. moderate-to-severe valvular heart disease, inherited/acquired cardiomyopathies). Cardiac MRI can provide a comprehensive evaluation of HHD, with an accurate and reproducible assessment of biventricular function, valvular disease, and stress myocardial perfusion [27].

2.2. MAGNETIC RESONANCE IMAGING PRINCIPLES

The human body is made of 80% water with two hydrogen atoms in each water molecule. MRI uses these hydrogen atoms to create contrast among different tissues based on their water content. Here is a detailed description of the MRI process:

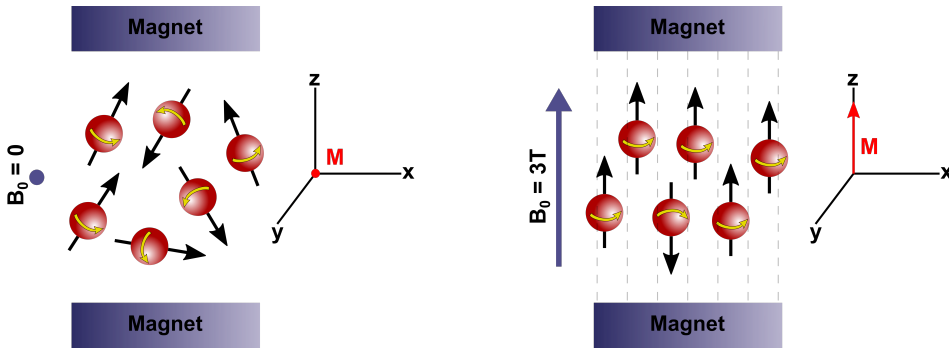


Figure 2.3: MRI Magnetization [28].

2.2.1. MAGNETIZATION

The nucleus of each hydrogen atom contains one positively charged proton that spins around its axis and produces a small magnetic field. Outside a magnetic field, these nuclei are randomly oriented with a net magnetization of zero. The MRI machine applies a strong magnetic field (B_0) to align these nuclei in the same direction as B_0 , producing a net magnetization of M_0 in the z-direction (parallel to the scanner bore) (Figure 2.3). This magnetization can be manipulated through physical and mathematical formulations to generate images [29].

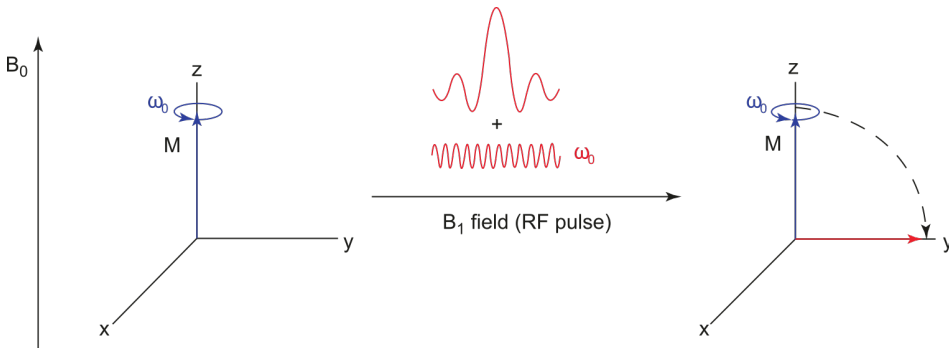


Figure 2.4: MRI Excitation [28].

2.2.2. RESONANCE AND EXCITATION

Due to gravitational forces and angular momentums, the spins forming the net magnetization vector precesses at an angular frequency called Larmor frequency (63.9 MHz in 1.5T magnet). To achieve magnetic resonance, MRI machines utilize radiofrequency (RF) pulses that match the Larmor frequency. Applying these RF pulses with specific

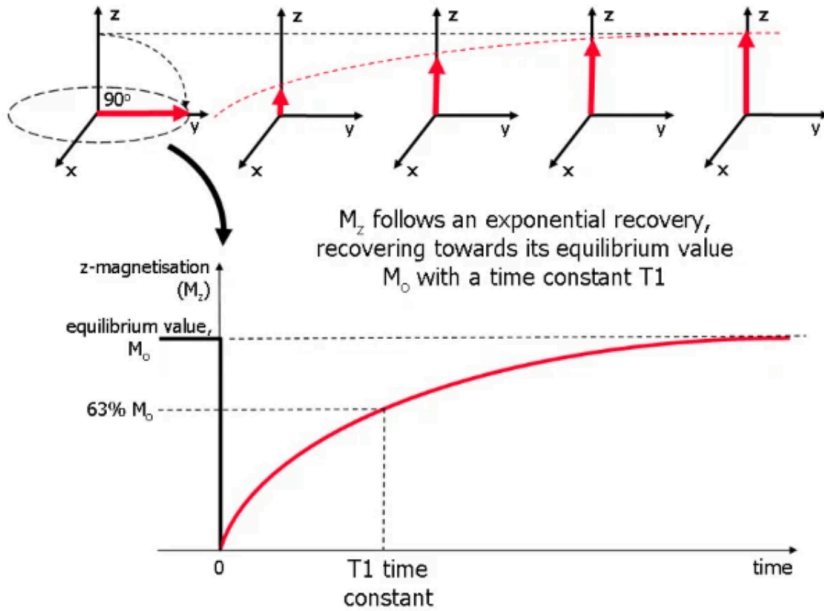


Figure 2.5: T_1 Relaxation [30].

amplitude and duration can precisely manipulate the net magnetization to be rotated in the transverse plane (in the x or y directions) with a specific flip angle (from 0 to 180 degrees). This process is called *excitation* (Figure 2.4).

2.2.3. RELAXATION

During the excitation process, the stimulated spins acquire energy from the applied RF pulse. Once the applied RF pulse is stopped, the spins start to return gradually to the equilibrium where the net magnetization is aligned again to the B_0 direction in a process called *relaxation*. Two independent types of relaxation are simultaneously taking place:

T_1 relaxation: refers to the recovering of the net magnetization in the direction of B_0 (z-direction). This type is called Spin-Lattice relaxation or Longitudinal relaxation. In this process, the energy gained from the RF pulse is dissipated in the lattice in form of increased rotation and heat. The T_1 relaxation follows an exponential growth process in the z-direction given by:

$$M(t) = M_0(1 - e^{-t/T_1}), \quad (2.1)$$

where $M(t)$ is the magnetization at time t , and M_0 is the maximum magnetization in the z-direction at a full recovery. T_1 is the time at which the signal is recovered to 63%

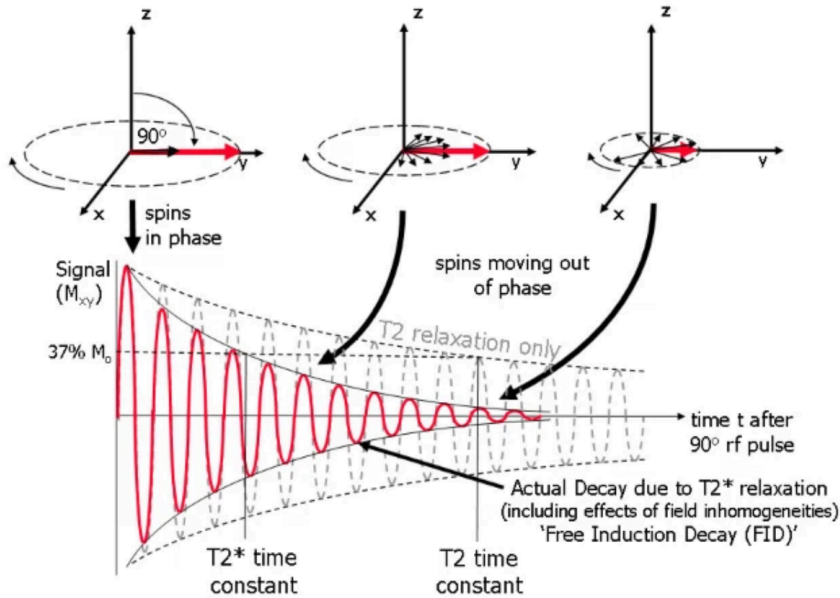


Figure 2.6: T_2 Relaxation [30].

of its maximum value M_0 (Figure 2.5). Different tissues have different T_1 times depending on their molecular structure, and therefore T_1 relaxation can be used to produce a contrast between different tissues in T_1 -weighted imaging.

T_2 relaxation: refers to the decay of the magnetization in the transverse direction and is called ‘spin-spin relaxation’. It takes place simultaneously but independent of the T_1 relaxation process. After applying the RF pulse, the simulated spins rotate to the transverse plane and spins in phase. Soon after RF transmission ends, the spins start to rotate at different rates due to direct interaction between the spins (Figure 2.6). Due to this effect, the signal in the transverse direction decays exponentially as a function of the T_2 time constant. The T_2 time also differs for different tissues and is used to create a contrast between different tissues in T_2 -weighted imaging.

2.2.4. IMAGE ACQUISITION

During relaxation, protons release their excess energy in the form of RF waves, which can be captured at each location of the x-y plane to create an image. In this process, the RF signal is spatially encoded using three gradient coils: G_x , G_y , and G_z . These gradients apply a variable magnetic field as a function of the position along the three directions x, y, and z, respectively. First, to determine a slice location in the z-direction, the slice gradient G_z is turned on during the excitation step, such that an RF pulse with a frequency

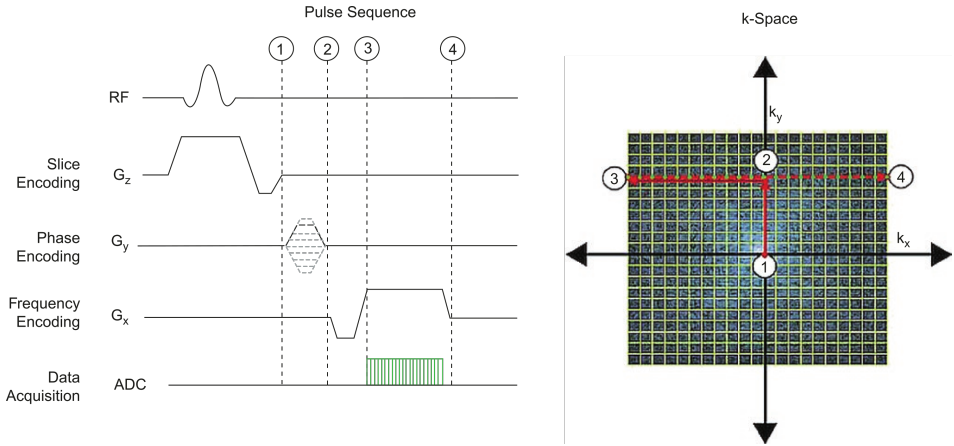


Figure 2.7: Image Acquisition [28].

corresponding to the slice location is applied. Similarly, the magnetization at each location in the x - y plane can be spatially encoded using the G_x and G_y gradients (Figure 2.7). The G_y gradient is turned on for short time to induce phase differences for each location in the y -direction (i.e. *phase encoding*). Subsequently, the G_x gradient is turned on to add frequency differences at each location in the x -direction (i.e. *frequency encoding*) while recording the signal at each location. This process is repeated for each line in the x - y plane to create a unique combination of phase and frequency at each voxel.

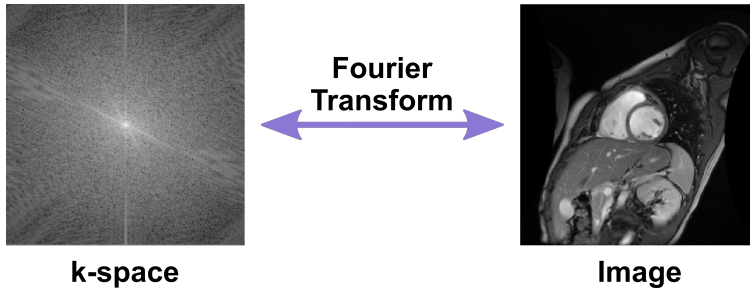


Figure 2.8: Image Reconstruction.

2.2.5. IMAGE FORMATION

The MRI raw data is acquired in a spatial frequency domain, called k -space, and typically requires multiple processing steps to be transformed into clinically useful images, in a process called *image reconstruction* (Figure 2.8).

2.3. MAGNETIC RESONANCE IMAGING RECONSTRUCTION

The image reconstruction is an important step that can critically impact the clinical use of MRI besides its significant role in accelerating the slow MRI acquisition process. This process involves a selection of sampling strategy and applying post-processing reconstruction techniques.

2.3.1. SAMPLING TRAJECTORIES

Reconstruction of MRI images starts with the selection of a sampling strategy for collecting the raw data. Cartesian and non-cartesian sampling trajectories were used for MR data acquisition (Figure 2.9) as follows:

CARTESIAN SAMPLING

The cartesian trajectory is the most widely adopted sampling method in the clinical imaging protocols due to its easy acquisition and reconstruction [29]. In cartesian sampling, the MR data are uniformly sampled line-by-line on the rectangular grid (k-space) which can be easily and quickly transformed into images using the inverse Fast Fourier Transform (FFT) [29, 31]. A typical Cartesian trajectory has equal space among lines on the k-space grid (Figure 2.9). A possible way to accelerate acquisition using cartesian sampling, variable-density cartesian trajectory with higher density at k-space center in the phase encoding direction. This acceleration results in aliasing artifacts in the phase encoding direction in the image domain. The degree of this aliasing is proportional to the acceleration rate of the undersampled k-space.

NON-CARTESIAN SAMPLING

Non-cartesian sampling allows a higher acceleration of MRI acquisition [29, 31]. Several non-cartesian sampling trajectories were used in MRI acquisition such as radial, spiral, ...etc. The radial trajectory consists of spokes that radiate out through the center of the k-space. Unlike cartesian sampling, radial sampling produces data points that do not fall into a rectangular matrix and requires further processing steps to estimate the k-space values on a rectangular matrix in a process called Gridding [33, 34]. In the gridding process, the non-uniform radially acquired data are interpolated at each location of the cartesian grid using a convolutional kernel [33, 35]. Reconstruction of radial acquisitions also involves some form of data weighting that accounts for the variable sampling density in the k-space [34–36]. The density compensation can be performed in the frequency domain directly by multiplying the acquired MR measurements with a weighting function [34, 35].

Radial sampling has several advantages such as rapid coverage of k-space, allow image contrast to be updated throughout data acquisition, and relative insensitivity to

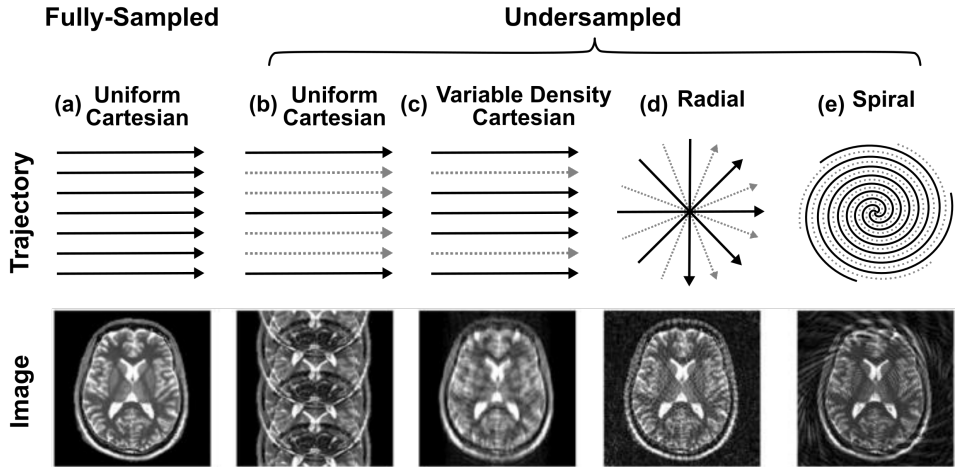


Figure 2.9: Examples of different cartesian and non-cartesian k-space trajectories. Solid and dotted trajectory arrows indicate the location of acquired and skipped k-space lines, respectively (a) Fully-sampled Cartesian trajectory and its corresponding artifact-free image (b) Uniformly undersampled Cartesian trajectory with an acceleration factor of $R=3$ produce coherent aliasing artifacts in the image domain. (c) Variable-density Cartesian sampling and the corresponding incoherent imaging artifacts. (d) Radial data can be undersampled by skipping radial spokes with streaking artifacts in the reconstructed image. (e) Spiral k-space undersampled by skipping spiral arms, which produces incoherent swirling artifacts [32].

motion artifacts [29, 37–39]. Unlike the fixed direction of phase-encoding in cartesian sampling, radial sampling has distributed phase-encoding directions across the whole images thus moving structures induced artifacts does not propagate as discrete ghosts along one phase-encoding direction [40]. Besides, the overlapping radial spokes at the k-space center contributes to the increased immunity of radial trajectories to motion artifacts due to the exploited redundancy of the signal at the center of the k-space. Additionally, radial sampling allows a higher acceleration of MR acquisition due to the equal contribution of each radial spoke to the image reconstruction, unlike cartesian sampling where the few lines across the center largely determine the image contrast and noise level. Finally, the image acquired using radial sampling was shown to have superior signal-to-noise ratios. For these reasons, radial acquisitions are fastly gaining ground in many applications that require highly accelerated acquisitions.

In dynamic cardiac MRI, each time frame can be acquired with a 2D radial trajectory (i.e. stack-of-stars) [41, 42]. Considering the periodic nature of dynamic cardiac imaging and similar structural information among successive time frames, radial views from neighbor frames can be utilized to provide a better estimation of k-space values at more locations on the Cartesian grid, and hence reduce the resulting streaking artifacts. To exploit information from different frames, the radial trajectory in each frame is rotated with some angle that maintains a uniform angular spacing among neighbor frames [43, 44].

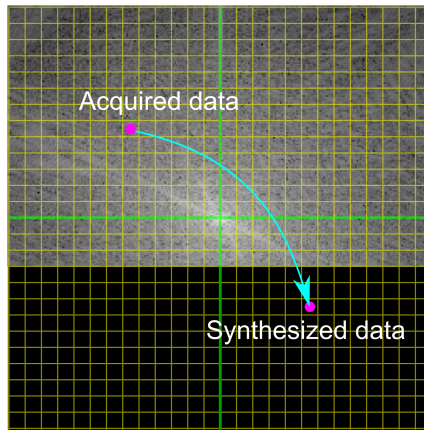


Figure 2.10: Partial Fourier.

Radial acquisition with rotating angles also produces incoherent artifact patterns across time frames. To enable higher acceleration rates for real-time applications, these incoherent signal variations can be exploited by reconstruction methods (e.g. compressed sensing) to remove residual undersampling artifacts from radial acquisition by minimizing the total variation across the time dimension [42].

2.3.2. RECONSTRUCTION METHODS

PARTIAL FOURIER

The partial Fourier imaging technique is one of the earliest methods to reconstruct MR images from accelerated acquisitions, which is based on the fact that the k-space contains redundant information when the imaged object is real [45, 46]. These techniques exploit the conjugate symmetry property of the k-space, in which, only one-half of the k-space is sufficient to reconstruct the whole MR image (Figure 2.10), assuming that no phase errors occur during data collection [47]. Although MR images are complex in nature, magnitude images are often displayed. Spatially dependent phase-shifts are usually produced in the k-space due to different spatial-domain effects such as radio-frequency phase shifts, flow, magnetic field (B_0) inhomogeneity [45]. Several methods were proposed to correct for phase-shifts in partial Fourier imaging in either of the image or spatial frequency domains, or both [45, 46].

PARALLEL IMAGING

In parallel imaging, MR data is acquired from multiple phased-array coil elements where each coil covers only a part of the field of view. Parallel imaging reconstruction methods utilize the redundancies in the multi-coil data to accelerate acquisition in k-space

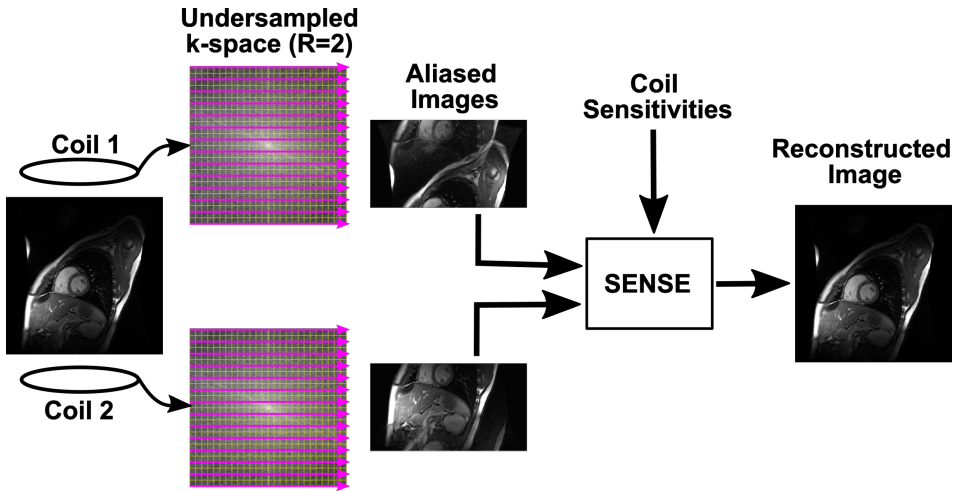


Figure 2.11: Parallel Imaging: SENSE reconstruction.

[48–51] or image domain [52] to reconstruct undersampled MR data. Two approaches are widely used in clinical protocols to reconstruct multi-coil data: sensitivity encoding (SENSE) and generalized autocalibrating partially parallel acquisition (GRAPPA) [48, 50].

In SENSE methods, the reconstruction is performed in the image domain by solving a linear inverse problem using the receiver coils sensitivities as recorded before the MRI scan (Figure 2.11) [50]. The coil sensitivity maps vary for different scans based on the relative position of the coil array to the heart and represent a determinant factor for the reconstructed image quality [32, 50, 53]. On the other hand, GRAPPA-based reconstruction methods operate in the k-space by utilizing shift-invariant convolutional kernels to estimate the missing k-space lines from the acquired ones [48]. In GRAPPA algorithms, the weights of these convolutional kernels are estimated from a small amount of fully-sampled reference data, commonly acquired at the center of the k-space and referred to as autocalibration lines (ACS) [48, 53].

While the parallel imaging reconstruction methods such as SENSE and GRAPPA were originally proposed for Cartesian sampling schemes, several modifications were developed to adapt these techniques for non-cartesian sampling trajectories [51, 52, 54, 55]. Although, non-cartesian parallel imaging utilizes the same concepts as Cartesian parallel imaging by taking advantage of redundant information from multiple coils to accelerate the image acquisition, applying such algorithms to non-cartesian undersampled data is more challenging [40]. For instance, non-cartesian sampling generates more complex aliasing artifacts that can complicate SENSE-type processing.

Other methods that combine features from SENSE and GRAPPA approaches were

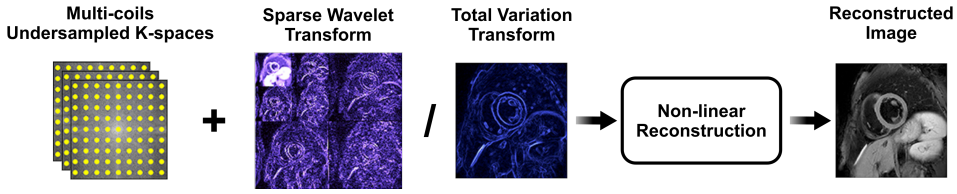


Figure 2.12: Compressed Sensing [58].

also proposed to accelerate parallel imaging acquisitions [49, 56, 57]. The iterative self-consistent parallel imaging (SPIRiT), like GRAPPA, recovers the missing k-space information using k-space kernels to exploit correlations between acquired k-space lines while framing the reconstruction process as an inverse problem in the image domain like SENSE. Additional constraints can be included in the iterative reconstruction process to improve the resulting image quality, commonly using spatial regularizations such as wavelets in l_1 -SPIRiT method [56].

COMPRESSED SENSING

Compressed (or compressive) sensing (CS) is a mathematical framework that allows reconstructing MR images from highly accelerated acquisition beyond the Nyquist criterion. CS exploits the sparsity (or compressibility) of the MR images in a transform domain (e.g. wavelet transform) to enable a high acceleration rate [59–61]. The full utility of the CS has three requirements: incoherent undersampling patterns, sparsifying transform, and non-linear optimization (Figure 2.12) [61]. The image-domain artifacts due to the k-space undersampling should be *incoherent* (noise-like) in a transform domain to allow easy separation from the true image data. Random k-space sampling schemes are often used in CS frameworks to generate incoherent image-domain artifacts. Although fully-random k-space sampling is impractical in MRI acquisition due to undesirable eddy current-induced artifacts, variable density pseudo-random sampling patterns are used in practice to allow better CS performance [61]. The MR images are also required to have sparse (or compressible) representation on a known transform domain to enable noise cancellation. The discrete wavelet transform is commonly used as a sparsifying domain in CS for many MR reconstruction applications. Finally, the MR images are iteratively reconstructed using a non-linear optimization framework that enforces the sparsity of image representations subject to data consistency constraints that maintain the fidelity of the acquired k-space data. Enforcing the sparsity is typically done by minimizing the convex l_1 norm of the transform domain coefficients.

CS-based reconstruction was applied in numerous cardiac MRI applications to reduce scan time, which can be traded off for improved spatial or temporal resolutions [62–65]. For instance, in dynamic cardiac imaging (i.e. 2D+t), the sparsity of MR data can

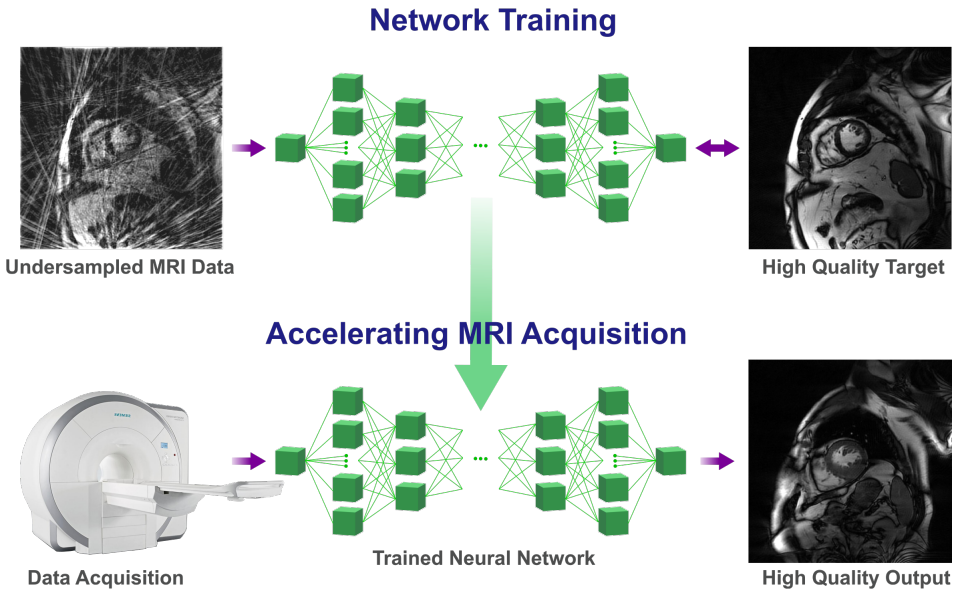


Figure 2.13: Deep neural networks for accelerating MRI acquisition.

be exploited in x-y space and time domain, which allows substantially higher accelerated acquisitions [61, 63, 64]. In addition, several methods were developed to combine parallel imaging and CS [66–68], via sparsity-regularized iterative GRAPPA-type approaches, or utilizing the coil sensitivity to enforce data consistency and sparsity constraints in a concurrent or series combination of CS and SENSE [67].

DICTIONARY LEARNING

The dictionary learning-based reconstruction methods extend the sparsifying transform concept employed in CS to adaptive transforms (or dictionaries) of learned representations from the data [69–72]. While the regular sparsifying transforms used in CS try to utilize the global sparsity of the MR data, dictionary learning methods utilize a local batch-based sparsity to capture local image features more effectively and potentially remove noise and aliasing artifacts without degrading resolution [70]. Most dictionary learning methods start with training adaptive dictionaries from image patches. In this step, a set of atoms (i.e. dictionary columns) are formed of image patches which can be then approximated by a sparse linear combination of these atoms. The K-Singular Value Decomposition (K-SVD) algorithm is commonly used to train adaptive dictionaries [73]. Similar to CS, several methods were developed to combine dictionary learning with a different parallel imaging method such as SPIRiT and l_1 SPIRiT [74, 75].

DEEP LEARNING

Deep artificial neural networks are a class of machine learning algorithms that have been successfully applied for MR image reconstruction tasks [76–81]. In deep learning frameworks, the MR data are processed via a series of cascaded layers of connected nodes that utilize thousands of trainable parameters to map the artifact-contaminated undersampled input data to artifact-free output (Figure 2.13). Deep learning models take the advantages of current increasing processing power, data availability, and advanced training approaches to automatically learn complex data representations and artifact patterns for fast reconstruction of MR data. During training, the learnable parameters in these models are automatically adjusted in an iterative fashion using an optimization algorithm (e.g. stochastic gradient descent, ADAM, ... etc.) to minimize a loss error for a given set of training data samples. These parameters approximate a mapping function between undersampled input and fully sampled output data which can be generalized to reconstruct new undersampled acquisitions and provide artifact-free MR data.

Several deep learning models have been investigated for image reconstruction tasks, such as Convolutional Neural Networks (CNN) [80, 82], Recurrent Neural Networks (RNN) [79], Generative Adversarial Networks (GAN) [83–85], ... etc. Deep CNN models utilize several layers of trainable parameters in form of convolutional kernels applied to the MR data in each layer. These kernels are automatically adjusted during training using shift-invariant convolution operations of the input data. To enable CNN to learn higher-order representations of the data, non-linearities are applied after each convolutional layer in form of activation functions. The rectified linear unit (ReLU) is the most common activation function which outputs zeros for negative inputs and is linear otherwise. Other architectures like RNN were used to unfold the reconstruction network into iterative-like states, in which the output of each state is fed as an input into the next state of the network [79]. RNNs also were used to reconstruct sequences of input, such as dynamic cardiac MRI, to share information among neighboring timeframes.

Both supervised and unsupervised neural networks were used to formulate MR image reconstruction problems. In supervised learning, the network is given a pair of images: artifact-contaminated data due to undersampled acquisition as input, and fully sampled versions as ground-truth for training [78, 85, 86]. In each iteration of supervised training, a loss function is calculated to minimize the error between the network output and the ground-truth data. The residual errors are used using the back-propagation algorithm to modify the network trainable parameters to minimize the overall errors over the entire training dataset. Two loss functions are commonly used in reconstruction problems: mean-squared error (l_2 loss) and mean absolute error (l_1 loss). On the other side, in unsupervised frameworks, neural networks are designed to infer structures of the input data without the need for ground-truth. The majority of proposed networks

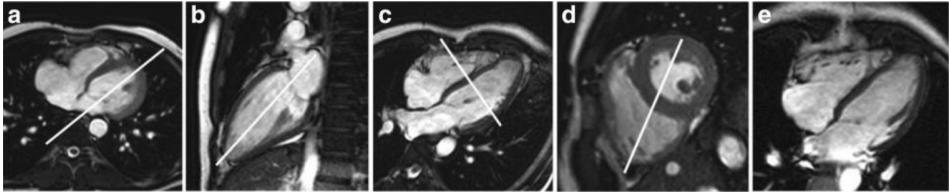


Figure 2.14: Cine imaging: (a) Axial plane. (b) Vertical long-axis plane. (c) Horizontal long-axis plane. (d) Short-axis plane. (e) Four-chamber plane [90].

for MR image reconstruction were framed as supervised networks. In addition, supervised and unsupervised deep learning methods were utilized to operate in the image space only, in k-space only, multiple domains as a direct mapping between k-space to image space, or unrolled optimization methods.

2.4. CARDIOVASCULAR MAGNETIC RESONANCE IMAGING

Cardiovascular Magnetic Resonance Imaging (or Cardiac MRI) is a powerful non-invasive imaging modality with a major clinical role in identifying cardiac diseases. Cardiac MRI is the gold standard for the practice of cardiology due to its high reproducibility and accuracy, wide field-of-view, and excellent soft-tissue contrast with high spatial resolution, which is superior to any other individual imaging modality [87]. Furthermore, cardiac MRI can provide a comprehensive cardiovascular assessment of a patient in a single sitting as it comprises several imaging protocols for assessment of cardiovascular morphology, ventricular function, tissue characterization, myocardial perfusion, flow quantification, and coronary artery disease [88, 89]. We will focus on cardiac MRI as the main imaging modality in this thesis.

Here is a summary of some modalities that are being used frequently in clinical practice and will be the focus of the next chapters:

2.4.1. CINE IMAGING

Cine imaging is the most common cardiac MRI technique to assess the cardiac morphology and quantifying global and regional left and right ventricular functional parameters (e.g. stroke volume, ejection fraction, end-diastolic and end-systolic volumes, and masses, ...etc) [91, 92]. In cine imaging, a full stack of cardiac images is acquired at different phases throughout the cardiac cycle and different cross-sections and positions of the heart, such as short-axial (SAX), 2, 3, and 4-chamber long-axial (LAX) views (Figure 2.14) [91].

The cardiac cine imaging is mainly challenged by the slow acquisition process of MRI which causes prolonged scan times. MRI is therefore limited when imaging a moving

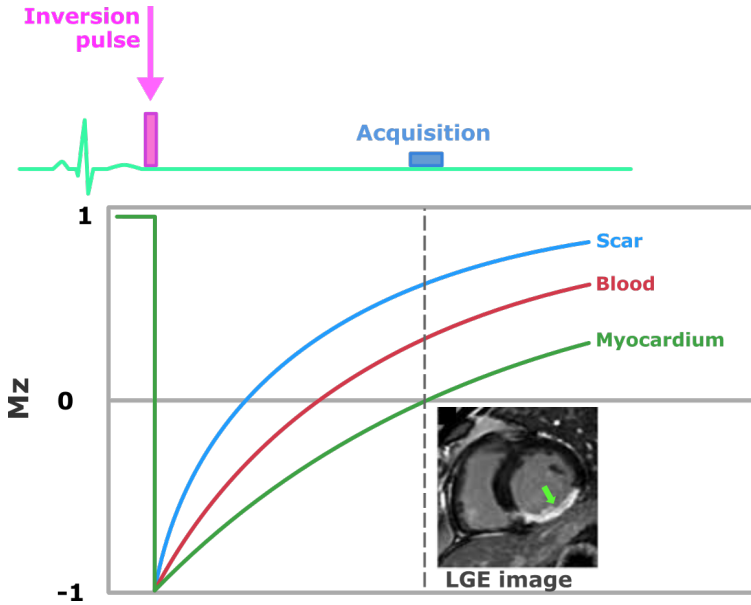


Figure 2.15: Myocardial Late Gadolinium Enhancement (LGE) sequence.

object like the heart, where the cardiac motion constitutes the major source of degradation and undesired effects in the reconstructed cine images, such as image blurring, ghosting, and misregistration due to alteration in the k-space data [93]. The overall cardiac motion is a combination of three sources: heart beating, respiratory-induced, and bulk patient motion. To minimize the motion effects due to heart beating, the cardiac cycle is split into small segments to represent different cardiac phases [94]. The ECG signal is then used to synchronize the acquisition of different segments in the k-space corresponding to each cardiac phase. To deal with respiratory motion, cardiac imaging is performed with a breath-holding procedure or using navigator-gated, or self-gated acquisitions [94–97]. However, a considerable number of patients suffer from multiple breath-holding difficulties, diaphragmatic drifts, or irreproducible breath-holding.

Advances in reconstruction techniques allow the acquisition of the whole cine imaging in a single breath-hold without compromising its spatial or temporal resolutions [41, 42, 63, 64, 98, 99]. In addition, free-breathing real-time cardiac cine imaging is employed to overcome breathing and gating problems. However, the existing real-time sequences have limited spatial and temporal resolution of the images with a lower signal-to-noise ratio (SNR). There is an unmet need for advanced techniques to address these limitations.

2.4.2. LATE GADOLINIUM ENHANCEMENT IMAGING

LGE is a valuable tool for the assessment of cardiac tissue viability. LGE has become the standard non-invasive imaging technique for determining ischemic and non-ischemic focal fibrosis of the myocardium [100]. LGE was shown to be very accurate in the detection of acute myocardial infarction and can provide valuable prognostic information regarding the LV remodeling improvement in this cohort [101]. In addition, the presence and extent of LGE is a strong indicator of improvement in contractility in chronic ischemic heart disease [100]. While LGE was originally developed for scar detection, it has also demonstrated an important diagnostic role in non-ischemic cardiac diseases, where different cardiomyopathies exhibit different LGE patterns [102].

The LGE concept is based on the delayed washing of gadolinium-based contrast in and out of the myocardium with an increased proportion of extracellular space. The increased volume distribution of gadolinium in scar regions than normal tissue is demonstrated as brighter regions in T_1 -weighted imaging within 10-30 minutes after contrast administration 2.15. LGE is commonly acquired in multi-slice 2D imaging with slice-thickness of 8-10 mm [103]. However, certain applications of LGE require further improvement in spatial resolution, such as the assessment of fibrosis in the right ventricle and left atrium of the heart [104]. As an alternative, 3D LGE was developed to offer a higher isotropic resolution. However, the 3D LGE is challenged by its long scan time which imposes acquisition difficulties due to temporal changes in contrast agent concentration, as well as patient discomfort. Several parallel imaging and compressed sensing reconstruction techniques were developed to address its long acquisition time [105].

2.4.3. MYOCARDIAL T_1 MAPPING

Myocardial T_1 mapping is an emerging imaging technique for spatially-resolved quantitation of the myocardial tissue composition and assessment of myocardial diffuse fibrosis [2]. The T_1 mapping technique aims to estimate the time required by the protons to re-calibrate their spins along with the longitudinal magnetization after being excited by a radiofrequency pulse [106]. The T_1 times vary at different locations of the myocardium reflecting the underlying tissue composition and content of diffuse fibrosis. There is increasing evidence that the deviation of myocardial T_1 values from the normal range is a potential indicator for a variety of non-ischemic cardiomyopathies [107].

Typically, T_1 maps are being reconstructed by voxel-wise curve fitting of a number of T_1 -weighted images acquired at different inversion times 2.16. Several techniques have been developed over the last decade for accurate and reproducible measurement of the myocardial T_1 mapping. The modified look-locker inversion recovery (MOLLI) sequence and its different variants are being frequently used in clinical protocols for native

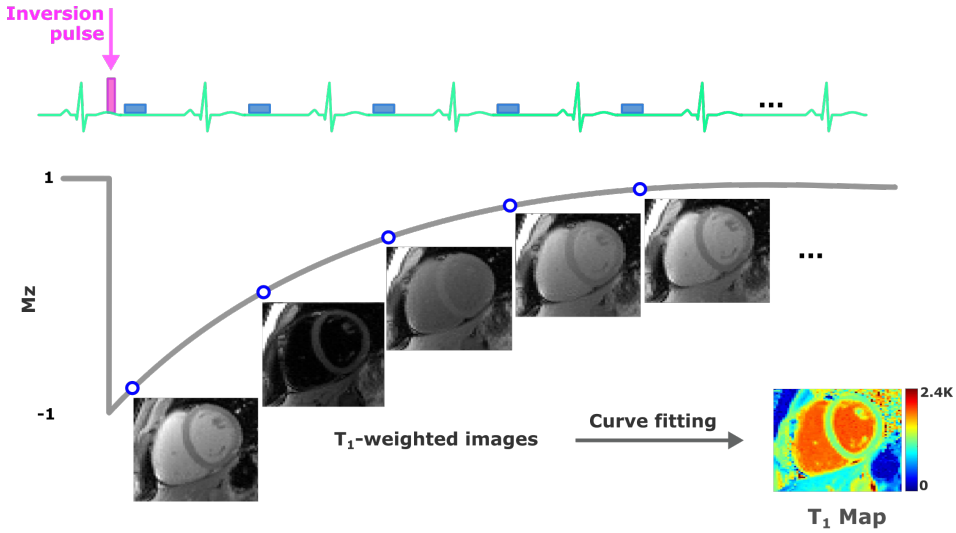


Figure 2.16: Myocardial T₁ Mapping.

myocardial T₁ mapping or post-contrast administration [108]. T₁ mapping techniques are challenged by the length of the breath-holding period required during acquisition and its dependency on heart rate variations and magnetization transfer. New T₁ mapping techniques are being proposed to address these challenges, such as the shortened MOLLI (ShMOLLI) technique [109] that improves the scan duration and heart rate dependency, the saturation recovery single-shot acquisition sequence (SASHA) that utilize saturation pulses to reduce the sensitivity of T₁ measurements to heart rate and T₂ effects [110], and more recently the slice-interleaved T₁ (STONE) sequence which enables free-breathing acquisition and more volumetric coverage of the myocardium with improved accuracy and precision of the T₁ measurements [111].

The reconstruction of an accurate T₁ map for the myocardium is also challenged by the motion artifacts induced in different T₁-weighted images due to failure of breath-holding or diaphragmatic drifts [112, 113]. Most of the previous T₁ mapping techniques require some form of motion correction such that myocardial voxels across all acquired T₁-weighted images are co-aligned. The T₁ maps are typically analyzed by a manual or automatic delineation of the myocardium and calculate the global T₁ values over the whole heart or at each segment of the AHA 16-segment model of the heart.

3

DEEP COMPLEX CONVOLUTIONAL NETWORK FOR FAST RECONSTRUCTION OF 3D LATE GADOLINIUM ENHANCEMENT CARDIAC MRI

Hossam El-Rewaidy, Ulf Neisius, Jennifer Mancio, Selcuk Kucukseymen , Jennifer Rodriguez, Amanda Paskavitz, Bjoern Menze, Reza Nezafat, "Deep complex convolutional network for fast reconstruction of 3D late gadolinium enhancement cardiac MRI," NMR in biomedicine, 2020, 33(7), e4312. [114]

ABSTRACT

Several deep-learning models have been proposed to shorten MRI scan time. Prior deep-learning models that utilize real-valued kernels have limited capability to learn rich representations of complex MRI data. In this chapter, we utilize a complex-valued convolutional network (CNet) for fast reconstruction of highly under-sampled MRI data and evaluate its ability to rapidly reconstruct 3D late gadolinium enhancement (LGE) data.

CNet preserves the complex nature and optimal combination of real and imaginary components of MRI data throughout the reconstruction process by utilizing complex-valued convolution, novel radial batch normalization, and complex activation function layers in a U-Net architecture. CNet enables fast reconstruction of highly accelerated 3D MRI with superior performance to real-valued networks, and achieve faster reconstruction than compressed-sensing.

3

AUTHOR CONTRIBUTIONS

The conception of the initial idea supporting this publication, data curation and management, development and design of methodology, design and implementation of the proposed models in all experiments, statistical analysis and data interpretation, and writing and revising the manuscript.



RESEARCH ARTICLE

Deep complex convolutional network for fast reconstruction of 3D late gadolinium enhancement cardiac MRI

Hossam El-Rewaify^{1,2} | Ulf Neisius¹ | Jennifer Mancio¹ |
Selcuk Kucukseymen¹ | Jennifer Rodriguez¹ | Amanda Paskavitz¹ |
Bjoern Menze² | Reza Nezafat¹

¹Department of Medicine (Cardiovascular Division), Beth Israel Deaconess Medical Center and Harvard Medical School, Boston, Massachusetts

²Department of Computer Science, Technical University of Munich, Munich, Germany

Correspondence

Reza Nezafat, PhD, Beth Israel Deaconess Medical Center, 330 Brookline Ave, Boston, MA 02215, USA.

Email: rnezafat@bidmc.harvard.edu

Funding information

American Heart Association, Grant/Award Number: 15EIA22710040; National Institutes of Health, Grant/Award Number: 5R01HL129185

Several deep-learning models have been proposed to shorten MRI scan time. Prior deep-learning models that utilize real-valued kernels have limited capability to learn rich representations of complex MRI data. In this work, we utilize a *complex-valued* convolutional network (CNet) for fast reconstruction of highly under-sampled MRI data and evaluate its ability to rapidly reconstruct 3D late gadolinium enhancement (LGE) data. CNet preserves the complex nature and optimal combination of real and imaginary components of MRI data throughout the reconstruction process by utilizing complex-valued convolution, novel radial batch normalization, and complex activation function layers in a U-Net architecture. A *prospectively* under-sampled 3D LGE cardiac MRI dataset of 219 patients (17 003 images) at acceleration rates $R = 3$ through $R = 5$ was used to evaluate CNet. The dataset was further retrospectively under-sampled to a maximum of $R = 8$ to simulate higher acceleration rates. We created three reconstructions of the 3D LGE dataset using (1) CNet, (2) a compressed-sensing-based low-dimensional-structure self-learning and thresholding algorithm (LOST), and (3) a real-valued U-Net (realNet) with the same number of parameters as CNet. LOST-reconstructed data were considered the reference for training and evaluation of all models. The reconstructed images were quantitatively evaluated using mean-squared error (MSE) and the structural similarity index measure (SSIM), and subjectively evaluated by three independent readers. Quantitatively, CNet-reconstructed images had significantly improved MSE and SSIM values compared with realNet (MSE, 0.077 versus 0.091; SSIM, 0.876 versus 0.733, respectively; $p < 0.01$). Subjective quality assessment showed that CNet-reconstructed image quality was similar to that of compressed sensing and significantly better than that of realNet. CNet reconstruction was also more than 300 times faster than compressed sensing. Retrospective under-sampled images demonstrate the potential of CNet at higher acceleration rates. CNet enables fast reconstruction of highly accelerated 3D MRI with superior performance to real-valued networks, and achieves faster reconstruction than compressed sensing.

Abbreviations: BN, batch normalization; CReLU, complex rectified linear unit; LGE, late gadolinium enhancement; LOST, low-dimensional-structure self-learning and thresholding algorithm; MSE, mean-squared error; realNet, real-valued network; SSIM, structural similarity index measure.

KEYWORDS

complex convolutional network, deep learning, image reconstruction, late gadolinium enhancement, MRI

1 | INTRODUCTION

Long MRI scan time remains a challenge, impacting patient throughput and limiting spatial and temporal resolution. Over the past two decades, numerous acceleration techniques such as parallel imaging,^{1–4} constrained reconstruction,^{5–7} dictionary-based reconstruction,^{8–10} compressed sensing,^{7,11} and magnetic resonance fingerprinting^{12–14} have been developed to reduce scan time. Data-driven techniques such as deep learning are being explored to accelerate image acquisition without explicit assumptions on data.^{15–24} Recent deep learning reconstruction techniques are based on multiple convolution operations using pre-trained kernels with additional non-linearity in the form of activation functions. Different convolutional neural network schemes are utilized to reconstruct MR images from under-sampled acquisitions. The iterative optimization process of compressed sensing formulated as a variational model was recently unfolded in the form of a variational network,²² in which each layer acts as one gradient descent iteration. Similarly, the iterative reconstruction scheme was represented as deep-cascaded convolutional networks with interleaved data consistency layers that maintain acquired data fidelity after each convolutional network.¹⁸ Instead of cascading networks, Qin et al. developed a convolutional recurrent neural network that shares reconstruction information across different network iterations to simulate the iterative optimization process.¹⁹ Deep generative networks have also been utilized to remove aliasing artifacts from magnitude MR images where the generator is trained to produce artifact-free images.^{16,21}

Both magnitude and complex imaging data are used in deep learning-based MR image reconstruction.^{17–22} Readily available magnitude images are appealing for developing and testing new deep-learning-based techniques. However, the phase also carries important information in MR reconstruction that cannot be ignored. While several recent studies have used complex image/ k -space information as network input,^{17,18,22,25} these approaches process real and imaginary components of data separately, concatenated to each other, or fed into a deep convolutional network as different input channels, analogous to RGB information of a color image. However, these approaches only use a kernel in which components of the kernel are real values, which have limited capability to learn naturally acquired complex MRI data representations. Thus, there is an unmet need for deep-learning reconstruction models that process MRI data in the complex domain to enable learning richer representations of the complex data.

A convolutional network framework that utilizes complex-valued convolutional kernels to learn complex representations from data was recently proposed.²⁶ These kernels have complex weights of real and imaginary components that are adjusted with a convolutional operation incorporating both real and imaginary components of the input data and output feature maps. This family of neural networks exhibits specific characteristics in its learning, self-organization, and processing dynamics.^{27–29} The complex manifolds learned by complex networks are easier to optimize and faster to learn,³⁰ have longer noise-immunity memory, and exhibit better generalization characteristics.^{27–29} Considering the complex nature of MRI signals and the necessity for an optimal combination of real and imaginary parts of the k -space data, a complex neural network may be beneficial in MRI reconstruction. Complex neural networks were previously utilized to estimate tissue parametric maps in MRI fingerprinting³¹ and MR image reconstruction.^{32,33}

In this work, we utilize and evaluate a complex convolutional neural network (CNet) for fast reconstruction of highly under-sampled 3D late gadolinium enhancement (LGE) MRI data. Novel batch normalization (BN) is proposed to normalize complex-valued feature maps and MR data without magnitude or phase distortions. CNet performance is qualitatively and quantitatively evaluated using a prospectively under-sampled cardiac MRI dataset of 3D LGE images. In this study, we used a compressed-sensing based low-dimensional-structure self-learning and thresholding algorithm (LOST) as a reference for training and evaluating our model.

2 | METHODS

We consider a 3D complex-valued zero-filled MR image, $\mathbf{Y} \in \mathbb{C}^N$, such that

$$\mathbf{Y} = \mathbf{S}\mathbf{F}^{-1}\mathbf{\Gamma}\mathbf{X} + \mathbf{\epsilon}, \quad (1)$$

where $\mathbf{X} \in \mathbb{C}^{NN_c}$ represents fully sampled k -space data from N_c coils, $N = N_x N_y N_z$, where $N_x, N_y,$ and N_z are the numbers of acquired k -space samples in the $x, y,$ and z directions, respectively; \mathbf{F}^{-1} is the inverse Fourier coefficient matrix (defined as the Kronecker product between an $N \times N$ DFT matrix and an $N_c \times N_c$ identity matrix), $\mathbf{\epsilon}$ is modeled as an additive white Gaussian noise, $\mathbf{\Gamma}$ is an under-sampling mask that controls the acceleration rate during MR acquisition, and \mathbf{S} is a matrix contains the complex conjugate of coil sensitivity maps from N_c coils of size $N \times NN_c$. In the case

of accelerated acquisition (ie beyond the Nyquist criterion), Equation 1 results in aliased image data Y , where the characteristics of artifacts in Y are largely dependent on the acceleration rate and the under-sampling pattern.

A priori knowledge of image and artifact characteristics can be employed to regularize an optimization function to produce an acceptable solution for the reconstruction problem. In deep learning, image and artifact characteristics can be exploited as trainable parameters from the same domain as the under-sampled images. Training these parameters can be achieved by solving the following optimization problem:

$$\min_{\Theta} \left\| \hat{X} - \Psi(Y|\Theta) \right\|_2^2, \quad (2)$$

where \hat{X} represents the single-channel LOST-reconstructed data in the image domain, and Ψ is a domain transform that maps the corrupted under-sampled image manifold to an artifact-free image manifold using learnable parameters Θ . Each of the trained parameters Θ acts as an operator in a nonlinear system that can be generalized to reconstruct new artifact-free images from under-sampled MR acquisitions.

In this work, we aim to exploit both image and artifact characteristics in their original complex form by learning the complex domain transform, Ψ , and parameters, Θ . Each step of the proposed reconstruction algorithm is described below.

3 | NETWORK ARCHITECTURE

○Net is a fully convolutional network with a U-net architecture (Figure 1) that propagates complex image data in contractive and expansive paths for multi-scale artifact removal and multi-resolution de-noising.^{17,20,24,34} In the contractive path, complex image input data are fed into two complex convolutional layers each with 64 kernels to extract basic features and noise patterns. The resulting feature maps are down-sampled using a complex convolution layer of 64 kernels and a stride of 2. This process is repeated through three down-sampling stages; at each stage, higher-scale features are extracted using complex convolutional layers with twice the previous number of kernels (ie 64, 128, and 256 over the three down-sampling stages). The resulting feature maps pass through two convolution layers of 512 and 256 complex kernels. The expansive path then maps the feature maps at each down-sampling stage onto an analogous stage of similar map size and kernel number (Figure 1B). The up-sampling layers are utilized to increase the size of feature maps by a factor of 2 at each up-sampling stage to provide a clean version of the artifact-contaminated images at different resolution levels. Corresponding feature maps in the up-sampling and down-sampling stages are concatenated. At all previous steps, each convolutional layer is followed by radial BN and complex activation layers, where all kernels are 2D complex valued consisting of real and imaginary components of size 3×3 (ie, the equivalent tensor size is $3 \times 3 \times 2$). The last feature maps are combined using a complex convolutional layer with kernel size 1×1 to reconstruct the final output image. The following sections describe various components of the proposed network.

For a 2D complex image, the corresponding ○Net data point is represented by a real-valued tensor of size $(N_x, N_y, 2)$ that includes both real and imaginary components of the complex image. This tensor flows through multiple complex operational points in the network as follows.

3.1 | Complex convolutional layer

In the proposed network, the complex input image, $I = x+iy$, is convolved with a complex filter, $k = a+ib$,²⁶ such that

$$I \circledast k = (a \circledast x - b \circledast y) + i(b \circledast x + a \circledast y) \quad (3)$$

where \circledast represents a convolution operation. This operation can be accomplished in the real-valued arithmetic by convolving the same kernels, a (or b), with each of the real and imaginary parts of the image, x and y , separately (Figure 2). The gradients of a (or b) should be calculated in the backwards direction considering both operations on x and y .

3.2 | Radial BN layer

BN is important for accelerating and stabilizing the convergence of neural networks.³⁵ Although the original BN was proposed for real-valued networks, a generalization to the complex data was proposed by Trabelsi et al.²⁶ In their complex version, the distribution of both real and imaginary components was independently shifted to have zero mean, then scaled by the covariance matrix of the real and imaginary components to ensure equal variance for the two components. However, separately shifting the distribution of each component towards zero mean induces distortion in the phase and magnitude (Figure 3).

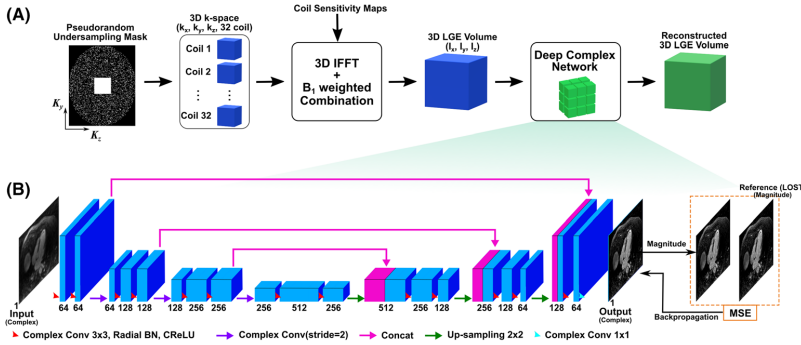
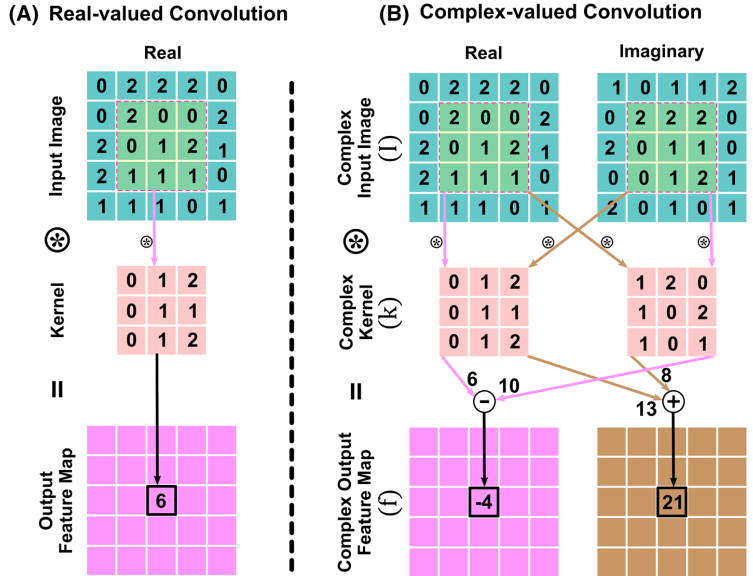


FIGURE 1 CNet pipeline. A, 3D MR data from 32 coils acquired in the k -space, $\mathbf{K}(k_x, k_y, k_z, 32)$, with a pseudorandom under-sampling pattern. Multi-coil data is transformed to the image domain by 3D inverse fast Fourier transform (IFFT), then combined using B_1 -weighted reconstruction and coil sensitivity information to produce a single 3D complex data volume in the image domain, $\mathbf{I}(i_x, i_y, i_z)$. B, Each slice is fed into cascaded complex convolutional layers with kernel size 3×3 with contractive and expansive paths. The contractive path includes convolutional layers with different sizes of kernel (ie 64, 128, and 256) interleaved with three under-sampling stages using complex convolutional layers with a stride of 2 to extract high-level features at multi-resolution levels. The feature maps pass through a bottleneck convolutional layer of 512. The expansive path gradually restores the original resolution of the data through three up-sampling stages; in each, the analogous feature maps from the two paths (ie contractive and expansive) at each level are concatenated. A complex convolutional layer with a similar number of kernels to the contractive path was applied at each level. This network results in a complex-valued 2D image at the last layer. The magnitude of the complex-valued output is compared with the LOST-reconstructed reference magnitude image to calculate the MSE loss. All convolutional layers are followed by radial BN and complex ReLU, with the exception of the last convolutional layer

To address this challenge, we propose radial BN in which phase information is maintained and magnitude is scaled such that relative differences are preserved between complex quantities. In radial BN, the input complex data are transformed to polar coordinates, $Z = R e^{j\theta}$. Standard BN is applied to the magnitude data, R , to have a mean of τ and standard deviation of 1; thus, the normalized magnitude can be calculated as

$$R_{bn} = \left(\frac{R - \mu_R}{\sqrt{\sigma_R^2 + \epsilon}} \right) \gamma + \beta + \tau, \quad (4)$$

FIGURE 2 Numerical examples of real-valued (A) and complex-valued (B) convolution operations. The complex-valued convolution operation is calculated using four real-valued convolution operations. In complex convolution, the input image (I), kernel (k), and output feature maps (f) are complex values with real and imaginary components. The real component of the output maps is described as $R(f) = R(k) \odot R(I) - I(k) \odot I(I)$ and the imaginary component as $I(f) = R(k) \odot I(I) + I(k) \odot R(I)$, where \odot represents the convolution operation



where μ_R and σ_R^2 are the respective mean and variance of R , ϵ is a constant added to the variance for numerical stability, and β and γ are trainable parameters for shifting and scaling data distribution.³⁵ We introduce a new constant, τ , to ensure a positive value for the normalized R ($\tau = 1$ was empirically used in our experiments). The normalized complex data are transformed back to Cartesian coordinates using the normalized magnitude and the same phase, $Z = R_{bn} e^{i\theta}$.

3.3 | Down-sampling and up-sampling layers

To collect artifact patterns on multiple scales and allow multi-resolution artifact removal, complex feature maps generated by the convolutional layers were down-sampled in some parts of the network then up-sampled again to retain the original resolution of the output images. To down-sample the feature maps, a complex convolutional layer with stride greater than 1 was utilized. The up-sampling layer generates complex feature maps with a larger size than the input feature maps by bilinear interpolation of the real and imaginary components.

3.4 | Complex activation function

Real-valued activation functions can be extended in the complex domain to separately activate real and imaginary parts,³⁶ eg a complex rectified linear unit (CReLU):

$$\text{CReLU} = \text{ReLU}(\Re(Z)) + i \text{ReLU}(\Im(Z)), \quad (5)$$

where $\Re(Z)$ and $\Im(Z)$ are the real and imaginary components of the complex-valued image Z . CReLU is holomorphic (ie complex differentiable in neighborhood points) when both real and imaginary components are strictly positive or negative.²⁶

4 | IMAGE ACQUISITION AND PRE-PROCESSING

To assess the performance of the proposed reconstruction techniques, we utilized a dataset of 219 patients (145 males, mean 55 years) referred for a clinical cardiac MRI examination for viability assessment. These patients were recruited prospectively as part of our previous study.³⁷

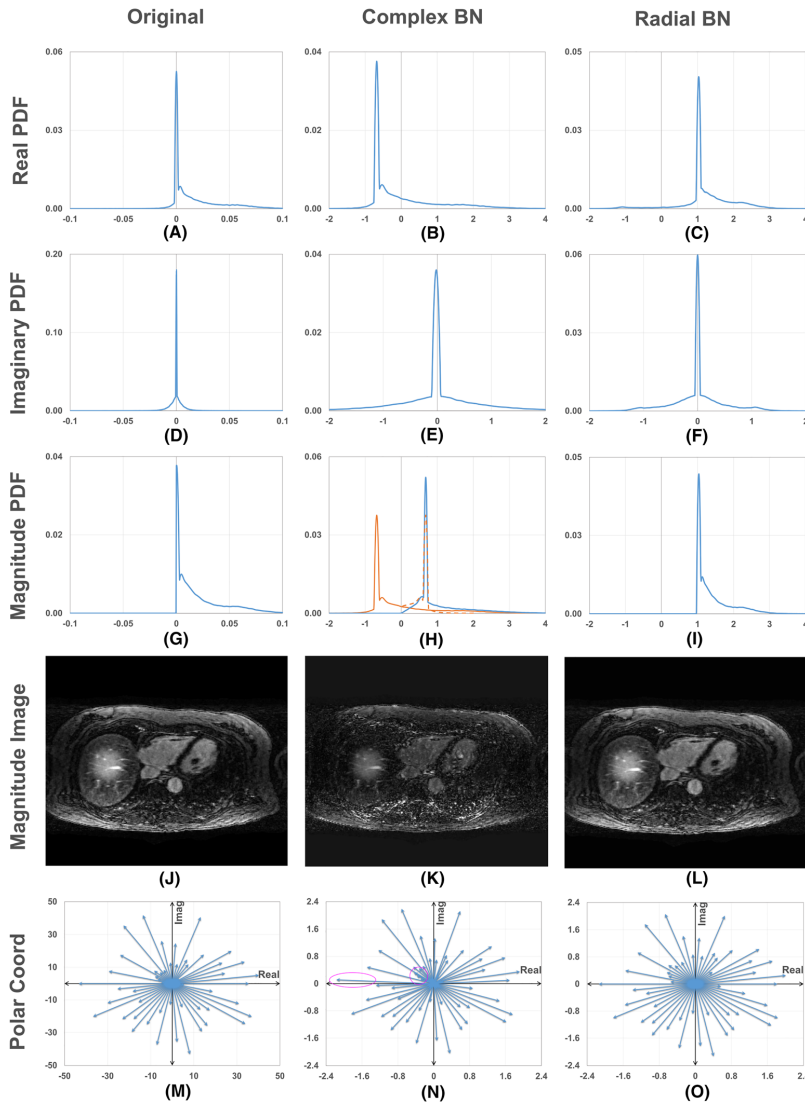


FIGURE 3 A-I, Effect of complex and radial data/BN methods on complex data samples. Probability distribution function (PDF) of the real and imaginary parts and magnitude of the original complex image (A, D, and G, respectively), the result of complex BN on the original data sample (B, E, and H, respectively), and the result of the proposed radial BN on the original data sample (C, F, and I, respectively). The magnitude PDF resulting from complex BN has substantially altered shape from that of the original data or radial BN result PDFs (third row), due to shifting the real and imaginary distributions of the data separately to have zero mean, where pixels with small values change its polarity (orange curve in H). J-L, The corresponding 2D magnitude images of another original data sample and its corresponding complex and radial BNed data (J, K, and L, respectively). M, Random complex data sample points represented by magnitude and phase in the polar coordinates. N, Performing the complex BN on this data sample resulted in distorted phase information (magenta ellipses) due to shifting the real and imaginary distributions independently to zero mean. O, Radial BN maintained the phase information and the relative differences in magnitude between the data points similar to those of the original data

Informed consent was obtained from each subject and the imaging protocol was approved by the institutional review board and institutional human subjects committee. 3D LGE images were acquired using a 1.5 T Philips Achieva system (Philips Healthcare, Best, The Netherlands) with a 32-channel cardiac coil. Images were acquired in the axial direction to cover the whole heart using a gradient echo imaging sequence with the following parameters: repetition time/echo time = 5.2/2.6 ms, field of view = $320 \times 320 \times 100\text{--}120$ mm³, flip angle = 25°, and spatial resolution = 1.0-1.5 mm³. A free-breathing ECG-triggered navigator-gated with inversion-recovery gradient echo imaging sequence was used. The 3D k -space was prospectively under-sampled in all patients using a pseudorandom mask, where the k -space was fully sampled within 15-20% in the k_y direction and 25% in the k_z direction around the center of k -space, and randomly sampled elsewhere^{37,38} (Figure 1). The acceleration rate was randomly prospectively chosen by the operator between $R = 3$ and $R = 5$ (130 patients at $R_p = 3$, 25 patients at $R_p = 4$, and 64 patients at $R_p = 5$). k -space data from all 32 coil channels were exported and used for evaluation. All images were previously reconstructed using the LOST algorithm³⁹ for training and evaluation.

5 | NETWORK TRAINING

The 3D k -space data from 32 coils were zero-filled and transformed into the complex image domain by 3D inverse Fourier transformation. Coil sensitivity information was then utilized to combine data from different coils into single complex-valued 3D volume data per patient in the image domain using B_1 -weighted reconstruction.³⁹ The corresponding LOST-reconstructed image data were used as a reference for loss calculations during network training and evaluation of results during testing. All images were normalized using the same radial BN process.

We divided the data into training (153 patients; 11 726 slices) and testing datasets (66 patients; 5277 slices). The network was trained until convergence with a fixed number of epochs (ie 50) via an Adam optimizer with a learning rate function, $0.1^{[\text{epoch}/20]+1}$, where the learning rate exponentially decreased with the number of epochs. The batch number was 100 complex images of size 256×256 . The mean-squared error (MSE) loss (ℓ) function was applied to minimize the error between LOST and network prediction images, such that $\ell = \|x_{\text{LOST}} - |x_{\text{URUS}}|\|_2^2$, where x_{LOST} represents LOST-reconstructed magnitude images and $|x_{\text{URUS}}|$ is the magnitude of CNet complex predictions.

This model was implemented using the open-source Python-based PyTorch library Version 0.41 (code available at <https://github.com/hossam-elrewaidy/urus-mri-recon>).⁴⁰ The B_1 -weighted reconstruction was performed on MATLAB (MathWorks, Natick, Massachusetts). All models in this work were trained and tested on an NVIDIA DGX-1 system equipped with eight Tesla V100 GPUs (each of 32 GB memory and 5120 cores), and a CPU of 88 cores: Intel Xeon 2.20 GHz each, and 504 GB RAM memory. CNet takes an average of 4 h to train on this machine. CPU-based LOST reconstruction was performed on a computing cluster of 20 cores and 100 GB of RAM.

6 | EXPERIMENTAL EVALUATION

CNet was evaluated by two means: initially, the prospectively under-sampled data ($R_p = 3$ -5) were reconstructed, then we retrospectively under-sampled the original data to simulate higher accelerations beyond the prospective under-sampling rates in separate experiments. Three new datasets (D_1 , D_2 , and D_3) were generated from the originally acquired dataset (D_0) by increasing the acceleration rate by 1 in each new dataset. Since D_0 includes patient data acquired at different acceleration rates, $R_p = \{3, 4, \text{ and } 5\}$, D_1 includes retrospective acceleration rates, $R_r = \{4, 5, \text{ and } 6\}$, D_2 includes rates $R_r = \{5, 6, \text{ and } 7\}$, and D_3 includes rates $R_r = \{6, 7, \text{ and } 8\}$. A pseudorandom mask was used to retrospectively under-sample the acquired k -space, where 16-21% of the k -space lines at the center were fully sampled and the rest randomly under-sampled.³⁷

For comparison, a real-valued network (realNet) of the same U-net architecture was built using the standard real-valued ReLU, BN, and convolutional layers. RealNet has the same number of convolutional layers as CNet but has an increased number of kernels at each layer as illustrated in Figure S1. The total number of trainable parameters in realNet is 12 475 073, versus 12 472 578 in CNet . RealNet has two input channels containing real and imaginary components of zero-filled complex images and an output of a magnitude reconstructed image. The optimal hyperparameters were experimentally determined for both CNet and realNet.

Deep residual networks (ResNet) were also investigated in this work. Complex ResNet was built with five standard residual blocks of 64, 128, 256, 128, and $64 \times 3 \times 3$ complex kernels, respectively (Figure S2). Two convolutional layers were added at the network input and output with 64 and one 7×7 complex kernels, respectively. The total number of trainable parameters in this network was $13\,089 \times 10^3$. Similar to CNet , ResNet has complex-valued 2D images at the input and output layers.

7 | DATA ANALYSIS

For quantitative assessment of CNet reconstruction performance, the MSE and structural similarity index measure (SSIM)⁴¹ of the magnitude of CNet -reconstructed and LOST-reconstructed images were calculated. While MSE calculates the unobserved mean intensity difference between the predicted and reference images, SSIM quantifies human visual perception qualities by combining luminance, contrast, and structural differences between predicted and reference images. Per-slice and per-patient LGE scar percentages were calculated using a conventional semi-automatic thresholding-based scar quantification method with three standard deviations of signal from the remote normal myocardium.⁴² For this purpose, the left ventricular myocardium was manually segmented from the entire heart in all patients with a scar in the testing dataset.

For qualitative assessment, three independent readers (with 10, 6, and 6 years of experience in cardiac MRI, respectively) graded the reconstructed images using LOST, CNet , and realNet on a five-point score to evaluate overall quality per patient (1—poor quality with large artifacts, 2—fair quality with moderate artifacts, 3—good quality with small artifacts, 4—excellent quality with no artifacts, and 5—spectacular quality as fully sampled images). Readers were blinded to the method of reconstruction. In addition, each reader identified patients with a left ventricular scar. Finally, all three reconstructed images from each patient were shown to the readers simultaneously, and each reader selected the best imaging dataset for best overall image quality.

A two-tailed Student *t*-test was performed for comparison of continuous variables between reconstruction methods. To compare categorical data, the Chi-squared test was used. Significance was declared at two-sided *p*-values less than 0.05. For pairwise comparisons following a three-group inferential test that was significant, a Bonferroni correction was used.

8 | RESULTS

Sample LGE images reconstructed using realNet, \mathbb{C} Net, and LOST from different patients acquired at prospective acceleration rates $R_p = 3$ and 5 are shown in Figure 4. \mathbb{C} Net-reconstructed images maintain scar-blood contrast and are visually comparable to those of LOST. Figure 5 shows two different patient LGE images with scar reconstructed by LOST, \mathbb{C} Net, and realNet. In both images, \mathbb{C} Net preserves better fine details of the scar than realNet with respect to the reference images, as indicated by the error maps.

Figure 6 shows \mathbb{C} Net-reconstructed images scanned at prospective acceleration rate $R_p = 3$ and corresponding retrospectively under-sampled versions at $R_r = 4, 5,$ and 6 from $D_1, D_2,$ and D_3 datasets, respectively, compared with realNet images. Noisy, blurry zero-padded images were restored by \mathbb{C} Net reconstruction at all acceleration rates. In addition, \mathbb{C} Net reconstruction recovered scar-blood contrast and scar shape compared with zero-padded images with respect to reference images at different acceleration rates. \mathbb{C} Net was also able to perform at higher acceleration rates (up to $R_r = 8$) and maintain image details (Figure 7).

The performance of \mathbb{C} Net was compared with realNet and zero-filled images (Table 1). \mathbb{C} Net images showed significantly higher SSIM than zero-filled images and significantly lower MSE for all datasets (ie $D_0, D_1, D_2,$ and D_3) ($p < 0.01$ for all). The visual perceptual-based SSIM values of \mathbb{C} Net images were significantly higher than those of realNet for all datasets ($p < 0.01$). However, \mathbb{C} Net-based MSE values were significantly lower than those of realNet in D_0 and D_1 only ($p < 0.01$).

\mathbb{C} Net showed faster convergence during training and more stable testing results at different training epochs when radial BN layers were included (Figure S3). \mathbb{C} Net reported an MSE of 0.083 and SSIM of 0.862 without radial BN, compared with 0.077 and 0.876 when radial BN was utilized. The U-net-based \mathbb{C} Net showed slightly better performance compared with the complex ResNet. The MSE and SSIM of ResNet-reconstructed images were 0.079 and 0.869 when radial BN was utilized, and 0.087 and 0.858 without BN, respectively.

\mathbb{C} Net performance at different epochs throughout network training is shown in Figure 8. SSIM increased and MSE decreased as the number of epochs increased in the prospectively (ie D_0) and retrospectively (ie $D_1, D_2,$ and D_3) under-sampled datasets. The consistent evolution of SSIM

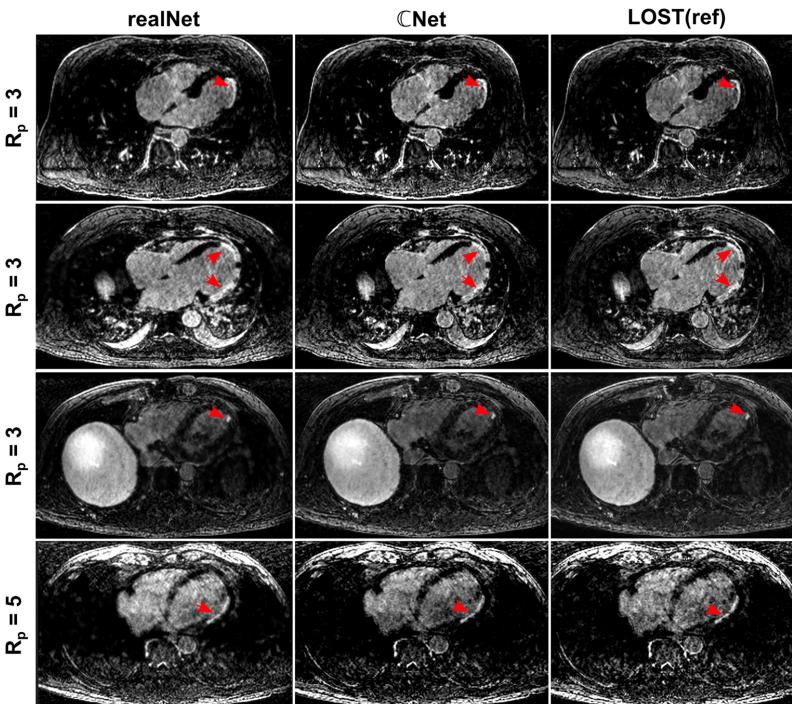
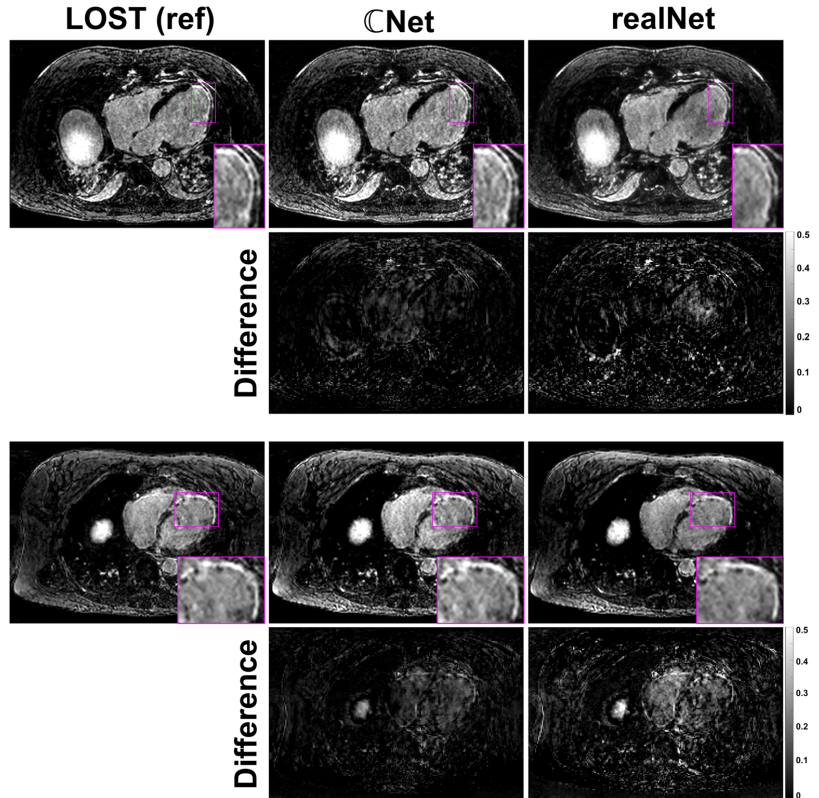


FIGURE 4 Four LGE images from different patients reconstructed using realNet, \mathbb{C} Net and LOST with different acceleration rates, $R_p = 3$ and $R_p = 5$. Arrows indicate areas of scar

FIGURE 5 LOST-, \mathbb{C} Net-, and realNet-reconstructed images of two patients (first and third rows). The corresponding error maps of \mathbb{C} Net- and realNet-reconstructed images w.r.t. the LOST reference are shown (second and fourth rows)



and MSE between training and testing for all datasets indicates minimal overfitting of the model. Sample magnitude and phase parts of feature maps captured after the first complex convolutional layer showed a variety of image-specific features and noise patterns within the layer (Figure S4).

There was no difference between \mathbb{C} Net and LOST (3.54 ± 0.92 and 3.51 ± 1.05 , respectively, $p = 0.54$) in the overall assessment of image quality by three independent readers (Table 2). \mathbb{C} Net-reconstructed images had better image quality than those using realNet (3.54 ± 0.92 versus 3.06 ± 0.99 ; $p < 0.01$) (Table 2). In the testing dataset, readers identified on average 20 patients with a scar in LGE images reconstructed by LOST and \mathbb{C} Net, but only 19 patients with a scar on LGE images reconstructed by realNet. \mathbb{C} Net, LOST, and realNet 3D LGE were ranked as the best method for image quality in 24, 24, and 17 patients, respectively (Table 2).

There was an excellent correlation in scar extent between \mathbb{C} Net and LOST ($R^2 > 0.97$ and $R^2 > 0.99$ for per-slice and per-patient scar percentages, respectively) (Figure 9). A Bland-Altman plot showed a small bias (0.29%) and narrow limits of agreements (6.86%) for per-slice scar percentage error by \mathbb{C} Net with respect to LOST reference images. The per-patient scar percentage error was $0.17 \pm 1.49\%$ by \mathbb{C} Net with respect to LOST and increased consistently with increasing acceleration rates (Figure 9D).

For a typical 3D LGE dataset of size 256 pixels \times 256 pixels, 100 slices, and 32 channel coils, the reconstruction time was about 15 s for \mathbb{C} Net and 89 min for LOST, which constitutes a 310-fold decrease in reconstruction time.

9 | DISCUSSION

In this work, we utilize a deep complex convolutional network to improve MR image reconstruction from under-sampled acquisitions. This network exploits a priori knowledge of MR image and artifact characteristics in the reconstruction process by learning complex image representations in the form of complex-valued kernels. The efficient utilization of phase information via dual complex components (ie real and imaginary) of the MRI data throughout the reconstruction pipeline allows efficient artifact removal. To stabilize the convergence of \mathbb{C} Net, a novel radial BN method that maintains relative differences between data points without magnitude or phase distortions was proposed.

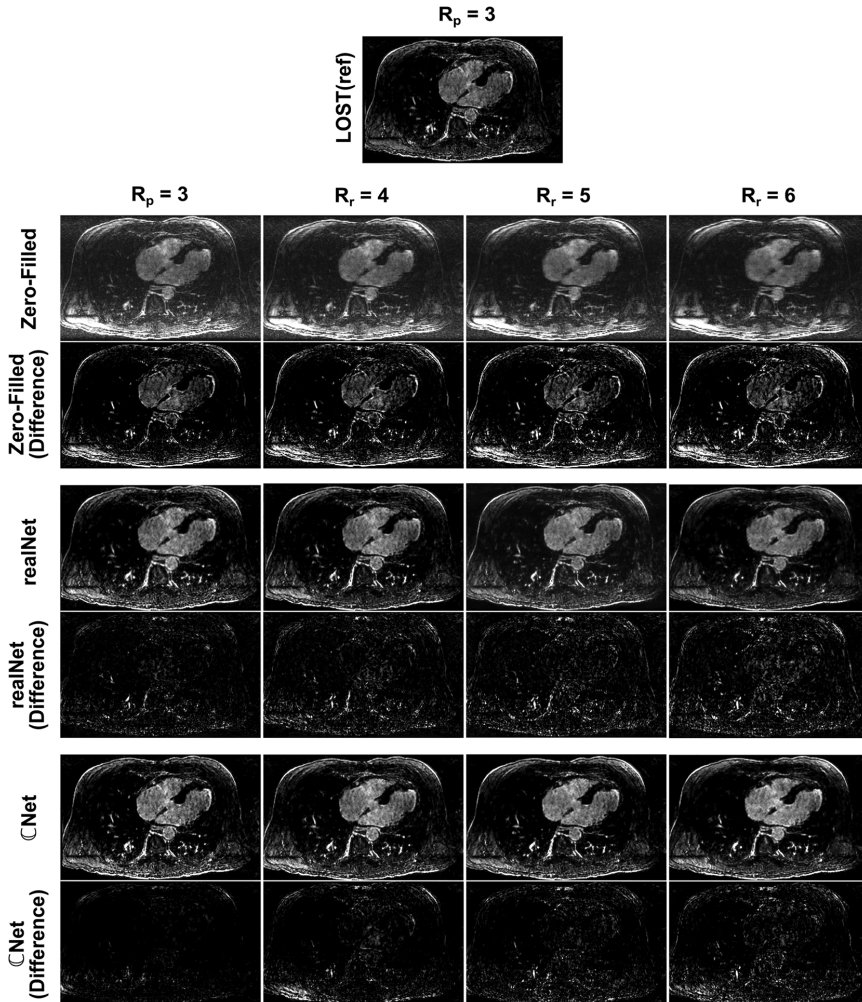


FIGURE 6 Representative LGE images at prospective acceleration rate $R_p = 3$ and retrospective acceleration rates $R_r = 4, 5,$ and 6 reconstructed by CNet compared with LOST reference, realNet, and zero-filled images at each acceleration rate. Image quality is restored with minimal noise and blurring artifacts in CNet -reconstructed images, similar to that of the reference images. Scar-blood contrast is also maintained at higher acceleration rates

The U-net architecture used in our study allows multi-scale artifact removal. The network receptive field increases after each down-sampling layer such that MR images are filtered at different resolution levels and up-sampled to provide clean versions of the artifact-contaminated images at each level. Unlike conventional U-net networks, the down-sampling was performed using complex convolution layers with a stride of 2 instead of the traditional pooling schemes. Although the convolution-based down-sampling adds more trainable parameters to the network, it was utilized in this work because pooling schemes are not well investigated for complex networks. In addition, the bypass connections at each down-sampling stage create shortcuts for the gradient flow in shallow layers and offer better convergence characteristics.^{24,43} Further studies are warranted to investigate the performance of other complex network architectures.

The large prospectively under-sampled dataset considered for the training and evaluation of our models covers the whole heart in the axial direction and provides a wide range of heart structures, slice locations, and scar shapes. This heterogeneous dataset allowed efficient training of our model with minimal overfitting without the need for data augmentation. The large testing dataset also enabled a comprehensive evaluation of our model performance and generalizability in a clinical setting.

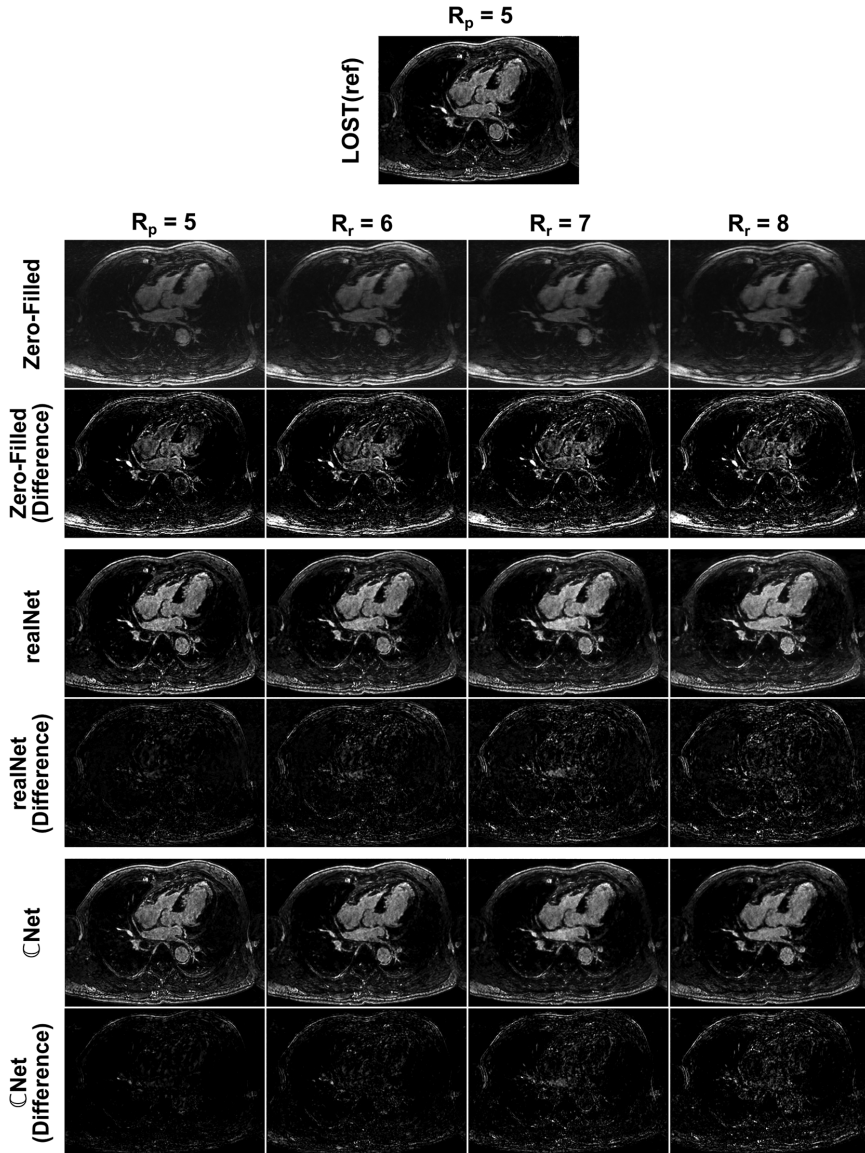


FIGURE 7 Representative LGE image at prospective acceleration rate $R_p = 5$ and retrospective acceleration rates $R_r = 6, 7,$ and 8 reconstructed by \mathbb{C} Net compared with LOST reference, realNet and zero-filled images at each acceleration rate. Image quality is restored with minimal noise and blurring artifacts in \mathbb{C} Net-reconstructed images similar to that of the reference images. Scar-blood contrast is also maintained at higher acceleration rates

We demonstrate the importance of incorporating phase information in the reconstruction process by comparing the complex-valued \mathbb{C} Net with the real-valued realNet. \mathbb{C} Net shows superior image quality compared with realNet in both quantitative and qualitative evaluations, despite their similar architectures and an equal number of trainable parameters. However, \mathbb{C} Net performs twice the number of convolutional operations compared with realNet, since each complex-valued convolution operation was implemented by four real-valued convolution operations. Although our LGE dataset was acquired with relatively short echo time (2.6 ms), which reduces phase errors (mainly caused by field inhomogeneity), the

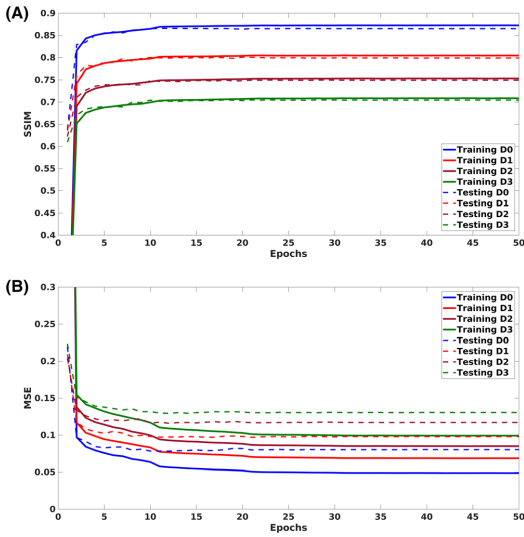


FIGURE 8 Analysis of CNet network performance: SSIM (A) and MSE (B) at all epochs of the training and testing phases in the prospective and retrospective under-sampled datasets

TABLE 1 MSE and SSIM for zero-filled, CNet, and realNet images, in the prospective and retrospective under-sampled datasets

Dataset	MSE			SSIM		
	Input	CNet	realNet	Input	CNet	realNet
D ₀	0.246	0.077	0.089	0.638	0.876	0.750
D ₁	0.263	0.098	0.102	0.595	0.804	0.703
D ₂	0.278	0.117	0.125	0.562	0.753	0.641
D ₃	0.290	0.131	0.138	0.535	0.707	0.612

TABLE 2 Qualitative assessment (per patient) of overall image quality, presence of LGE scars, and the preferred method for diagnosis of LGE images reconstructed using LOST, CNet, and realNet methods from three readers

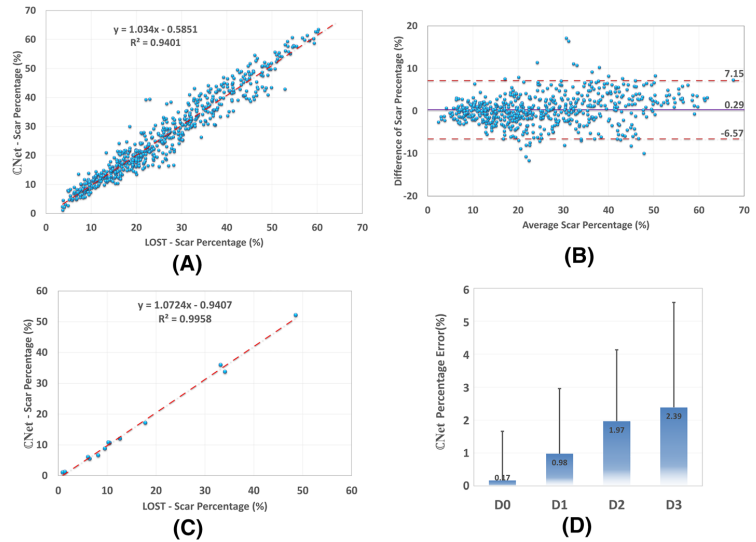
Measure	Overall image quality			Presence of LGE			Method preference		
	LOST	CNet	realNet	LOST	CNet	realNet	LOST	CNet	realNet
Reader 1	3.0 ± 0.9	3.14 ± 0.7	2.89 ± 0.8	17	18	17	29	22	15
Reader 2	3.29 ± 1.0	3.21 ± 0.9	2.5 ± 0.9	20	19	18	20	27	19
Reader 3	4.24 ± 0.84	4.26 ± 0.71	3.77 ± 0.87	23	22	23	24	24	18

phases in our input complex data carry valuable information related to the *k*-space under-sampling pattern (ie pseudorandom trajectory) and hence can help remove under-sampling artifacts.

Image quality using CNet was very similar to that of LOST in both subjective and objective assessments. However, CNet reconstruction time was over 300 times shorter, which is important when considering its adoption in a clinical setting. CNet yielded 3D LGE images without artifact and showed potential for acceleration beyond what compressed sensing can achieve. Additional efforts to increase the acceleration rate in a prospectively under-sampled imaging sequence are needed to evaluate the performance of CNet at high acceleration rates.

In many MRI applications, collecting a fully sampled 3D dataset that can be used as a reference dataset is not possible. A fully sampled high-resolution dataset typically requires a very long scan time, and image quality is impacted by factors such as respiratory or cardiac motion. For post-contrast MRI sequences such as LGE, a change in the underlying signal such as contrast washout adds additional complexity. Therefore, calculating the loss function in such sequences is challenging. In our study, we relied on LOST-reconstructed images for learning and evaluation of CNet. While not ideal, this is the only solution that allowed us to evaluate the potential of CNet in high-resolution 3D LGE imaging.

FIGURE 9 Quantitative analysis of scar percentage: correlation of per-slice scar percentage between \mathbb{C} Net and LOST (A), Bland-Altman plot of differences in per-slice scar percentage between \mathbb{C} Net and LOST w.r.t the average scar percentage of the two methods (B), correlation of the per-patient scar percentage between \mathbb{C} Net and LOST (C), and error of per-patient scar percentage calculated from \mathbb{C} Net-reconstructed images w.r.t. LOST in the prospective and retrospective under-sampled datasets (D)



During \mathbb{C} Net training, the loss function was calculated between the magnitude of \mathbb{C} Net-derived complex images and reference LOST magnitude images. While mapping the complex input image to a magnitude reference forces the network to produce an optimal result for magnitude images without consideration of errors in the phase, complex-to-complex mapping of both input and output images was not investigated in this work due to unavailability of complex-valued reference images, since the complex output of LOST is not normally saved in our clinical workflow.

In this study, we used a complex neural network in a U-net type architecture. The concept of complex neural networks can potentially be adopted in other architectures such as cascaded networks.¹⁸ In LGE imaging, the magnitude of reconstructed images is used to assess the presence of the scar, and phase images are often discarded. However, in several other imaging sequences such as phase-contrast MRI, recovering the phase information is important. Future studies should assess both magnitude and phase recovery to determine if a complex network can provide better image phase reconstruction.

For scar quantification, we used a three-standard-deviation thresholding method that utilizes the distribution of pixel intensities within the myocardium to assess the scar volume. Although the distribution of the myocardial intensities could be altered due to the non-linear processing performed by convolutional networks, an excellent correlation ($R^2 > 0.97$) was reported between the quantified scar volumes from \mathbb{C} Net-reconstructed data and the reference images. An optimal threshold for scar quantification may depend on the reconstruction algorithm and warrants further studies.

Our study has several limitations. We did not have a fully sampled 3D k -space dataset as a reference for comparison, and images were compared with a compressed-sensing reconstruction as the reference standard. While our imaging datasets are relatively large, there was only a small subset of patients with a scar in our training datasets. The performance of the complex convolutional network was assessed only by 3D LGE. In this work, we investigated a complex network solely with 2D convolutional layers. However, 3D convolutional networks have the potential to learn spatial correlations in 3D and further studies are warranted to assess the performance of 3D networks. We compared the performance of \mathbb{C} Net with a real-valued network that takes real and imaginary channels as input and produces single-channel magnitude image as output; however, a better comparison would be with a real-valued network that has real and imaginary channels in both input and output. We tested the performance of a complex convolutional network using the widely used U-net architecture only without intermediate data-consistency steps. Including data-consistency steps that reconstruct coil-combined 3D acquired k -space data in our 2D network was challenging, and future studies are warranted to utilize more advanced models that incorporate data-consistency steps.

10 | CONCLUSION

\mathbb{C} Net enables fast reconstruction of large 3D MRI datasets with superior performance compared with real-valued kernel networks. Our results demonstrate that \mathbb{C} Net can reconstruct 3D LGE images with acceleration rates up to 8 with a more than 300-fold speed-up in reconstruction time compared with compressed sensing.

FUNDING INFORMATION

This study is supported in part by grants from the National Institutes of Health, 5R01HL129185, and the American Heart Association (AHA), 15EIA22710040 (Dallas, TX, USA).

ORCID

Hossam El-Rewaidy  <https://orcid.org/0000-0002-5266-8702>

REFERENCES

- Pruessmann KP, Weiger M, Scheidegger MB, Boesiger P. SENSE: sensitivity encoding for fast MRI. *Magn Reson Med*. 1999;42(5):952-962.
- Griswold MA, Jakob PM, Heidemann RM, et al. Generalized autocalibrating partially parallel acquisitions (GRAPPA). *Magn Reson Med*. 2002;47(6):1202-1210. <https://doi.org/10.1002/mrm.10171>
- McGibney G, Smith MR, Nichols ST, Crawley A. Quantitative evaluation of several partial Fourier reconstruction algorithms used in MRI. *Magn Reson Med*. 1993;30(1):51-59.
- Uecker M, Lai P, Murphy MJ, et al. ESPIRiT—an eigenvalue approach to autocalibrating parallel MRI: where SENSE meets GRAPPA. *Magn Reson Med*. 2014;71(3):990-1001. <https://doi.org/10.1002/mrm.24751>
- Lustig M, Pauly JM. SPIRiT: iterative self-consistent parallel imaging reconstruction from arbitrary k -space. *Magn Reson Med*. 2010;64(2):457-471. <https://doi.org/10.1002/mrm.22428>
- Murphy M, Alley M, Demmel J, Keutzer K, Vasanawala S, Lustig M. Fast ℓ -SPIRiT compressed sensing parallel imaging MRI: scalable parallel implementation and clinically feasible runtime. *IEEE Trans Med Imaging*. 2012;31(6):1250-1262. <https://doi.org/10.1109/TMI.2012.2188039>
- Lustig M, Donoho D, Pauly JM. Sparse MRI: the application of compressed sensing for rapid MR imaging. *Magn Reson Med*. 2007;58(6):1182-1195. <https://doi.org/10.1002/mrm.21391>
- Ravishanker S, Bresler Y. MR image reconstruction from highly undersampled k -space data by dictionary learning. *IEEE Trans Med Imaging*. 2011;30(5):1028-1041. <https://doi.org/10.1109/TMI.2010.2090538>
- Caballero J, Price AN, Rueckert D, Hajnal JV. Dictionary learning and time sparsity for dynamic MR data reconstruction. *IEEE Trans Med Imaging*. 2014;33(4):979-994. <https://doi.org/10.1109/TMI.2014.2301271>
- Song Y, Zhu Z, Lu Y, Liu Q, Zhao J. Reconstruction of magnetic resonance imaging by three-dimensional dual-dictionary learning. *Magn Reson Med*. 2014;71(3):1285-1298. <https://doi.org/10.1002/mrm.24734>
- Block KT, Uecker M, Frahm J. Undersampled radial MRI with multiple coils. Iterative image reconstruction using a total variation constraint. *Magn Reson Med*. 2007;57(6):1086-1098. <https://doi.org/10.1002/mrm.21236>
- Ma D, Gulani V, Seiberlich N, et al. Magnetic resonance fingerprinting. *Nature*. 2013;495(7440):187-192. <https://doi.org/10.1038/nature11971>
- Hamilton JI, Jiang Y, Chen Y, et al. MR fingerprinting for rapid quantification of myocardial T_1 , T_2 , and proton spin density. *Magn Reson Med*. 2017;77(4):1446-1458. <https://doi.org/10.1002/mrm.26216>
- Zhao B, Setsompop K, Adalsteinsson E, et al. Improved magnetic resonance fingerprinting reconstruction with low-rank and subspace modeling. *Magn Reson Med*. 2018;79(2):933-942. <https://doi.org/10.1002/mrm.26701>
- Zhu B, Liu JZ, Cauley SF, Rosen BR, Rosen MS. Image reconstruction by domain-transform manifold learning. *Nature*. 2018;555(7697):487-492. <https://doi.org/10.1038/nature25988>
- Yang G, Yu S, Dong H, et al. DAGAN: deep de-aliasing Generative Adversarial Networks for fast compressed sensing MRI reconstruction. *IEEE Trans Med Imaging*. 2018;37(6):1310-1321. <https://doi.org/10.1109/TMI.2017.2785879>
- Lee D, Yoo J, Tak S, Ye JC. Deep residual learning for accelerated MRI using magnitude and phase networks. *IEEE Trans Biomed Eng*. 2018;65(9):1985-1995. <https://doi.org/10.1109/TBME.2018.2821699>
- Schlemper J, Caballero J, Hajnal JV, Price AN, Rueckert D. A deep cascade of convolutional neural networks for dynamic MR image reconstruction. *IEEE Trans Med Imaging*. 2018;37(2):491-503. <https://doi.org/10.1109/TMI.2017.2760978>
- Qin C, Schlemper J, Caballero J, Price AN, Hajnal JV, Rueckert D. Convolutional recurrent neural networks for dynamic MR image reconstruction. *IEEE Trans Med Imaging*. 2019;38(1):280-290.
- Hauptmann A, Arridge S, Lucka F, Muthurangu V, Steeden JA. Real-time cardiovascular MR with spatio-temporal artifact suppression using deep learning—proof of concept in congenital heart disease. *Magn Reson Med*. 2019;81(2):1143-1156. <https://doi.org/10.1002/mrm.27480>
- Mardani M, Gong E, Cheng JY, et al. Deep generative adversarial neural networks for compressive sensing (GANCS) MRI. *IEEE Trans Med Imaging*. 2018;38(1):167-179. <https://doi.org/10.1109/TMI.2018.2858752>
- Hammernik K, Klatzer T, Kobler E, et al. Learning a variational network for reconstruction of accelerated MRI data. *Magn Reson Med*. 2018;79(6):3055-3071. <https://doi.org/10.1002/mrm.26977>
- Akçakaya M, Moeller S, Weingärtner S, Ugurbil K. Scan-specific robust artificial-neural-networks for k -space interpolation (RAKI) reconstruction: Database-free deep learning for fast imaging. *Magn Reson Med*. 2019;81(1):439-453. <https://doi.org/10.1002/mrm.27420>
- Han Y, Yoo J, Kim HH, Shin HJ, Sung K, Ye JC. Deep learning with domain adaptation for accelerated projection-reconstruction MR. *Magn Reson Med*. 2018;80(3):1189-1205. <https://doi.org/10.1002/mrm.27106>
- Eo T, Jun Y, Kim T, Jang J, Lee H-J, Hwang D. KIKI-net: cross-domain convolutional neural networks for reconstructing undersampled magnetic resonance images. *Magn Reson Med*. 2018;80(5):1-14. <https://doi.org/10.1002/mrm.27201>
- Trabelsi C, Bilaniuk O, Zhang Y, et al. Deep Complex Networks. Paper presented at: International Conference on Learning Representations; 2018; Vancouver.
- Hirose A. *Complex-Valued Neural Networks: Advances and Applications*. Piscataway, NJ: IEEE Press; 2013.
- Arjovsky M, Shah A, Machine YB. Unitary evolution recurrent neural networks. *Proc Machine Learn Res*. 2016;48:1120-1128.
- Wisdom S, Powers T, Hershey J, Le Roux J, Atlas L. Full-capacity unitary recurrent neural networks. In: *Advances in Neural Information Processing Systems*. 30th ed. Barcelona Spain: Curran Associates Town; 2016:4880-4888.
- Nitta T. Orthogonality of decision boundaries in complex-valued neural networks. *Neural Comput*. 2004;16(1):73-97.

31. Virtue P, Yu SX, Lustig M. Better than real: complex-valued neural nets for MRI fingerprinting. In: *2017 International Conference on Image Processing (ICIP)*. 24th ed. Piscataway, NJ: IEEE; 2018:3953-3957. <https://doi.org/10.1109/ICIP.2017.8297024>.
32. Dedmari MA, Conjeti S, Estrada S, Ehses P, Stöcker T, Reuter M. Complex fully convolutional neural networks for MR image reconstruction. In: Knoll F, Maier A, Rueckert D, eds. *Lecture Notes in Computer Science (Including Subseries Lecture Notes in Artificial Intelligence and Lecture Notes in Bioinformatics)*. Vol 11074. Cham, Switzerland: Springer; 2018:30-38. https://doi.org/10.1007/978-3-030-00129-2_4.
33. Wang S, Cheng H, Ying L, et al. DeepcomplexMRI: exploiting deep residual network for fast parallel MR imaging with complex convolution. June 2019. <http://arxiv.org/abs/1906.04359>. Accessed January 2, 2020.
34. Yu S, Dong H, Yang G, et al. Deep de-aliasing for fast compressive sensing MRI. 2017. <http://arxiv.org/abs/1705.07137>. Accessed April 12, 2020.
35. Ioffe S, Szegedy C. Batch normalization: accelerating deep network training by reducing internal covariate shift. *Proc Machine Learn Res*. 2015;37:448-456.
36. Benvenuto N, Piazza F. On the complex backpropagation algorithm. *IEEE Trans Signal Process*. 1992;40(4):967-969. <https://doi.org/10.1109/78.127967>
37. Basha TA, Akçakaya M, Liew C, et al. Clinical performance of high-resolution late gadolinium enhancement imaging with compressed sensing. *J Magn Reson Imaging*. 2017;46(6):1829-1838. <https://doi.org/10.1002/jmri.25695>
38. Akçakaya M, Rayatzadeh H, Basha TA, et al. Accelerated late gadolinium enhancement cardiac MR imaging with isotropic spatial resolution using compressed sensing: initial experience. *Radiology*. 2012;264(3):691-699. <https://doi.org/10.1148/radiol.12112489>
39. Akçakaya M, Basha TA, Goddu B, et al. Low-dimensional-structure self-learning and thresholding: regularization beyond compressed sensing for MRI reconstruction. *Magn Reson Med*. 2011;66(3):756-767. <https://doi.org/10.1002/mrm.22841>
40. Paszke A, Gross S, Chintala S, et al. Automatic differentiation in PyTorch. Paper presented at: 31st Conference on Neural Information Processing Systems (NIPS 2017); 2017; Long Beach, CA.
41. Wang Z, Bovik AC, Sheikh HR, Simoncelli EP. Image quality assessment: from error visibility to structural similarity. *IEEE Trans Image Process*. 2004; 13(4):600-612. <https://doi.org/10.1109/TIP.2003.819861>
42. Flett AS, Hasleton J, Cook C, et al. Evaluation of techniques for the quantification of myocardial scar of differing etiology using cardiac magnetic resonance. *JACC Cardiovasc Imaging*. 2011;4(2):150-156. <https://doi.org/10.1016/j.jcmg.2010.11.015>
43. Drozdal M, Vorontsov E, Chartrand G, Kadoury S, Pal C. The importance of skip connections in biomedical image segmentation. In: *Deep Learning and Data Labeling for Medical Applications*. 1st ed. Cham, Switzerland: Springer; 2016:179-187.

SUPPORTING INFORMATION

Additional supporting information may be found online in the Supporting Information section at the end of this article.

How to cite this article: El-Rewaidy H, Neisius U, Mancio J, et al. Deep complex convolutional network for fast reconstruction of 3D late gadolinium enhancement cardiac MRI. *NMR in Biomedicine*. 2020;e4312. <https://doi.org/10.1002/nbm.4312>

3.6. SUPPORTING INFORMATION

3

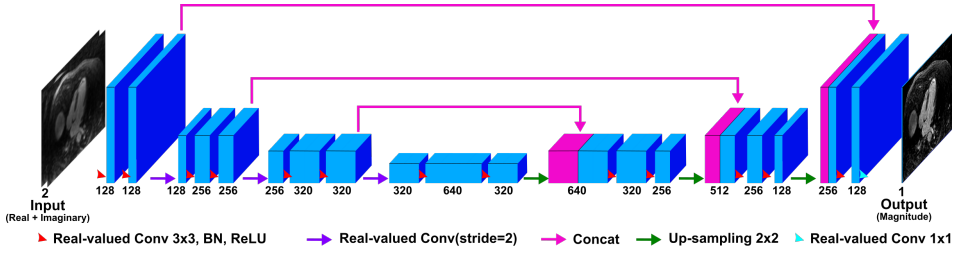


Figure 3.10: (Figure S1) RealNet architecture. Real and imaginary components of complex image data are fed as 2-channel input into real-valued convolutional layers with kernel size 3x3 with contractive and expansive paths. The contractive path includes convolutional layers of different kernel amounts (i.e. 128, 256, and 320) interleaved with 3 under-sampling stages using a convolutional layers with a stride =2 to extract high-level features at multi-resolution levels. The feature maps passed through a bottleneck convolutional layer of 640 kernels. The expansive path gradually restores the original resolution of the data through three upsampling stages; in each, the analogous feature maps from both contractive and expansive paths at each level are concatenated. Real-valued convolutional layers with a similar number of kernels in the contractive path are applied at each level. The network output is a single channel magnitude image. All convolutional layers are followed by batch normalization and ReLU, with the exception of the last convolutional layer.

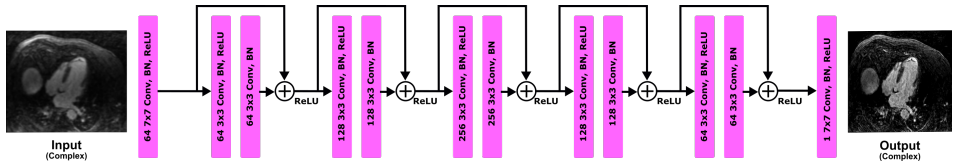


Figure 3.11: (Figure S2) ResNet architecture. The complex-valued input image is fed into an input complex convolutional layer of 64 7x7 features. Five residual blocks are deployed with 64, 128, 256, 128, and 64 3x3 kernels, respectively. The processed feature maps are combined at output layer of 1 7x7 complex convolutional kernels to generate complex artifact-free image at the network output. Radial batch normalization and complex ReLU are applied after each convolutional layer.

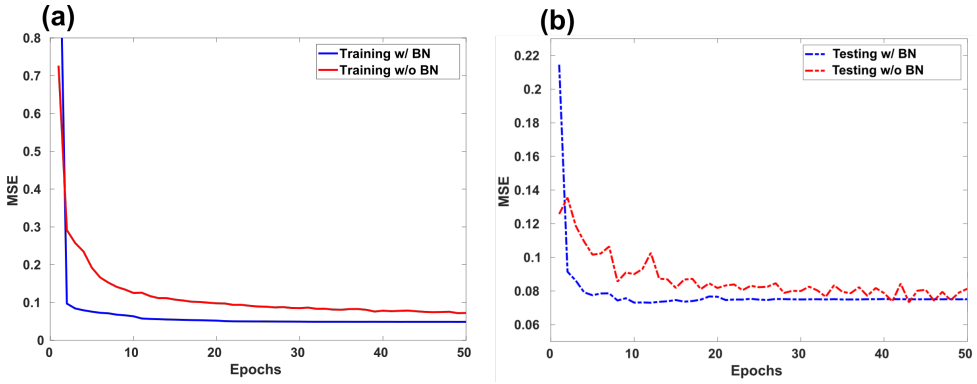


Figure 3.12: (Figure S3) Mean squared error (MSE) for CNet in (a) training and (b) testing datasets with and without radial batch normalization layers. Radial BN accelerates and stabilizes CNet convergence.

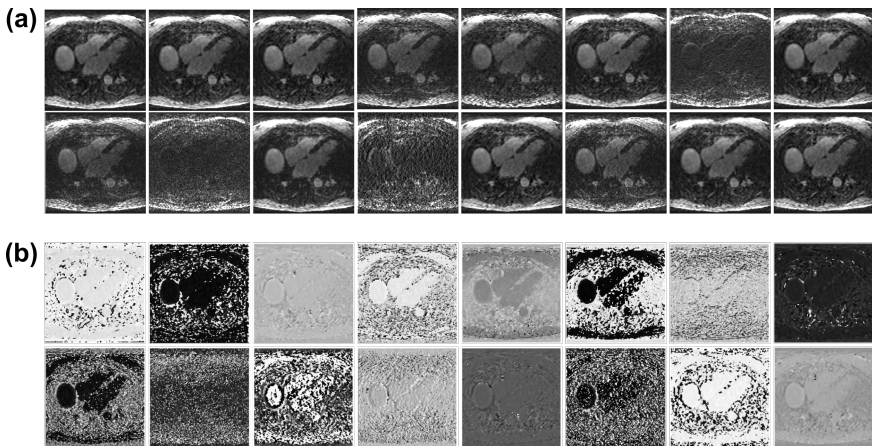


Figure 3.13: (Figure S4) Representative feature maps for the same image after applying the kernels of the first complex convolutional layer: (a) magnitude, and (b) the corresponding phase part of each feature map.

4

MULTI-DOMAIN CONVOLUTIONAL NEURAL NETWORK (MD-CNN) FOR RADIAL RECONSTRUCTION OF DYNAMIC CARDIAC MRI

Hossam El-Rewaidy, Ahmed S Fahmy, Farhad Pashakhanloo, Xiaoying Cai, Selcuk Kucukseymen, Ibolya Csecs, Ulf Neisius, Hassan Haji-Valizadeh, Bjoern Menze, Reza Nezafat, "Multi-Domain Convolutional Neural Network (MD-CNN) For Radial Reconstruction of Dynamic Cardiac MRI," *Magnetic Resonance in Medicine*, 2020. [115]

ABSTRACT


Cardiac MR cine imaging allows accurate and reproducible assessment of cardiac function. However, its long scan time not only limits spatial and temporal resolutions but is challenging in patients with breath-holding difficulty or non-sinus rhythms. To reduce scan time, in this chapter, we introduce a multi-domain convolutional neural network (MD-CNN) for fast reconstruction of highly undersampled radial cine images. MD-CNN is a complex-valued network that processes MR data in k-space and image domains via k-space interpolation and image-domain subnetworks for residual artifact suppression. MD-CNN exploits spatio-temporal correlations across timeframes and multi-coil redun-

dancies to enable high acceleration. MD-CNN reduces the scan time of cine imaging by a factor of 23.3 and provides superior image quality compared to compressed-sensing.

AUTHOR CONTRIBUTIONS

The conception of the initial idea supporting this publication, data curation and management, development and design of methodology, design and implementation of the proposed models in all experiments, statistical analysis and data interpretation, and writing and revising the manuscript.

Multi-domain convolutional neural network (MD-CNN) for radial reconstruction of dynamic cardiac MRI

Hossam El-Rewaidy^{1,2}  | Ahmed S. Fahmy¹ | Farhad Pashakhanloo¹ | Xiaoying Cai^{1,3} | Selcuk Kucukseymen¹ | Ibolya Csecs¹ | Ulf Neisius¹ | Hassan Haji-Valizadeh¹ | Bjoern Menze² | Reza Nezafat¹

¹Department of Medicine (Cardiovascular Division), Beth Israel Deaconess Medical Center and Harvard Medical School, Boston, Massachusetts, USA

²Department of Computer Science, Technical University of Munich, Munich, Germany

³Siemens Medical Solutions USA, Inc. Cary, North Carolina, USA

Correspondence

Reza Nezafat, Department of Medicine (Cardiovascular Division), Beth Israel Deaconess Medical Center and Harvard Medical School, 330 Brookline Ave, Boston, MA 02215, USA.
Email: rnezafat@bidmc.harvard.edu

Funding information

Dr. Nezafat's research is supported by grants from the National Institutes of Health 5R01HL129185, 1R01HL129157-01A1, and 5R01HL127015-02, and the American Heart Association (AHA) 15EIA22710040 (Dallas, TX, USA). Dr. Fahmy is supported by the AHA Institute for Precision Cardiovascular Medicine 19A1ML34850090 (Dallas, TX, USA). Dr. Pashakhanloo is supported by the AHA 18POST33990040 (Dallas, TX, USA). NIH grant (1R01HL154744) to Dr. Nezafat's grants. Dr. Haji-Valizadeh is supported by a NIH T32 training grant (5T32HL007374-41).

Purpose: Cardiac MR cine imaging allows accurate and reproducible assessment of cardiac function. However, its long scan time not only limits the spatial and temporal resolutions but is challenging in patients with breath-holding difficulty or non-sinus rhythms. To reduce scan time, we propose a multi-domain convolutional neural network (MD-CNN) for fast reconstruction of highly undersampled radial cine images.

Methods: MD-CNN is a complex-valued network that processes MR data in k-space and image domains via k-space interpolation and image-domain subnetworks for residual artifact suppression. MD-CNN exploits spatio-temporal correlations across timeframes and multi-coil redundancies to enable high acceleration. Radial cine data were prospectively collected in 108 subjects (50 ± 17 y, 72 males) using retrospective-gated acquisition with 80%:20% split for training/testing. Images were reconstructed by MD-CNN and k-t Radial Sparse-Sense (kt-RASPS) using an undersampled dataset (14 of 196 acquired views; relative acceleration rate = 14). MD-CNN images were evaluated quantitatively using mean-squared-error (MSE) and structural similarity index (SSIM) relative to reference images, and qualitatively by three independent readers for left ventricular (LV) border sharpness and temporal fidelity using 5-point Likert-scale (1-non-diagnostic, 2-poor, 3-fair, 4-good, and 5-excellent).

Results: MD-CNN showed improved MSE and SSIM compared to kt-RASPS (0.11 ± 0.10 vs. 0.61 ± 0.51 , and 0.87 ± 0.07 vs. 0.72 ± 0.07 , respectively; $P < .01$). Qualitatively, MD-CNN significantly outperformed kt-RASPS in LV border sharpness (3.87 ± 0.66 vs. 2.71 ± 0.58 at end-diastole, and 3.57 ± 0.6 vs. 2.56 ± 0.6 at end-systole, respectively; $P < .01$) and temporal fidelity (3.27 ± 0.65 vs. 2.59 ± 0.59 ; $P < .01$).

Conclusion: MD-CNN reduces the scan time of cine imaging by a factor of 23.3 and provides superior image quality compared to kt-RASPS.

This is an open access article under the terms of the Creative Commons Attribution-NonCommercial License, which permits use, distribution and reproduction in any medium, provided the original work is properly cited and is not used for commercial purposes.

© 2020 The Authors. *Magnetic Resonance in Medicine* published by Wiley Periodicals LLC on behalf of International Society for Magnetic Resonance in Medicine

KEYWORDS

Cardiac MRI, deep learning, image reconstruction, non-cartesian acquisition, radial acquisition, real-time imaging

1 | INTRODUCTION

Cardiac MR cine imaging with balanced steady-state free precession (bSSFP) allows accurate and reproducible measurement of cardiac function.¹ Cine images are frequently collected using electrocardiograph (ECG)-gated segmented acquisition during multiple breath-holds. For patients with breathing difficulties or non-sinus rhythms, real-time cine imaging at lower temporal and spatial resolutions is commonly acquired. A single-shot acquisition scheme is frequently used but the spatial and temporal resolution are often limited. Accelerated acquisition and advanced reconstruction can be used to increase temporal and spatial resolutions for both segmented and real-time single-shot cine imaging. Over the past two decades, there have been continuous innovations in image acceleration techniques for cardiac cine imaging, such as view-sharing,^{2,3} partial-Fourier imaging,⁴ parallel imaging,^{5,6} and compressed sensing (CS).⁷⁻¹² Parallel imaging with rate 2 accelerated cine imaging is commonly adopted in clinical routines. Recently, CS imaging has become available by vendors to reduce scan time. However, the acceleration has been limited and the reconstruction remains to be time-consuming, which hinders the clinical workflow. In addition, CS reconstruction generally requires additional state-of-the-art hardware to accommodate the higher demand for reconstruction engines.¹²

Recent advances in deep learning-based image reconstruction techniques provided yet another opportunity to achieve higher acceleration rates and improve spatial and temporal resolution in cardiac MRI.¹³⁻¹⁸ For cine imaging, both convolutional and recurrent neural networks have been used to suppress image domain aliasing artifacts in cartesian¹³⁻¹⁵ and radial^{16,19} sampling schemes. To enable high acceleration rates, temporal correlations were exploited using 3D convolutional kernels to learn spatio-temporal features in the image domain.^{13,16} In cartesian acquisitions, shared information among neighboring time frames was exploited to fill in missing k-space lines.^{13,15} Schlemper et al. used a simple k-space data-sharing strategy before applying their cascaded network by filling the missing k-space lines directly from the nearest acquired line in the neighboring frames.¹³ Although aggregating k-space lines from different time frames reduces image domain aliasing, it may increase temporal blurring at higher acceleration rates. Convolutional networks have also been used to share information across time in a multi-supervised network on cartesian k-space acquisition.¹⁵ However, the additional hyperparameters associated with the multiple

loss functions led to challenges in training, and the performance of this network degrades at high acceleration rates of ≥ 8 . To achieve higher acceleration rates, radial sampling can be used to allow more efficient coverage of k-space and offer an enhanced view-sharing strategy among time frames. However, view sharing in k-space using convolutional neural networks (CNN) has not been investigated for radial acquisitions.

In this work, we propose a multi-domain convolutional neural network (MD-CNN) for cine imaging with radial k-space sampling that processes the radial MR data in k-space, image, and time domains from multiple coils by end-to-end training. MD-CNN performance is evaluated on a retrospective gated cine imaging dataset for image quality using both quantitative and qualitative assessments.

2 | METHODS

2.1 | Network architecture

MD-CNN is a fully complex-valued CNN with two main components: k-space and image-domain subnetworks (Figure 1). Both subnetworks are trained end-to-end from scratch. The input to MD-CNN is a 4D complex-valued matrix of size $N_c \times N_{tw} \times N_x \times N_y$, representing the gridded k-space of a 2D cross-sectional image from multiple coils and across multiple consecutive time frames. N_{tw} denotes the number of time frames, and N_c denotes the number of coils.

2.1.1 | k-space subnetwork

The function of this subnetwork is to refine estimations of the 2D gridded k-space data using convolutional kernels. Missing k-space data are estimated by interpolation of the acquired MR data using multiple convolutional kernels. Correlations across time frames are also exploited in the form of view-sharing via 3D convolutional kernels applied on the 2D gridded k-space and a window of neighboring time frames (N_{tw}). The k-space subnetwork consists of two identical residual blocks of cascaded convolutional layers. Each k-space block consists of three 3D complex-valued convolutional layers (XConv)²⁰ with $2N_c$, $2N_c$, and N_c kernels each of size $3 \times 5 \times 5$; where N_c is the number of coils. A complex rectified linear unit (XReLU) follows each convolutional layer. A residual connection is added after each k-space block to reduce the

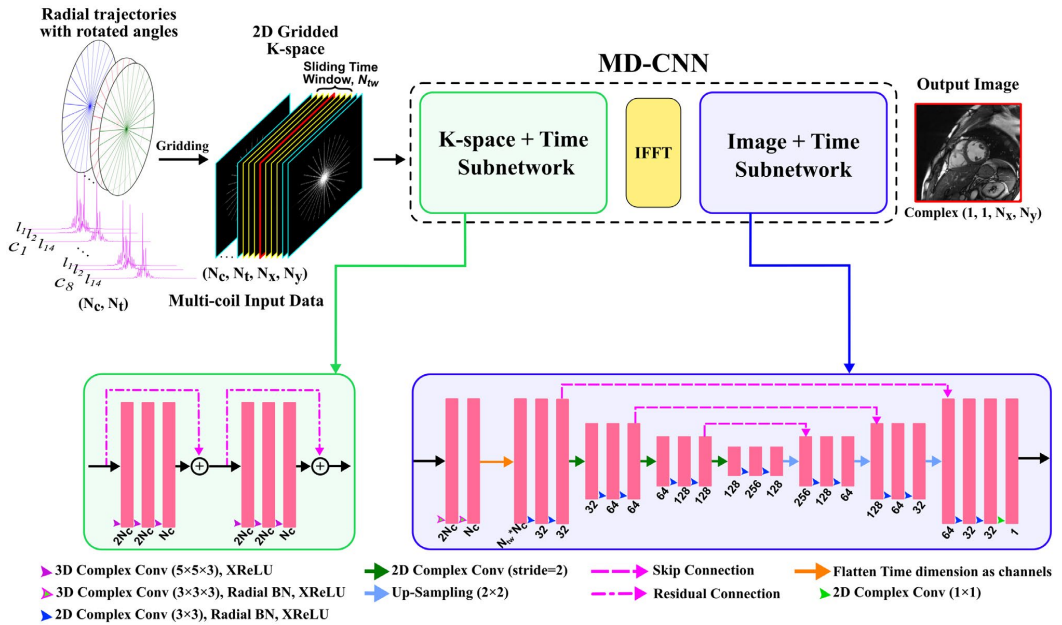


FIGURE 1 Proposed multi-domain convolutional neural network (MD-CNN) pipeline. The k-space data from N_c coils acquired with radial trajectories are gridded onto the cartesian grid using NUFFT. To reconstruct the frame (red), multi-coil 2D k-space data from N_{tw} adjacent time frames (yellow) are fed into the MD-CNN. The output of the MD-CNN is a coil-combined reconstructed image for the target frame. MD-CNN consists of two subnetworks: k-space and image-domain. The k-space subnetwork takes complex-valued 2D k-space input data of size (N_c, N_{tw}, N_x, N_y) to be processed by two identical residual blocks. Each block consists of three complex convolutional layers with 3D kernels of size $(3 \times 5 \times 5)$. Each convolutional layer is followed by a complex rectified linear unit (XReLU) for activation. The resulting k-space data is transformed into the image domain by inverse fast Fourier transform (IFFT). In the image subnetwork, data are fed into two convolutional layers with 3D kernels of size $(3 \times 3 \times 3)$ to exploit spatio-temporal correlations. The time dimension in the resulting 3D feature maps are flattened into channels to produce 2D feature maps of size $(N_c N_{tw}, N_x, N_y)$. A 2D U-net is then used to process the 2D feature maps from N_c coils and N_{tw} frames to reconstruct a coil-combined reconstructed image

large dynamic range of k-space values. The resulting k-space data are then transformed into the image domain using inverse fast Fourier transform (FFT).

2.1.2 | Image domain subnetwork

In the image domain, shared structural information among neighboring time frames is exploited by two 3D XConv layers consisting of $2N_c$ and N_c kernels each of size $3 \times 3 \times 3$ with radial batch normalization (RBN) and XReLU.²⁰ The resulting 3D maps (ie, 2D+time; size of $N_c \times N_{tw} \times N_x \times N_y$) are projected in the 2D space, where time frames are flattened into channels to produce 2D feature maps.

A 2D U-Net architecture is then used to remove residual artifacts and combine data from different time frames and coils into a coil-combined output image. The U-Net subnetwork consists of contracting and expanding paths that can remove image artifacts at multiple resolutions. In the contracting path, three stages of spatial down-sampling are

applied consisting of two 2D XConv, RBN, and XReLU layers at each stage. The number of kernels doubles after each down-sampling stage (32, 64, and 128, respectively). The resulting feature maps pass through two XConv layers of 256 and 128 kernels of size 3×3 , respectively. The expansive path maps the output at each down-sampling stage to an analogous stage of similar map size and kernel number using skip connections. Up-sampling layers are used to increase the size of feature maps by a factor of 2 at each up-sampling stage to provide a clean version of the artifact-contaminated images at different resolution levels. The final feature maps are combined using the XConv layer of one 1×1 kernel to generate a coil-combined complex-valued reconstructed image.

2.2 | Data acquisition

The study was approved by the Beth Israel Deaconess Medical Center Institutional Review Board (IRB number 2001P000793). All imaging was performed on a 3T

system (MAGNETOM Vida, Siemens Healthcare, Erlangen, Germany) using body and spine phased-array coils. Radial bSSFP cine data were acquired in 101 patients and 7 healthy subjects (108 total subjects; age 50 ± 17 y, 72 males, heartbeats 72 ± 15 beats/min, and weight 80.6 ± 18 kg). Participants provided written informed consent to use cardiac MRI studies for research purposes. The indications for clinical CMR scans for our cohort are reported in Supporting Information Table S1, which is available online. A mid-ventricular slice was imaged during breath-holding with the following imaging parameters: repetition time/echo time (TR/TE) = 3.06/1.4 ms, field of view = 380×380 mm², matrix size = 208×208 , in-plane resolution = 1.8×1.8 mm², slice thickness = 8 mm, flip angle = 48°, number of channels = 16 ± 1 , and retrospective ECG-triggering with 25 cardiac phases calculated. In each patient, 196 radial views were acquired on average per cardiac phase with a breath-hold duration of ~14 heartbeats.

2.3 | Data preparation

The dataset was randomly divided into training (87 subjects) and testing (21 subjects) subsets. The complex-valued reference images at each time frame were reconstructed with all acquired 196 radial views per frame using non-uniform fast Fourier transform (NUFFT) implemented on the scanner,²¹ where the complex-valued images were saved before writing the DICOM images. An undersampled dataset was synthesized by selecting a small set (eg, $N_v = 14$ views) from the acquired 196 radial views at each time frame; such that an equivalent acquisition duration of one heartbeat per slice

is achieved. The effective acceleration rate is 23.3 based on the Nyquist sampling requirement ($208 \times \frac{\pi}{2} = 327$ views).²² To create an undersampled dataset, radial views across a 14-spokes radial trajectory (T_{14}) were selected from the acquired highly sampled radial data (ie, 196 spokes). First, the uniform angles of T_{14} are calculated and matched to the nearest 14 angles of the 196-spokes trajectory (Figure 2). The selected 14 angles are considered as the undersampled trajectory.

To create rotated angles trajectory among different frames, T_{14} was rotated in each frame, p , with an angle $\theta_p = \frac{p\pi}{N_v N_{tw}}$, where p is the frame index ($p = 0, 1, \dots, 24$), N_{tw} is a window of neighboring time frames (eg, $N_{tw} = 7$), and N_v is the total number of acquired views (eg, 196) (Figure 2). To enable optimized k-space coverage for data sharing among consecutive N_{tw} frames, the rotating angle θ_p also maintains uniform angular distance among all views from the N_{tw} neighboring frames. Gradient delay induced errors in the radial trajectory were automatically corrected using the RING method²³ implemented from the Berkeley Advanced Reconstruction Toolbox (BART).²⁴ Gradient delays were corrected in each time frame using only the selected 14 radial views.

The radial k-space of each frame and each coil was reconstructed using inverse NUFFT. Coil compression was applied to obtain a fixed number of coils ($N_c = 8$) per frame using BART.²⁵ Complex-valued gridded data from consecutive time frames of window size, $N_{tw} = 7$, with eight coils per frame were normalized in the image domain using RBN. Considering the periodic nature of the dynamic cardiac imaging, information can be shared from the last frames of the dynamic cine imaging to reconstruct the first frames and vice versa. For example, to reconstruct the first frame, a window

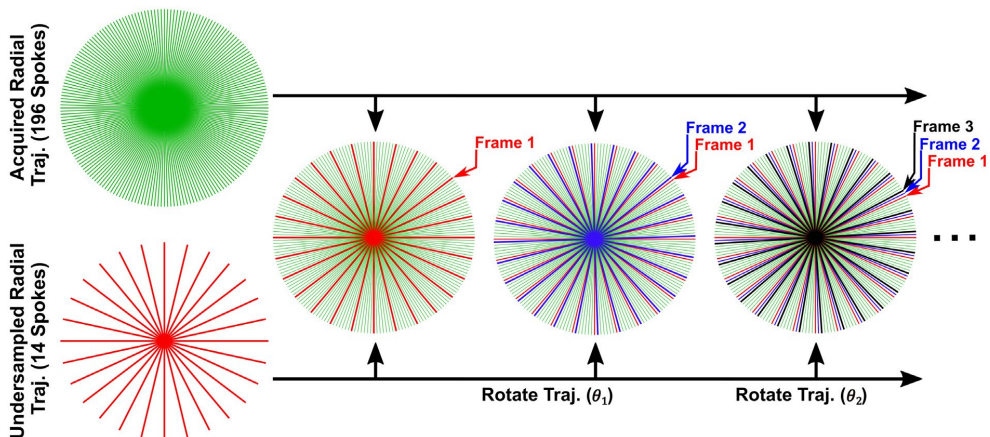


FIGURE 2 Radial undersampling using uniform-angle rotating radial trajectories. An undersampled uniform radial trajectory of 14 spokes is selected from the acquired highly sampled radial data (196 spokes). The radial trajectory in a frame p is rotated with an angle $\theta_p = \frac{p\pi}{N_v N_{tw}}$, where N_v is the number of views per frame (eg, 14 spokes), and N_{tw} is the number of neighboring time frames (eg, seven frames). The undersampled radial lines from N_{tw} consecutive time frames have a uniform angular-spacing trajectory that allow optimal k-space coverage for data sharing

of neighboring frames at indices {23, 24, 25, 1, 2, 3, and 4} is included at the network input. Next, FFT was applied to obtain 2D k-spaces fed into MD-CNN to reconstruct the coil-combined image at a single time frame (ie, corresponding to the middle frame of the input window $\left\lfloor \frac{N_{tw}}{2} \right\rfloor$).

2.4 | Network training

MD-CNN was trained with 250 epochs via a stochastic gradient descent SGD optimizer with a momentum of 0.9 and learning rate function $0.01^{\lfloor epoch/50 \rfloor + 1}$, where the learning rate exponentially decreases with the number of epochs. The batch number was 15 complex-valued data points of size $8 \times 7 \times 208 \times 208$. The mean-squared error loss function was applied to minimize reconstruction error between MD-CNN predictions and reference images at any time frame, t , such that:

$$\min_{\Theta_k, \Theta_m} \left\| M_{xy}(t) - \Psi(A\Phi(K_{xyw}(t)|\Theta_k)|\Theta_m)_{xy} \right\|_2^2,$$

where $M_{xy}(t)$ is a complex-valued, coil-combined reference image at a single time point, t , reconstructed using all 196 acquired radial views, $t \in [0, 1, \dots, 24]$; $K_{xyw}(t)$ is a complex-valued, multi-coil 2D spatial k-space gridded from undersampled radial acquisitions at N_{tw} time frames (ie, 2D k-space + time); A is the Fourier encoding matrix of the 2D FFT; $\Phi(\cdot)$ is a nonlinear interpolation function controlled by trainable parameters, Θ_k ; and $\Psi(\cdot)$ is a non-linear mapping function controlled by trainable parameters, Θ_m , which take N_{tw} time frames as input to reconstruct a single frame at the output. The same network parameters, Θ_k and Θ_m , were trained using all time frames. During MD-CNN training, time frames from all patients in the training dataset were randomized and 15 (ie, batch size) frames from different patients were selected to be reconstructed in each training iteration.

MD-CNN was implemented in Python using the PyTorch library version 0.41.²⁶ All models in this work were trained and tested on an NVIDIA DGX-1 system equipped with 8T V100 graphics processing units (GPUs; each of 32 GB memory and 5120 cores), central processing unit (CPU) of 88 core: Intel Xeon 2.20 GHz each, and 504 GB RAM. Only four GPUs were used to train MD-CNN. The total MD-CNN training time was 24 h.

2.5 | Performance evaluation

To investigate the impact of the window size N_{tw} of input time frames, MD-CNN performance was evaluated on testing dataset reconstructed at three different window sizes (N_{tw}

= 5, 7, and 9 frames), where MD-CNN was trained from scratch at each window size. The performance of MD-CNN was compared with a compressed-sensing based k-t Radial Sparse-Sense (kt-RASPS) reconstruction method, which exploits the temporal sparsity of the data.^{11,27} The same undersampled dataset prepared for MD-CNN was used for kt-RASPS reconstruction where 14 views, corresponding to a temporal resolution of 42.8 ms, were selected per frame with a uniform-angle rotating among different frames. The kt-RASPS algorithm was implemented using the parallel imaging and compressed sensing tools in BART with GPUs and parallel processing. Coil sensitivities were calculated using the ESPIRiT method.²⁵ kt-RASPS parameters were optimized on 10 randomly selected subjects from the training dataset, where images were evaluated to determine the optimal value of the regularization level and number of iterations. kt-RASPS performance was evaluated over a range of regularization levels (λ) from 0.01-0.1 with a step of 0.005 and number of iterations ranging from 25 to 100, with 25 steps. MD-CNN performance was also compared to the CS-based method proposed by Miao et al.,²⁸ in which a combination of locally low rank (LLR) and temporal finite differences (FD) were used as regularization terms. This method was used to reconstruct the same undersampled dataset of 14 views/frame with regularization parameters $\lambda_{LLR} = 0.06$ and $\lambda_{FD} = 0.006$.

To evaluate MD-CNN performance compared to other deep learning frameworks, a 3D U-net network¹⁶ was used to reconstruct the same undersampled data (ie, 14 spokes). This network consisted of contracting and expanding paths with two stages of spatio-temporal down-sampling and up-sampling in each path, respectively. The radial cine data from all time frames was gridded using NUFFT, coil-combined, and fed into the U-net as a 3D volume in the image domain of size $208 \times 208 \times 24$ (ie, 2D + time) with real and imaginary components as different channels. To allow down-sampling and up-sampling of the temporal dimension inside the network, the temporal dimension of the input and reference data was reduced to 24 frames (compared to the original data of 25 frames) using linear interpolation of all time frames. The mean-squared error loss function was used to train this network using the stochastic gradient descent optimizer with a learning rate of 0.01 and 350 epochs.

MD-CNN and kt-RASPS performance was evaluated by quantitative and qualitative measures. Mean squared error (MSE) and structural similarity index measure (SSIM) were calculated for MD-CNN, U-net and kt-RASPS with respect to the reference images. The magnitude values of all images are normalized by the 90th percentile before assessment. Edge sharpness of left ventricular (LV) borders was quantitatively evaluated across six LV myocardial segments (based on the AHA 16-segment model) in all time frames. In each segment, edge sharpness was calculated as the maximum gradient of the normalized intensity profile (between 0 and 1) across this

segment. To avoid misleading gradients produced by noise, each intensity profile was fit to a high-order polynomial function of order 10.

For qualitative assessment, three readers (U.N., S.K., and I.C. with > 5 y of experience in cardiovascular imaging) blinded to the reconstruction methods independently assessed images reconstructed by MD-CNN, kt-RASPS, and the reference based on four different metrics: (a-b) the sharpness of LV borders at end-diastolic (ED) and end-systolic (ES) phases, (c) temporal fidelity of LV wall motion using a 5-point Likert scale (1-non-diagnostic, 2-poor, 3-fair, 4-good, and 5-excellent), and (d) residual image artifacts in the entire field-of-view on a 5-point scale (1-minimal, 2-mild, 3-moderate, 4-severe, and 5-non-diagnostic).

Endocardial and epicardial LV myocardial borders from MD-CNN, kt-RASPS, and reference images in ED and ES frames were manually delineated by all readers. LV myocardium (ie, areas between endocardial and epicardial contours) and LV blood pool cavity were calculated from the extracted contours for the three datasets (ie, reference, kt-RASPS, and MD-CNN). To further investigate the effect of LV border sharpness on manual delineation, we calculated the DICE index between kt-RASPS vs. reference and MD-CNN vs. reference for the LV myocardium and LV blood cavity at the ED and ES phases.

2.6 | Data analysis

Normal data distributions were expressed in the form of mean \pm SD. The two-sided Student's *t*-test compared continuous variables between different reconstruction methods. Analysis of variance or Kruskal-Wallis tests were used as appropriate for comparison of multiple groups. For comparison of categorical data, the Chi-squared test was used. Significance was declared at two-sided *P*-values < .05. For pairwise comparisons following a three-group inferential test, a Bonferroni correction was used. Bland-Altman plots assessed agreement between different readers. Statistical analyses were conducted using MATLAB (2017a, The MathWorks Inc., Natick, Massachusetts, United States).

3 | RESULTS

MD-CNN performance increased as window size increased, as indicated by the decreasing MSE (0.125 ± 0.09 , 0.11 ± 0.1 , and 0.106 ± 0.1) and increasing SSIM (0.85 ± 0.072 , 0.87 ± 0.067 , and 0.87 ± 0.062) for $N_{tw} = 5, 7$, and 9 , respectively. MD-CNN reconstructed data also showed similar temporal fidelity for the three window sizes with increased flickering artifacts at $N_{tw} = 5$ compared to seven and nine frames (Supporting Information Video S1). A window size

of seven frames was, therefore, used in the rest of our experiments due to its similar performance to $N_{tw} = 9$ with lower reconstruction time and memory requirements, and improved performance compared to $N_{tw} = 5$. Supporting Information Figure S1 shows the MSE for MD-CNN images in the training and testing datasets at each of the 250 training epochs. Both training and testing MSE consistently decreased as the number of training epochs increased, indicating a robust performance and minimal overfitting of the MD-CNN. Parameters tuning for kt-RASPS yielded minimal streaking artifacts and maximal temporal fidelity at $\lambda = 0.025$ and #iterations = 50 (Supporting Information Videos S2 and S3).

Figure 3 shows examples from two subjects and compares the images (and their corresponding k-space) after different stages of the MD-CNN reconstructions. Comparing the input and output of the 1st and 2nd blocks of the k-space subnetwork (columns 1–3), the k-space convolutional subnetwork gradually estimated the missing data at more k-space locations by interpolating values near the acquired k-space data and neighboring time frames. K-space interpolation reduced streaking artifacts in the corresponding images while maintaining image sharpness. The image subnetwork further reduced streaking artifacts and improved image sharpness and contrast (column 4). The final MD-CNN-reconstructed images demonstrated a similar contrast as the reference images (column 5).

Cine images from undersampled radial data were reconstructed by NUFFT, kt-RASPS, U-net, and MD-CNN compared to the reference images (Figure 4). MD-CNN, U-net, and kt-RASPS reconstructions showed less pronounced streaking artifacts than NUFFT images. Similar to reference images, MD-CNN images preserved anatomical sharpness and contrast of the myocardium compared to kt-RASPS, and less residual artifacts compared to U-net. Cine imaging movies for two additional cases reconstructed by LLR+FD, kt-RASPS, MD-CNN, and reference showed improved temporal fidelity of MD-CNN network compared to CS methods (Supporting Information Videos S4 and S5) and reduced residual streaking artifacts compared to the 3D U-net. Figure 5 shows MD-CNN reconstructions from one subject at different undersampling rates: 14, 16, and 20 spokes per frame compared to the corresponding reference image. X-t plots and Supporting Information Video S6 showed increased temporal fidelity as undersampling rate decreases indicated by less blurring in the LV wall at 20 spokes compared to reconstructions with 14 spokes per frame.

MD-CNN showed lower MSE and improved SSIM compared to kt-RASPS and U-net ($P < .01$ for both) (Table 1). The intensity profiles of MD-CNN reconstructed images also showed higher sharpness across the blood-myocardium at different segments than kt-RASPS at ED and ES frames (Figure 6, and Supporting Information Figure S2, respectively). MD-CNN maintained the blood-myocardium

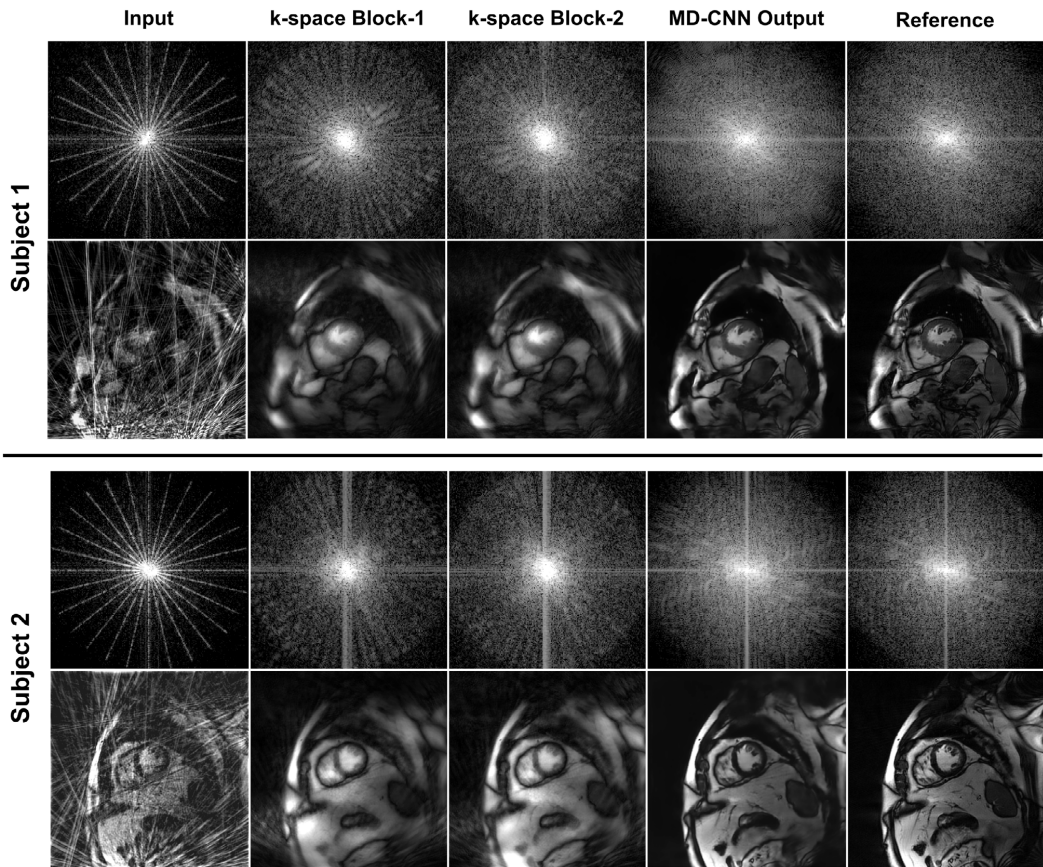


FIGURE 3 Performance of the k-space subnetwork in two subjects. The k-space data are shown at different stages of the network: the gridded input k-space, after the 1st and 2nd residual blocks of the k-space subnetwork, the k-space of MD-CNN reconstruction, and the k-space of the reference image (rows 1 and 3). The corresponding images are also shown (rows 2 and 4). The k-space gaps are gradually filled and the corresponding streaking artifacts of input images are suppressed after k-space interpolation in 1st and 2nd k-space blocks (columns 2 and 3). The final MD-CNN reconstructed images have further reduced artifacts and improved image quality similar to the reference images. The k-space of the input, k-space block-1, and kspace block-2 are taken from a single coil. All k-space data are presented on a logarithmic scale

contrast of small anatomic structures such as papillary muscles, as indicated by the intensity profiles in segment 4 of Figure 6. Per-segment LV sharpness is illustrated in the bull's-eye plot with mean \pm SD for each segment calculated over all time frames in the testing dataset. MD-CNN images had better LV sharpness in all segments compared to kt-RASPS ($P < .01$) (Table 1).

Qualitative assessments of LV border sharpness, temporal fidelity, and residual artifacts are reported in Table 2. The sharpness of the LV myocardium at end-diastole and end-systole was significantly improved in MD-CNN reconstruction compared to kt-RASPS reconstruction (3.87 ± 0.66 vs. 2.71 ± 0.58 , and 3.57 ± 0.58 vs. 2.56 ± 0.60 for end-diastole and end-systole, respectively; P -value $< .01$). LV myocardium sharpness was higher in ED frames compared to ES

MD-CNN and kt-RASPS, potentially due to less cardiac motion at end-diastole. MD-CNN reconstructed images exhibited less temporal LV wall blurring compared to kt-RASPS (P -value $< .01$). Residual artifacts were reduced in MD-CNN images indicating the network's ability to recover image sharpness while suppressing artifacts.

The percentage error of the extracted LV myocardial area in MD-CNN images was lower than in kt-RASPS images, with a 9% and 4% decrease at ED and ES frames relative to reference images, respectively (P -value $< .01$) (Table 3). The LV cavity area extracted from MD-CNN also showed improved DICE index and reduced percentage error compared to that of the kt-RASPS images at both ED and ES frames with respect to the reference images. Figure 7 and Supporting Information Figure S3 shows agreement between

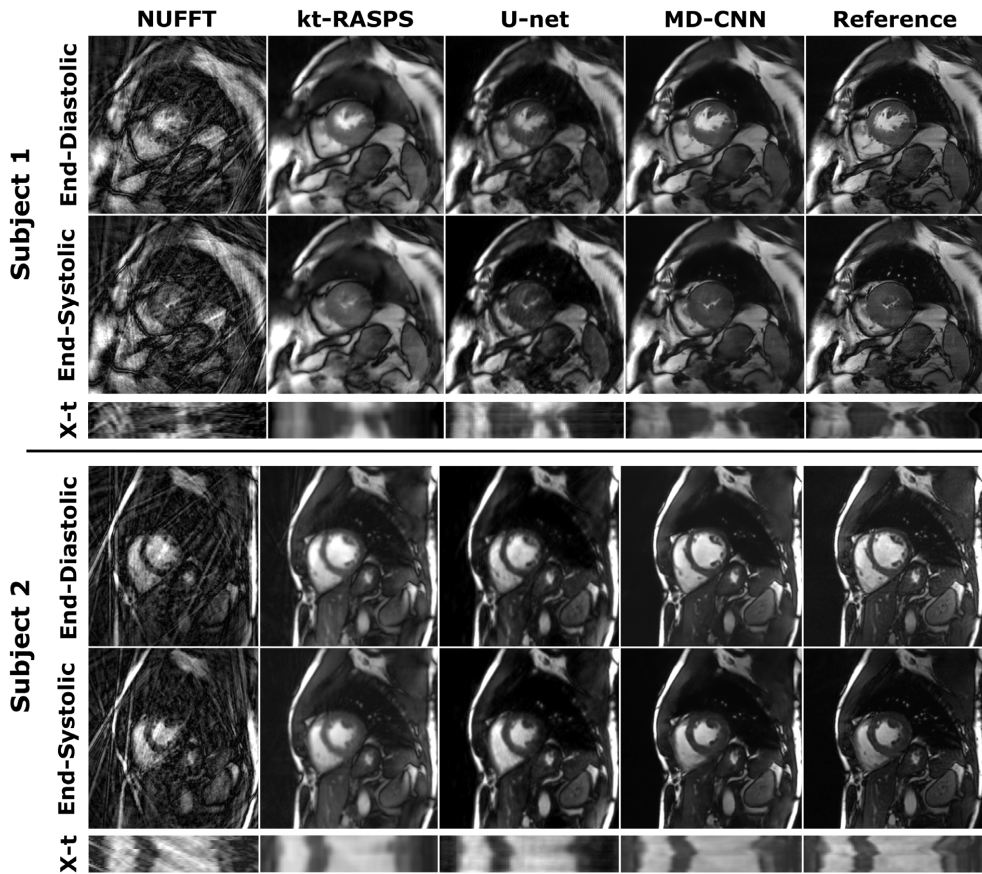


FIGURE 4 Representative reconstructions by NUFFTT, kt-RASPS, U-net, and MD-CNN compared to the reference images for two subjects at end-diastolic and end-systolic phases, as well as x-t plots across all time frames

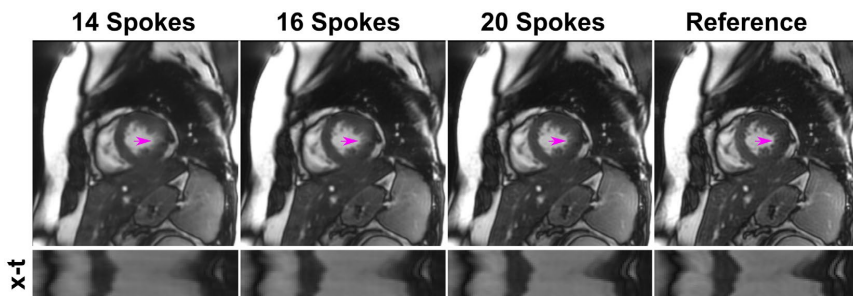


FIGURE 5 Representative reconstruction by MD-CNN at different undersampling rates: 14, 16, and 20 spokes per frame compared to reference image. X-t plots of the reconstructed images at each undersampling rate (bottom row) shows the temporal fidelity across all time frames. Temporal fidelity increases as undersampling decreases (magenta arrows)

readers segmenting the LV myocardial area from kt-RASPS, MD-CNN, and reference images. MD-CNN showed higher agreement between readers (ie, smaller limits of agreement)

similar to that of reference images (Supporting Information Table S2). MD-CNN takes 1.6 ± 0.35 s to reconstruct a set of 25 frames of one slice compared to 5.4 ± 1.1 s for kt-RASPS.

TABLE 1 Quantitative assessment of image quality by mean-squared error (MSE), structural-similarity index measure (SSIM), and LV myocardial sharpness for kt-RASPS, 3D U-net, and MD-CNN reconstructed images with respect to the reference

Method	kt-RASPS	U-net	MD-CNN	Reference	P-value
MSE	$0.61 \pm 0.51^*$	0.13 ± 0.16	0.11 ± 0.10	–	<.01
SSIM	$0.72 \pm 0.07^*$	$0.84 \pm 0.08^*$	0.87 ± 0.067	–	<.01
Quantitative LV myocardial sharpness	$0.12 \pm 0.04^{\S}$	$0.16 \pm 0.06^{\S}$	$0.17 \pm 0.06^{\S}$	0.21 ± 0.07	<.01

All values are reported as mean \pm SD.

§ P-value < .01 compared to Reference; *P-value < .01 compared to MD-CNN.

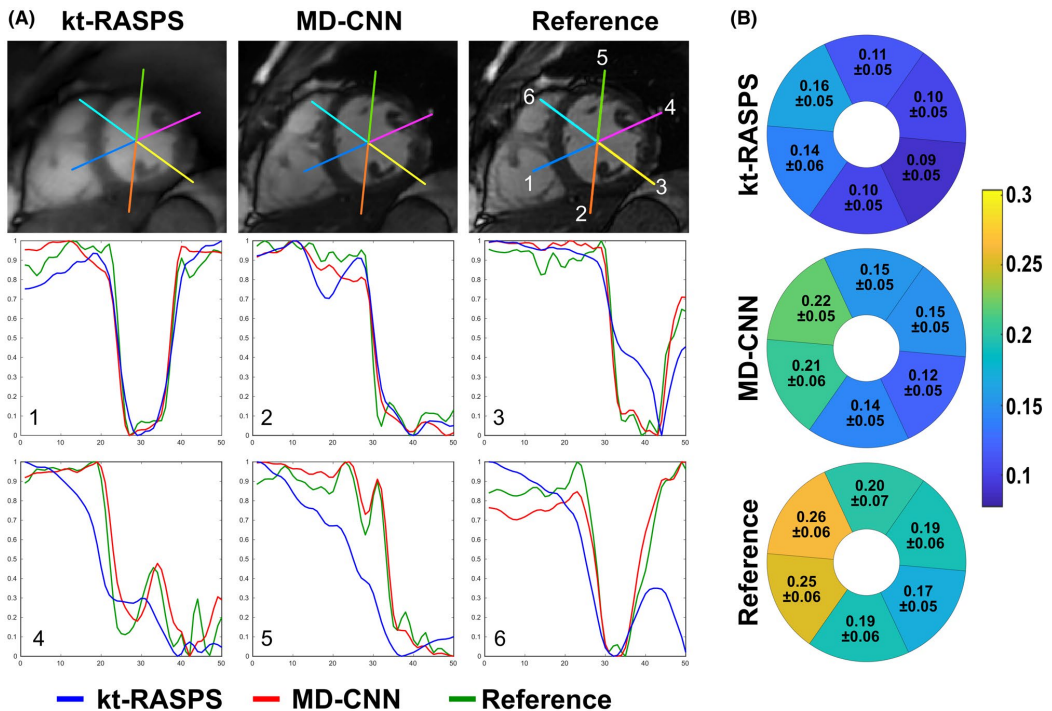


FIGURE 6 Quantification of the left ventricular (LV) edge sharpness at six myocardial segments in GRAS, MD-CNN, and reference images. A, Sample reconstructed images at end-systole by the three methods (kt-RASPS, MD-CNN, and Reference) showing the six segments at which LV sharpness was quantified and the intensity profiles corresponding to each segment of the sample images. B, The bull's eye plot shows the value of the quantified LV edge sharpness at the six different segments of the myocardium with mean \pm SD calculated over all time frames of the testing dataset

4 | DISCUSSION

In this study, we developed a multi-domain network that processes MR data in both k-space and image domains with an end-to-end training process. In general, all k-space operations can be performed in the image domain and vice versa; for example, convolving a kernel to an image is equivalent to multiplying this kernel's response to the k-space of that image. However, in the context of CNN, all operations are based on convolutional kernels only; hence, certain operations are

feasible to be performed in the k-space and others in the image domain using CNN. The k-space subnetwork performs an interpolation of the input 2D k-space using shared information among adjacent frames to provide an enhanced estimation of missing k-space data, particularly at locations far from the acquired radial lines (ie, gaps among radial lines). Filling such k-space gaps is crucial for suppressing image domain's streaking artifacts. Although conventional gridding techniques use single hand-crafted kernel to interpolate MR signals at all k-space locations, the performance of such kernels degrades

Method	kt-RASPS	MD-CNN	Reference
Sharpness of LV borders at end-diastole	2.71 ± 0.58* [§]	3.87 ± 0.66 [§]	4.71 ± 0.52
Sharpness of LV borders at end-systole	2.56 ± 0.60* [§]	3.57 ± 0.58 [§]	4.60 ± 0.58
Temporal fidelity of wall motion	2.59 ± 0.59* [§]	3.27 ± 0.65 [§]	4.65 ± 0.51
Residual artifacts	2.63 ± 1.09 [§]	2.38 ± 0.81 [§]	1.81 ± 0.82

[§]P-value < .01 compared to Reference;

*P-value < .01 compared to MD-CNN.

Method	Phase	kt-RASPS	MD-CNN	P-value
DICE index of LV myocardium	Diastole	0.77 ± 0.12	0.84 ± 0.05	<.01
	Systole	0.83 ± 0.06	0.88 ± 0.07	<.01
DICE index of LV endocardium	Diastole	0.97 ± 0.01	0.98 ± 0.03	.011
	Systole	0.96 ± 0.01	0.97 ± 0.01	<.01
Percentage error of LV myocardial area (%)	Diastole	21.4 ± 19.1	12.0 ± 13.1	<.01
	Systole	13.8 ± 13.3	9.4 ± 8.0	<.01
Percentage error of LV endocardial area (%)	Diastole	4.5 ± 4.0	3.6 ± 3.3	.15
	Systole	7.3 ± 6.2	5.2 ± 4.3	<.01

rapidly at higher acceleration rates, leaving large k-space gaps and hence more streaking artifacts. The amount and shape of such artifacts are largely determined by the design of the gridding kernel and the undersampling rate. CNN, on the other hand, offers an efficient k-space interpolation strategy that optimizes multiple convolutional kernels on many training samples to determine the proper interpolation weights specific to the undersampling scheme used. Additionally, the non-linear activation functions used after each convolutional layer in CNN may allow a spatially variant interpolation process, in which the high- and low-frequency k-space content can be interpolated differently.

Considering that successive time frames have similar structural information, k-space interpolation across the time dimension (using 3D convolution kernels) also allows spoke sharing among neighboring frames with similar image content. Data sharing in turn allows for better estimation of k-space values at more locations on k-space gaps, thereby reducing streaking artifacts. To exploit shared information across the time dimension in the form of spokes sharing, the radial trajectory was rotated from frame to frame at a small angle (1.8°) that maintained a uniform angular spacing among neighboring frames.^{29,30} The importance of k-space processing in our network was demonstrated by assessing the resulting k-space of each residual block in the k-space subnetwork. The blocks of the k-space subnetwork gradually filled the missing values in k-space and led to significantly reduced streaking artifacts in the reconstructed images while maintaining fine image details and sharpness.

TABLE 2 Qualitative assessment of LV border sharpness at end-diastolic and end-systolic cardiac phases, temporal fidelity of myocardial wall motion, and residual artifacts in kt-RASPS, MD-CNN, and reference images

TABLE 3 DICE index and percentage error of LV myocardial and endocardial areas at end-diastolic and end-systolic phases extracted from kt-RASPS and MD-CNN images with respect to reference images

The refined k-space data are transformed into the image domain using inverse FFT for further processing via the image-subnetwork. To guarantee a proper flow of gradients between the two subnetworks for the back-propagation algorithm during training, a differentiable FFT operation was implemented using native PyTorch functions. Maintaining complex-valued MR data throughout the MD-CNN intermediate layers was also necessary to allow a proper transformation of data between the k-space and image domain. To process complex-valued data, a complex convolutional network was used to maintain the proper combination of real and imaginary components of complex MR data throughout all network layers.

In the image-subnetwork, the improved myocardium-blood contrast, artifact suppression, and sharp edges in the MD-CNN output images are likely associated with the ability of the image-subnetwork to compensate for variable k-space density and suppress more residual artifacts. Considering the incoherent residual (streaking) artifact patterns among different frames, the 3D convolution layers in this subnetwork enable further removal of residual artifacts by sharing spatio-temporal correlations among neighboring frames, similar to compressed sensing.^{12,16}

MD-CNN images had superior image quality than kt-RASPS and U-net on all quantitative measures. MD-CNN was trained to produce images that minimally differ from reference images in pixel value, such that quantitative measures are implicitly biased toward the MD-CNN-reconstructed images compared to kt-RASPS images. To alleviate this

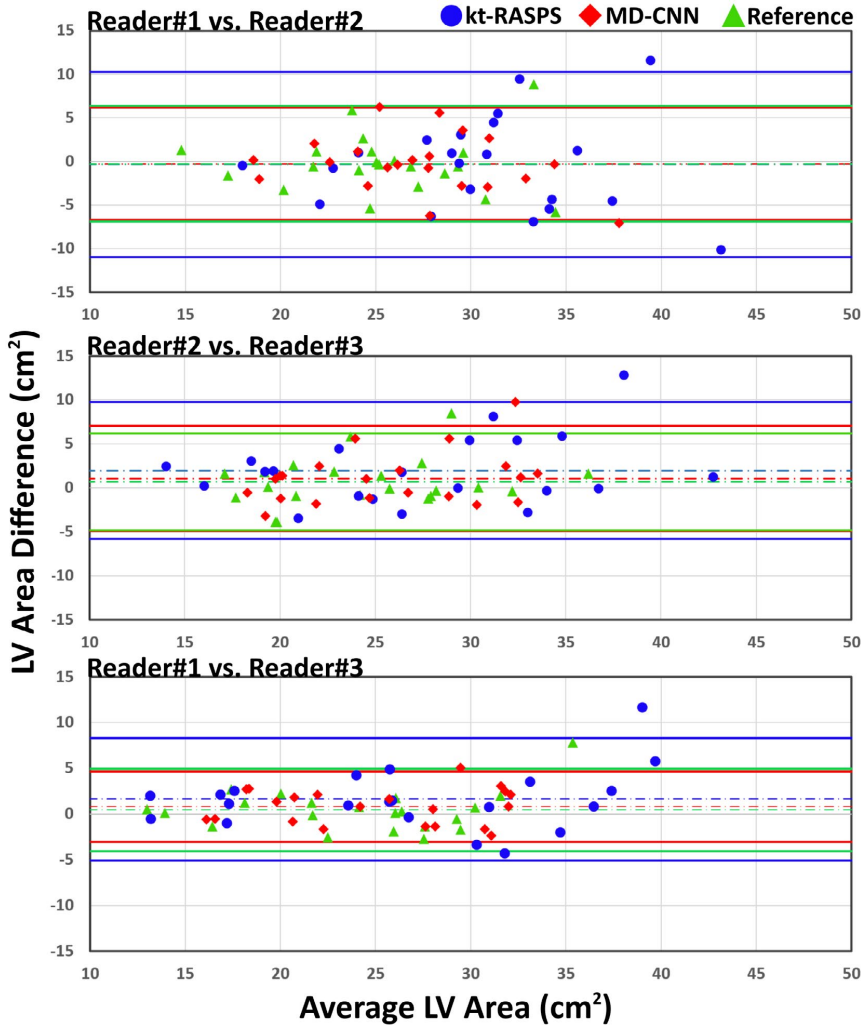


FIGURE 7 Bland-Altman plots showing inter-observer agreement of three comparisons: Reader 1 vs. Reader 2, Reader 2 vs. Reader 3, and Reader 1 vs. Reader 3 of the extracted LV myocardial areas in kt-RASPS, MD-CNN, and reference images. Biases and limits of agreement for each comparison are reported in Supporting Information Table S2

bias, kt-RASPS, MDC-CNN, and reference images were normalized by the 90th percentile before MSE and SSIM calculations. In addition, to alleviate the impact of myocardium-blood contrast differences on LV sharpness quantifications, each intensity profile across the LV myocardium was standardized separately from 0 to 1 before the sharpness calculations. In addition, MD-CNN allows further suppression of the residual streaking artifacts compared to the 3D U-net. This is mainly due to the ability of the k-space interpolation subnetwork to provide cleaner images to the image-domain subnetwork, unlike the U-net that processes cine data in the image domain only.

In the qualitative assessment, MD-CNN images also demonstrated improved LV edge sharpness at ED and ES phases and reduced temporal blurring compared to kt-RASPS images. This was also indicated by greater agreement among readers assessing the extracted LV areas from MD-CNN vs. kt-RASPS reconstruction. These results also reflect higher confidence among readers to accurately segment the sharp LV borders from MD-CNN images. Although the temporal fidelity of MD-CNN reconstruction at 14 views was assessed as fair by the readers, higher temporal fidelity can be obtained by including more views (optimally observed at 20 views per frame). Both methods

showed similar residual artifact content, but the artifacts were different in nature. Kt-RASPS endorsed streaking artifacts, while flickering artifacts were observed in MD-CNN.

A few considerations may have contributed to inferior reconstruction by kt-RASPS in this study. The kt-RASPS method is more suitable for real-time imaging applications where a large number of frames are available ($\gg 25$), so that sufficient sparsity along the time dimension is achieved. However, in our reconstruction problem, only 25 phases were available for reconstruction, which may have led to additional blurring in kt-RASPS images. The limited number of frames in our data also led to faster kt-RASPS reconstruction times compared to the real-time applications.¹² On the other hand, the proposed MD-CNN method is able to exploit redundancy in a small number of adjacent frames (seven in the experiments) and thereby efficiently reduce undersampling artifacts. In addition, the rotation angle in this study is uniform, as opposed to the golden-angle rotation that is widely used in real-time applications.^{12,22} However, the uniform trajectories exhibit better characteristics that allow equidistant spacing between views when compared to golden-angle trajectories.

Our study has some limitations. Only one slice at mid-LV was acquired per patient, which was not sufficient to calculate LV functional parameters (eg, LV volumes and ejection fraction). All patients studied were in sinus rhythm, and generalization of the reconstruction techniques in patients with irregular rhythms was not studied.

5 | CONCLUSION

The proposed multi-domain network uses k-space and image domain processing units to efficiently reconstruct highly undersampled radial cine MR data. MD-CNN exploits the spatio-temporal correlations among neighboring time frames and multiple coils to enable higher acceleration rates.

ACKNOWLEDGMENT

The authors thank Jennifer Rodriguez and Amanda Paskavitz for editorial corrections. Open access funding enabled and organized by Projekt DEAL.

CONFLICT OF INTEREST

Xiaoying Cai is a Siemens Employee.

DATA AVAILABILITY STATEMENT

The code and data that support the findings of this study are openly available in Harvard dataverse at (<https://dataverse.harvard.edu/dataverse/cardiacmr>), reference number (<https://doi.org/10.7910/DVN/E9FFZK>).

ORCID

Hossam El-Rewaidy  <https://orcid.org/0000-0002-5266-8702>

REFERENCES

1. American College of Cardiology Foundation Task Force on Expert Consensus Documents; Hundley WG, Bluemke DA, et al. ACCF/ACR/AHA/NASCI/SCMR 2010 expert consensus document on cardiovascular magnetic resonance: A report of the American college of cardiology foundation task force on expert consensus documents. *Circulation*. 2010;121:2462-2508.
2. Rehwald WG, Kim RJ, Simonetti OP, Laub G, Judd RM. Theory of high-speed MR imaging of the human heart with the selective line acquisition mode. *Radiology*. 2001;220:540-547.
3. Song HK, Dougherty L. k-Space weighted image contrast (KWIC) for contrast manipulation in projection reconstruction MRI. *Magn Reson Med*. 2000;44:825-832.
4. McGibney G, Smith MR, Nichols ST, Crawley A. Quantitative evaluation of several partial Fourier reconstruction algorithms used in MRI. *Magn Reson Med*. 1993;30:51-59.
5. Kellman P, Chefd'hotel C, Lorenz CH, Mancini C, Arai AE, McVeigh ER. Fully automatic, retrospective enhancement of real-time acquired cardiac cine MR images using image-based navigators and respiratory motion-corrected averaging. *Magn Reson Med*. 2008;59:771-778.
6. Kellman P, Chefd'hotel C, Lorenz CH, Mancini C, Arai AE, McVeigh ER. High spatial and temporal resolution cardiac cine MRI from retrospective reconstruction of data acquired in real time using motion correction and resampling. *Magn Reson Med*. 2009;62:1557-1564.
7. Feng L, Srichai MB, Lim RP, et al. Highly accelerated real-time cardiac cine MRI using k-t SPARSE-SENSE. *Magn Reson Med*. 2013;70:64-74.
8. Haji-Valizadeh H, Rahsepar AA, Collins JD, et al. Validation of highly accelerated real-time cardiac cine MRI with radial k-space sampling and compressed sensing in patients at 1.5T and 3T. *Magn Reson Med*. 2017;79:2745-2751. <https://doi.org/10.1002/mrm.26918>.
9. Kido T, Kido T, Nakamura M, et al. Compressed sensing real-time cine cardiovascular magnetic resonance: Accurate assessment of left ventricular function in a single-breath-hold. *J Cardiovasc Magn Reson*. 2016;18:50.
10. Voit D, Zhang S, Unterberg-Buchwald C, Sohns JM, Lotz J, Frahm J. Real-time cardiovascular magnetic resonance at 1.5 T using balanced SSFP and 40 ms resolution. *J Cardiovasc Magn Reson*. 2013;15:79.
11. Feng L, Grimm R, Block KT, et al. Golden-angle radial sparse parallel MRI: Combination of compressed sensing, parallel imaging, and golden-angle radial sampling for fast and flexible dynamic volumetric MRI. *Magn Reson Med*. 2014;72:707-717.
12. Feng L, Axel L, Chandarana H, Block KT, Sodickson DK, Otazo R. XD-GRASP: Golden-angle radial MRI with reconstruction of extra motion-state dimensions using compressed sensing. *Magn Reson Med*. 2016;75:775-788.
13. Schlemper J, Caballero J, Hajnal JV, Price AN, Rueckert D. A deep cascade of convolutional neural networks for dynamic MR image reconstruction. *IEEE Trans Med Imaging*. 2018;37:491-503.
14. Qin C, Schlemper J, Caballero J, Price AN, Hajnal JV, Rueckert D. Convolutional recurrent neural networks for dynamic MR image reconstruction. *IEEE Trans Med Imaging*. 2019;38:280-290.

15. Wang S, Ke Z, Cheng H, et al. DIMENSION: Dynamic MR imaging with both k-space and spatial prior knowledge obtained via multi-supervised network training. *NMR Biomed*. 2019:e4131. <https://doi.org/10.1002/nbm.4131>.
16. Hauptmann A, Arridge S, Lucka F, Muthurangu V, Steeden JA. Real-time cardiovascular MR with spatio-temporal artifact suppression using deep learning—proof of concept in congenital heart disease. *Magn Reson Med*. 2019;81:1143-1156.
17. Hammernik K, Klatzer T, Kobler E, et al. Learning a variational network for reconstruction of accelerated MRI data. *Magn Reson Med*. 2018;79:3055-3071.
18. Akçakaya M, Moeller S, Weingärtner S, Uğurbil K. Scan-specific robust artificial-neural-networks for k-space interpolation (RAKI) reconstruction: Database-free deep learning for fast imaging. *Magn Reson Med*. 2019;81:439-453.
19. Kofler A, Dewey M, Schaeffter T, Wald C, Kolbitsch C. Spatio-temporal deep learning-based undersampling artefact reduction for 2D radial cine MRI with limited training data. *IEEE Trans Med Imaging*. 2020;39:703-717.
20. El-Rewaidy H, Neisius U, Mancio J, et al. Deep complex convolutional network for fast reconstruction of 3D late gadolinium enhancement cardiac MRI. *NMR Biomed*. 2020:e4312.
21. Fessler JA, Sutton BP. Nonuniform fast Fourier transforms using min-max interpolation. *IEEE Trans Signal Process*. 2003;51:560-574.
22. Feng L, Grimm R, Block KT, et al. Golden-angle radial sparse parallel MRI: Combination of compressed sensing, parallel imaging, and golden-angle radial sampling for fast and flexible dynamic volumetric MRI. *Magn Reson Med*. 2014;72:707-717.
23. Rosenzweig S, Holme HCM, Uecker M. Simple auto-calibrated gradient delay estimation from few spokes using Radial Intersections (RING). *Magn Reson Med*. 2019;81:1898-1906.
24. Tamir J, Ong F, Cheng J, Uecker M, Lustig M. Generalized magnetic resonance image reconstruction using the Berkeley advanced reconstruction toolbox. In: Proceedings of ISMRM Workshop on Data Sampling and Image Reconstruction, Sedona, AZ; 2016. p. 33.
25. Uecker M, Lai P, Murphy MJ, et al. ESPIRiT—An eigenvalue approach to autocalibrating parallel MRI: Where SENSE meets GRAPPA. *Magn Reson Med*. 2014;71:990-1001.
26. Paszke A, Gross S, Chintala S, et al. Automatic differentiation in PyTorch. In: *Neural Information Processing Systems Workshop*. California, USA; 2017.
27. Feng L, Chandarana H, Xu J, Block KT, Sodickson D, Otazo R. K-t radial SPARSE-SENSE: Combination of compressed sensing and parallel imaging with golden angle radial sampling for highly accelerated volumetric dynamic MRI. In: *International Society for Magnetic Resonance in Medicine*. Melbourne, Australia; 2012. p. 81.
28. Miao X, Lingala SG, Guo Y, et al. Accelerated cardiac cine MRI using locally low rank and finite difference constraints. *Magn Reson Imaging*. 2016;34:707-714.
29. Rasche V, De Boer RW, Holz D, Proksa R. Continuous radial data acquisition for dynamic MRI. *Magn Reson Med*. 1995;34:754-761.
30. Zhang S, Block KT, Frahm J. Magnetic resonance imaging in real time: Advances using radial FLASH. *J Magn Reson Imaging*. 2010;31:101-109.

SUPPORTING INFORMATION

Additional supporting information may be found online in the Supporting Information section.

VIDEO S1 MD-CNN sample reconstruction of all time frames at three different neighboring window sizes ($N_{fw} = 5, 7, \text{ and } 9$ frames) from the left side to the right side, respectively. The flickering artifacts are suppressed at larger window sizes (eg, 7 (middle) and 9 (right)) while the temporal fidelity did not degrade at these large window sizes when compared to a window size of 5

VIDEO S2 K-t radial sparse-sense (kt-RASPS) sample reconstruction of all time frames at three different values of regularization weights ($\lambda = 0.01, 0.025, \text{ and } 0.1$) from the left side to the right side, respectively. The reconstructed data with low regularization values ($\lambda = 0.01$) showed a high level of streaking artifacts, and increased temporal blurring at higher regularization levels ($\lambda = 0.1$), while data at $\lambda = 0.025$ showed minimal streaking artifacts with relatively high temporal fidelity

VIDEO S3 K-t radial sparse-sense (kt-RASPS) sample reconstruction of all time frames at 3 different values of regularization weights (#iterations = 25, 50, and 100) from the left side to the right side, respectively. The image quality increases at #iterations = 50 compared to that at #iterations = 25, while image quality was maintained at #iterations = 50 and 100

VIDEO S4 Representative reconstruction at 14 spokes/frame of undersampled data from one subject at all cardiac phases by different reconstruction methods: the locally low rank and temporal finite differences compressed sensing method (LLR+FD), k-t radial sparse-sense (kt-RASPS), 3D U-net, the proposed MD-CNN network, and reference data, from left to right, respectively

VIDEO S5 Representative reconstruction at 14 spokes/frame of undersampled data from another subject at all cardiac phases by different reconstruction methods: the locally low rank and temporal finite differences compressed sensing method (LLR+FD), k-t radial sparse-sense (kt-RASPS), 3D U-net, the proposed MD-CNN network, and reference data, from left to right, respectively

VIDEO S6 Representative reconstruction at 14, 16, and 20 spokes/frame of undersampled data from one subject at all cardiac phases by the proposed MD-CNN network. Temporal fidelity increases as number of spokes increase

FIGURE S1 Mean squared error (MSE) for MD-CNN images in the training and testing datasets at each of the 250 training epochs

FIGURE S2 Sample reconstructed images at end-systole by the three methods (kt-RASPS, MD-CNN, and Reference) showing the six segments at which LV sharpness was quantified and the intensity profiles corresponding to each segment of the sample images

FIGURE S3 Bland-Altman plots showing inter-observer agreement of each comparison: Reader#1 vs. Reader#2, Reader#2 vs. Reader#3, and Reader#1 vs. Reader#3 of the extracted LV myocardial areas in kt-RASPS, MD-CNN, and reference images, separately

TABLE S1 Clinical indications for clinical cardiac MR scans of our patient cohort

TABLE S2 Biases and limits of agreement of the Bland-Altman plots for inter-observer agreement of 3 comparisons: Reader#1 vs. Reader#2, Reader#2 vs. Reader#3, and Reader#1 vs. Reader#3 of the extracted LV myocardial areas in kt-RASPS, MD-CNN, and reference images

How to cite this article: El-Rewaigy H, Fahmy AS, Pashakhanloo F, et al. Multi-domain convolutional neural network (MD-CNN) for radial reconstruction of dynamic cardiac MRI. *Magn Reson Med*. 2021;85:1195–1208. <https://doi.org/10.1002/mrm.28485>

4.4. SUPPORTING INFORMATION

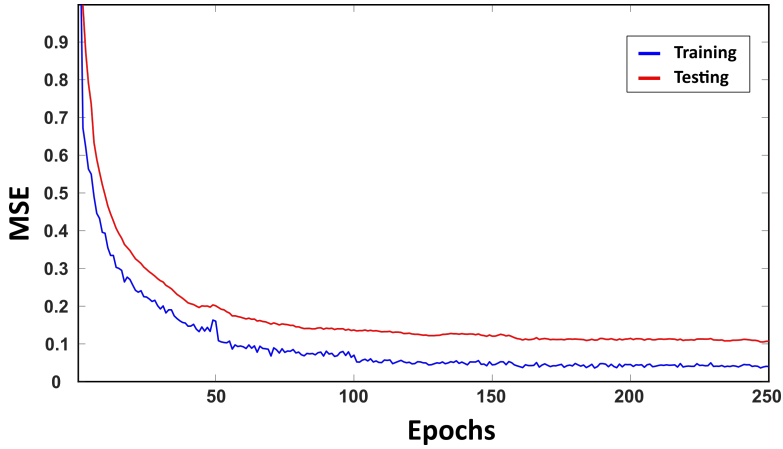


Figure 4.8: (Figure S1) Mean squared error (MSE) for MD-CNN images in the training and testing datasets at each of the 250 training epochs.

Table 4.4: (Table S2) Biases and limits of agreement of the Bland-Altman plots for inter-observer agreement of 3 comparisons: Reader#1 vs. Reader#2, Reader#2 vs. Reader#3, and Reader#1 vs. Reader#3 of the extracted LV myocardial areas in kt-RASPS, MD-CNN, and reference images.

Comparison	Bias			Upper Limit			Lower Limit		
	kt-RASPS	MD-CNN	Reference	kt-RASPS	MD-CNN	Reference	kt-RASPS	MD-CNN	Reference
R1 vs. R2	-0.37	-0.27	-0.26	10.2	6.2	6.4	-10.9	-6.7	-6.9
R1 vs. R3	2*	1.1	0.7	9.7	7	6.2	-5.7	-4.9	-4.8
R2 vs. R3	1.6*	0.8	0.4	8.3	4.6	4.9	-5	-3	-4.1

¹ *p-value <0.05 LV myocardial area between Readers

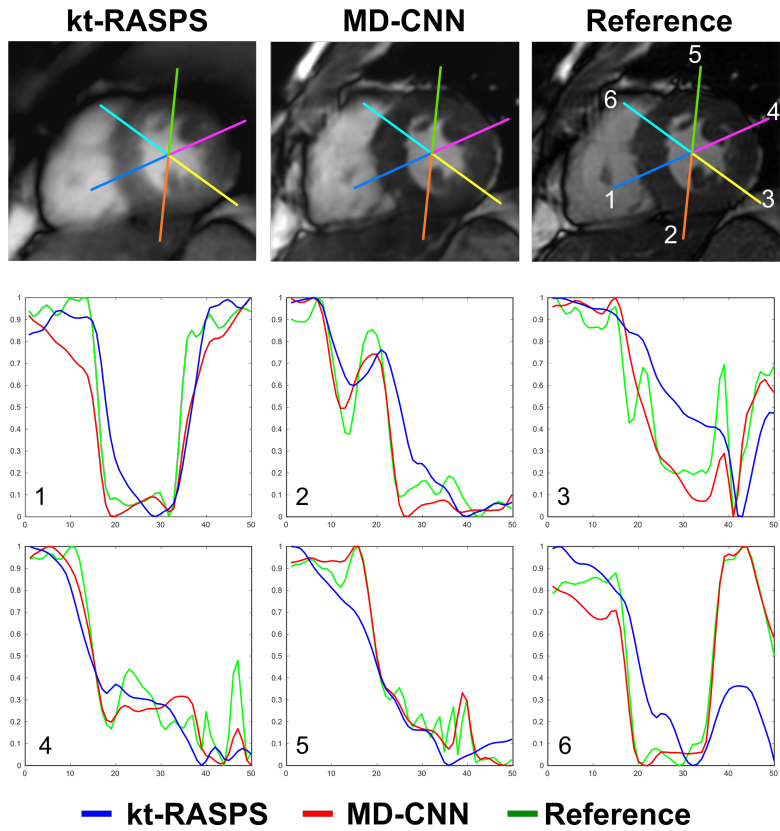


Figure 4.9: (Figure S2) Sample reconstructed images at end-systole by the three methods (kt-RASPS, MD-CNN, and Reference) showing the six segments at which LV sharpness was quantified and the intensity profiles corresponding to each segment of the sample images.

5

NEURAL NETWORKS FOR ACCELERATING MYOCARDIAL T_1 MAPPING

In this chapter, we develop and evaluate MyoMapNet, a rapid myocardial T_1 mapping approach that uses neural networks (NN) to estimate voxel-wise myocardial T_1 and extracellular (ECV) from T_1 -weighted images collected after a single inversion pulse over 4-5 heartbeats. MyoMapNet utilizes a simple fully-connected NN to estimate T_1 values from 5 (native) or 4 (post-contrast) T_1 -weighted images. MyoMapNet T_1 mapping enables myocardial T_1 quantification in 4-5 heartbeats with near-instantaneous map estimation time with similar accuracy and precision as MOLLI.

5.1. INTRODUCTION

CARDIOVASCULAR magnetic resonance (CMR) myocardial T_1 and extracellular volume (ECV) mapping allow for non-invasive quantification of interstitial diffuse fibrosis [2]. Over the past decade, there have been significant advances in CMR pulse sequences for myocardial T_1 mapping [109–111, 116–121]. These sequences are based on the application of magnetization preparation pulses (such as inversion [109, 111, 119], saturation [110, 116], or a combination of both [121]) for the collection of a series of T_1 weighted images. Subsequently, tissue relaxation times are estimated using a two or three-parameter fitting model [109–111, 116–122]. For each of these sequences, there are different trade-offs in accuracy, precision, coverage (2D vs. 3D), and respiratory motion (free breathing vs breath-holding) [120, 123–133]. Alternatively, recent approaches, such as combined T_1 and T_2 mapping [125, 129, 134–136], MR fingerprinting [137, 138], or multitasking [139], have been introduced to simultaneously measure different tissue parameters.

Among different myocardial T_1 mapping sequences, Modified Look-Locker (LL) inversion recovery (MOLLI) [119], acquired within a single breath-hold, is the most widely used sequence for myocardial T_1 mapping. This sequence consists of three sets of LL experiments with 3 heartbeats (or 3 seconds) in between for magnetization recovery. This acquisition is commonly referred to as the 3(3)3(3)5 MOLLI scheme, which indicates that 3, 3, and 5 images are acquired in three LL experiments with 3 rest heartbeats (i.e., 3RR interval) between each LL experiment. MOLLI-5(3)3 and MOLLI-4(1)3(1)2 were implemented to improve acquisition efficiency and precision [124]. A variation of these sequences in which the rest period between acquisition utilizes a fixed time (1-3 second) instead of heartbeats was also implemented [140]. These modifications reduce the duration of the original MOLLI from approximately 17 heartbeats to 11 heartbeats [124]. In this approach, T_1 -weighted images are acquired at multiple points throughout the recovery curve, and a pixel-wise curve fitting algorithm using a 3-parameter model is applied to estimate the T_1 values at each pixel. Recently, the inversion group (IG) fitting has also been proposed for MOLLI with shorter waiting periods between LL experiments, albeit with a penalty on precision [141–143]. For shortened MOLLI (ShMOLLI) with a 5(1)1(1)1 scheme [109], a conditional fitting algorithm is utilized to discard the latter measurements for long T_1 at high heart-rates.

Alternatives to standard curve-fitting techniques in parametric mapping include dictionary based reconstruction, simulated signal recovery, or machine learning [144–146]. Shao et al. used a deep learning model for rapid and accurate calculation of myocardial T_1 and T_2 in Bloch equation simulation with slice profile correction [146]. Similarly, Hamilton et. al. used deep learning to rapidly reconstruct T_1 and T_2 maps from

CMR fingerprinting images [144]. To reduce motion artifacts and minimize the acquisition window in T_1 mapping during the cardiac cycle, a convolutional neural network (CNN) model was used to reconstruct highly accelerated T_1 weighted images in slice-interleaved T_1 mapping sequences with radial sampling (38). Deep learning neural networks were also recently used to combine saturation recovery and inversion data to improve T_1 mapping precision [147]. These studies have demonstrated the potential for machine learning to improve myocardial tissue characterization by increasing precision and reconstruction speed, or decreasing motion sensitivity or other confounders of T_1 mapping.

In this study, we sought to develop and evaluate a fully connected neural network (MyoMapNet)-based rapid myocardial T_1 mapping approach using a single LL experiment with a scan duration of 4-5 heartbeats and near-instantaneous (2ms) reconstruction time. The proposed MyoMapNet was trained and validated using numerically simulated data and in-vivo images; MyoMapNet's performance was compared to MOLLI with a 3-parameter fitting model.

5.2. METHODS

5.2.1. MYOMAPNET T_1 MAPPING

The data acquisition for MyoMapNet is very similar to MOLLI sequence and is based on the collection of 5 (native) or 4 (post-contrast) T_1 weighted images after a single inversion pulse. Figure 5.1 shows the pulse sequence and magnetization evolution of MOLLI-5(3)3 for native T_1 mapping, composed of two LL experiments to acquire eight T_1 weighted images over 11 heartbeats. In MyoMapNet, we use the five images sampled after the first inversion pulse for native MOLLI-5(3)3 T_1 measurement. For post-contrast T_1 mapping, we will use only the first four images collected using MOLLI-4(1)3(1)2 T_1 (Figure 5.2). In contrast to MOLLI, where a 3-parameter fit model is used to estimate native or post-contrast T_1 mapping, in MyoMapNet, we propose to use a neural network to estimate T_1 values from only 5 (native) or 4 (post-contrast) T_1 images, thereby reducing the scan time to only 5 heartbeats for native and 4 heartbeats for post-contrast scans.

5.2.2. NUMERICAL SIMULATION

MOLLI-5(3)3 simulations were performed to generate the training and testing signal-intensity time courses. A single-shot readout for two sequences was simulated using Bloch equation with the following parameters: balanced Steady-State Free Precession (bSSFP) acquisition with 5 ramp-up pulses, TR/flip angle = 2.5 ms/35°, 80 phase-encode lines, acquisition window = 200 ms, and linear phase ordering. The time between the inversion and the center of k-space was 120 ms and 200 ms for two LL experiments of

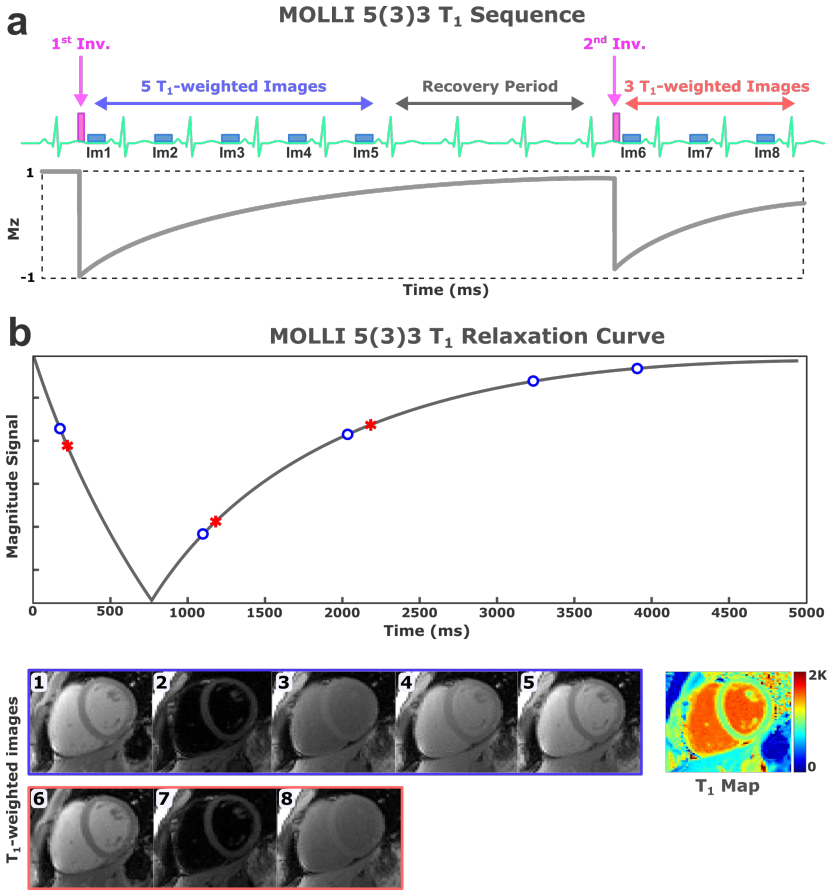


Figure 5.1: MOLLI-5(3)3 sequence (a) and associated signal recovery (b): two look-locker inversion pulses are performed to acquire eight T_1 -weighted images with a recovery period of 3 heartbeats between look-lockers. In MyoMapNet, images collected after the first inversion pulse are used for estimating the T_1 values.

MOLLI-5(3)3. Simulated T_1 ranged from 400 ms to 1800 ms with an increment of 0.1 ms, T_2 of 42 ms, and a fixed heart rate of 60 bpm. Subsequently, different Gaussian noise levels were added to the simulated signals for SNRs of 20, 40, and 100. This process was repeated 5 times for each SNR to generate a total of 80,000 signal time-courses, each with 8 time-points, to serve as data augmentation. A 3-parameter fitting model was used to calculate T_1 of each signal time course:

$$s(TI) = A - Be^{(-TI/T_1^*)} \quad (5.1)$$

where TI represents the inversion time, and A, B, and T_1^* were three unknowns. T_1 was determined from the resulting A, B, and T_1^* by applying the equation: $T_1 =$

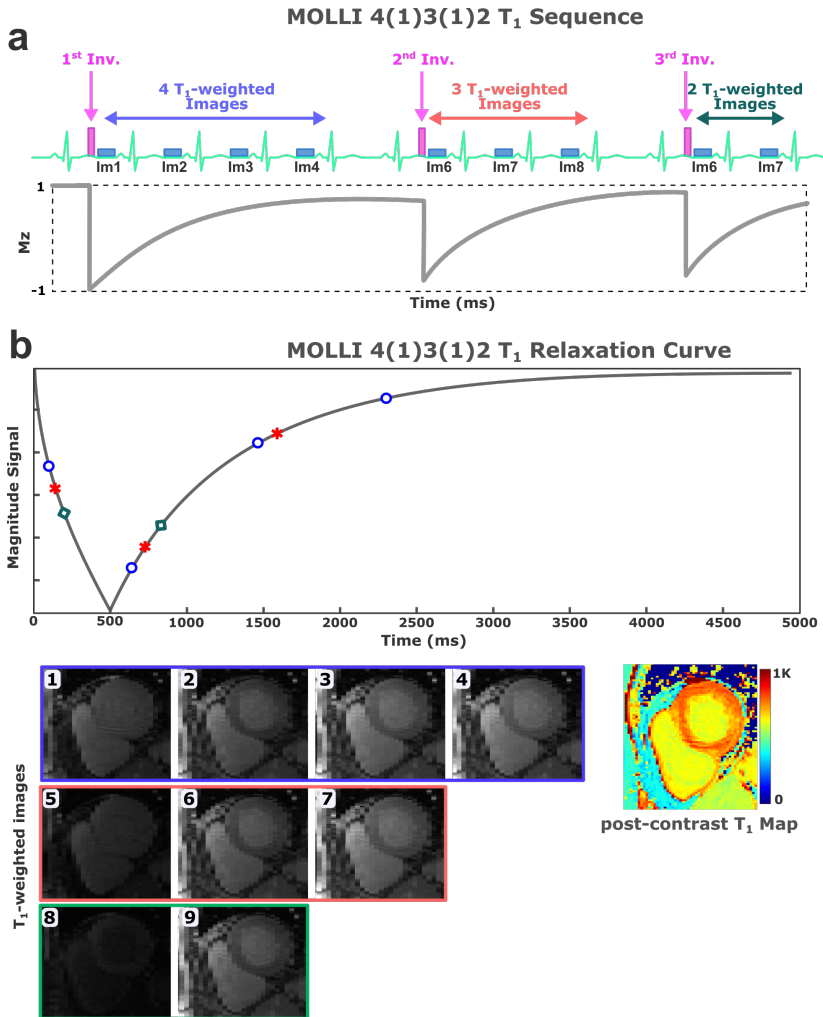


Figure 5.2: MOLLI-4(1)3(1)2 sequence (a) and associated signal recovery (b): three look-locker inversion pulses are performed to acquire nine T₁-weighted images with a recovery period of one heartbeat between look-lockers. In MyoMapNet, images collected after the first look-locker are used for estimating the T₁ values.

$$T_1^* (B/A - 1).$$

5.2.3. IN-VIVO DATA

The study protocol was approved by the Institutional Review Board and written consent was waived. T₁ mapping data was collected as part of the clinical exam in all participants, and we retrospectively extracted T₁ mapping data. Patient data were handled in compliance with the Health Insurance Portability and Accountability Act. Imaging was

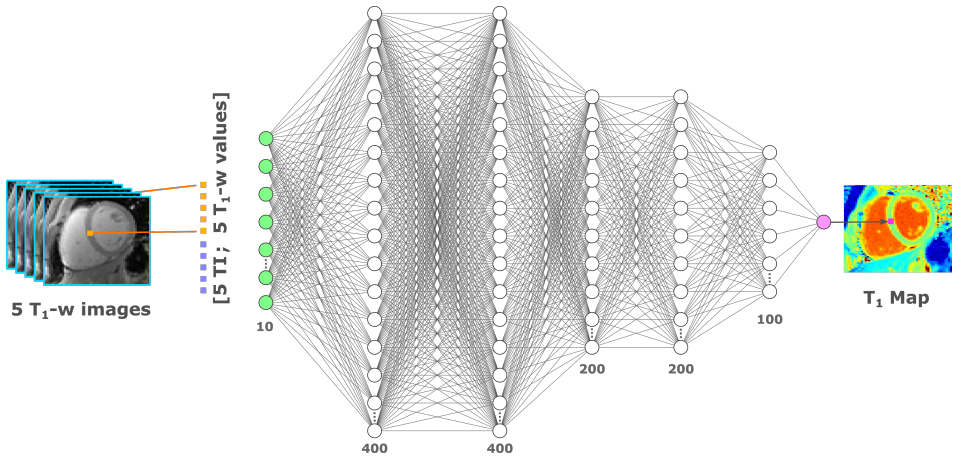


Figure 5.3: MyoMapNet architecture: MyoMapNet uses a fully-connected neural network for estimating pixel-wise T_1 values from T_1 -weighted images collected after a single look-locker inversion pulse (i.e. the first 5 images of MOLLI-5(3)3 or first 4 images of MOLLI-4(1)3(1)2). For each voxel, the signal values from 5 T_1 -weighted images are concatenated with their corresponding look-locker times and used as the network input (i.e. 10×1) for native T_1 mapping. The input values are fed to a fully-connected network with 5 hidden layers with 400, 400, 200, 200, and 100 nodes each layer, respectively. The output is the estimated T_1 value at each voxel.

5

performed using a 3T scanner (MAGNETOM Vida, Siemens Healthineers, Erlangen, Germany) equipped with body and spine phased-array coils.

T_1 mapping using MOLLI was collected in 717 subjects (386 males, 55 ± 16.5 years) with a subset of 535 subjects (232 males, 56.5 ± 15 years) having both native and post-contrast T_1 maps. All data were extracted retrospectively from patients who were referred for a clinical CMR exam for various cardiovascular indications from October 2018 to March 2020.

MOLLI-5(3)3 and MOLLI-4(1)3(1)2 were performed using the following parameters: bSSFP with 5 ramp-up excitations, FOV = 360×320 mm², voxel size = $1.7 \times 1.7 \times 8$ mm³, TR/TE = 2.5 ms/1.03 ms, flip angle = 35° , linear phase-encoding ordering, partial Fourier factor = $7/8$, GRAPPA acceleration factor of 2 with 24 reference lines, acquisition window 218 ms during diastole, slice gap 12 mm. Three slices in the short-axis view (SAX) were collected in three separate breath-holds with 10 second rest periods between breath-holds. Adiabatic tan/tanh inversion pulse was used. Both MOLLI-5(3)3 and MOLLI-4(1)3(1)2 used a minimum inversion time (TI) of 100 ms with a TI increment of 80 ms. For post-contrast measurement, MOLLI-4(1)3(1)2 data was collected 15-20 min after injection of Gd-DTPA at 0.1 mmol/kg (Gadavist, Bayer Pharma AG, Berlin, Germany). MOLLI-5(3)3 and MOLLI-4(1)3(1)2 T_1 were calculated using a 3-parameter curve fitting model (Equation 1).

5.2.4. T_1 ESTIMATION IN MYOMAPNET

MyoMapNet is a fully-connected neural network that estimates T_1 maps from input T_1 -weighted images. MyoMapNet input layer has $2N_t$ nodes for N_t T_1 weighted signals and their corresponding inversion times, where $N_t=5$ in the native T_1 network, and $N_t=4$ in the post-contrast T_1 network. MyoMapNet is consisted of M_l layers each of $(200 \times S)$ nodes followed by M_l layers of $(100 \times S)$ nodes each, and one layer of $(50 \times S)$ nodes; where M_l controls the depth (total number of layers) of MyoMapNet, and S is a scaling factor to control the number of trainable parameters in each layer. For example, Figure 5.3 shows the MyoMapNet architecture at $M_l=2$ and $S=2$, where five hidden layers of 400, 400, 200, 200, 100 nodes in each layer were utilized. A leaky rectified linear unit activation function was applied after each hidden layer. MyoMapNet parameters were empirically optimized to balance between accurate T_1 mapping estimation and avoiding the risk of overfitting. To determine the optimal network depth and size, MyoMapNet performance was validated at $M_l=1,2, and 3 and $S=1,2, and 3. The number of parameters at different depths and scales of MyoMapNet is reported in Table 5.1.$$

MyoMapNet was implemented in Python using the PyTorch library version 0.41. Training and validation were performed on an NVIDIA DGX-1 system equipped with 8T V100 graphics processing units (GPUs; each with 32 GB memory and 5120 cores), central processing unit (CPU) of 88 core: Intel Xeon 2.20 GHz each, and 504 GB RAM. Only 2 GPUs were considered for training and testing the proposed MyoMapNet.

Table 5.1: Number of parameters at different MyoMapNet depth (3, 5, and 7 layers) and network size ($S=1, 2,$ and 3).

	3 layers	5 layers	7 layers
S=1	27401	77701	128001
S=2	104801	305401	506001
S=3	232201	683101	1134001

5.2.5. MYOMAPNET TRAINING

For simulation experiments, a set of 64,000 simulated signals (80% of the whole dataset) was randomly selected at each noise level (i.e. SNR of 100, 40, and 20). Each of these datasets was used to train the MyoMapNet separately. For in-vivo studies, training datasets of 573 patients (1719 native T_1 maps) and 428 patients (1281 post-contrast T_1 maps) were randomly selected for the native and post-contrast map reconstructions, respectively. A detailed description of data splitting is included in Figure 5.4. Corrupted native T_1 maps

(249 maps) due to image artifacts were excluded from the training dataset. MOLLI-5(3)3 and MOLLI-4(1)3(1)2 T₁ maps were estimated using 8 (native) or 9 (post-contrast) T₁-weighted images. We performed all the map reconstruction offline without motion correction. Two loss functions were studied to minimize the error between the estimated and reference MOLLI T₁ values:

The mean-absolute error loss function (MAE) = $\frac{1}{n} \sum_{i=1}^n |estimated_T_{1_i} - MOLLI_T_{1_i}|$

The mean-squared error loss (MSE) = $\frac{1}{n} \sum_{i=1}^n (estimated_T_{1_i} - MOLLI_T_{1_i})^2$

where n is the number of T₁ samples in a minibatch of the training dataset (batch size =80 T₁ maps). To select the optimal loss function and network size, the training dataset was further split into subsets of 80% training and 20% validation of the network for the optimization experiments only. The stochastic gradient descent optimizer with an initial learning rate of 1E-8 and momentum of 0.8 was used to train the network for 2000 epochs with a batch size of 80 maps. The same hyperparameters were used to train all models on native and post-contrast datasets, except for networks with S=3 or M_l=3, where a batch size of 60 T₁ maps was used. MyoMapNet took 8.3±2.5 hours to be trained using the native T₁ dataset.

5

5.2.6. MYOMAPNET EVALUATION

The performance of MyoMapNet was evaluated using the independent testing dataset. The simulated testing dataset contained 16,000 samples, containing T₁ ranging from 400 to 1800ms. For in-vivo studies, we used native T₁ maps from 144 patients (432 MOLLI-5(3)3 T₁ maps) and post-contrast T₁ maps from 107 patients (324 MOLLI-4(1)3(1)2 T₁ maps). For each T₁ map, we calculated 3 sets of T₁ estimates: (a) standard MOLLI T₁ mapping using 3-parameter curve fitting from all collected images (8, or 9 images in native or post-contrast T₁ mapping, respectively), (b) abbreviated MOLLI using only 5 native (MOLLI-5) or 4 post-contrast MOLLI (MOLLI-4) images using standard 3-parameter curve fitting, and (c) MyoMapNet using only 5 native or 4 post-contrast T₁ weighted images, retrospectively extracted from the standard MOLLI dataset. The ECV values were calculated for patients who had both native and post-contrast T₁ mapping available in the testing dataset (75 patients).

5.2.7. DATA ANALYSIS

Endocardial and epicardial contours were drawn to measure global T₁ values. Figure 5.5 shows example contours for 4 different subjects. The mean and standard deviation of T₁ or ECV from the LV myocardium were calculated. The global T₁ was measured by averaging the myocardial T₁ from three different slices. Native, post-contrast T₁, and

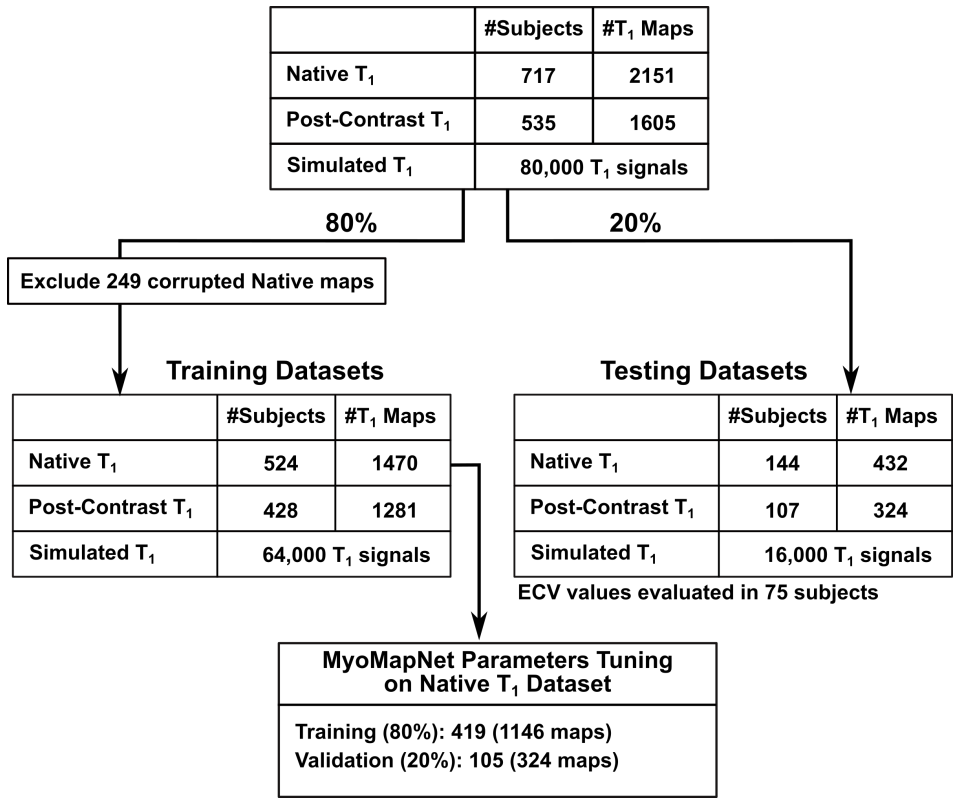


Figure 5.4: Flowchart for MyoMapNet training, testing, and parameter-tuning validation splits in the native, post-contrast, and simulated T₁ datasets. ECV values were evaluated in 75 subjects who had both native and post-contrast T₁ data available in the testing dataset.

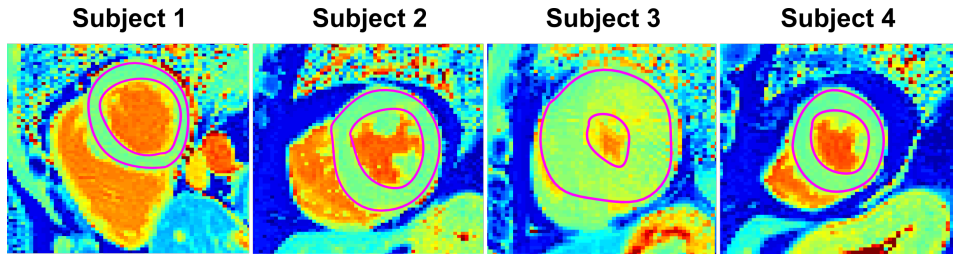


Figure 5.5: Example native T₁ maps with left ventricular myocardial segmentation used for analyzing T₁ estimations by MyoMapNet, MOLLI-5, and standard MOLLI-5(3)3.

ECV values were reported as mean \pm standard deviation. The 95% confidence interval (95% CI) of the mean was reported to represent a range of values that contains the true mean of the population with 95% certainty. The precision of T₁ maps was assessed using the standard deviation of T₁ values within the myocardium. Bland-Altman analysis was

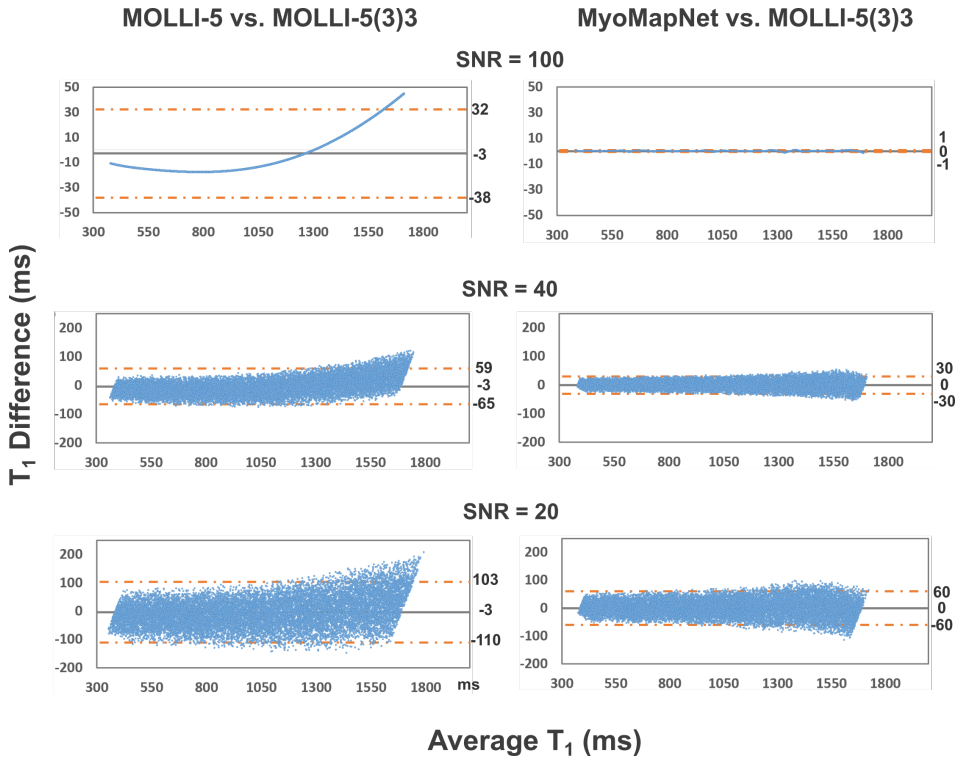


Figure 5.6: Bland-Altman plots showing the mean difference and 95% limits of agreement between the simulated T_1 values by the MOLLI-5 vs. MOLLI-5(3)3 (left column) and MyoMapNet vs. MOLLI-5(3)3 (right column) for SNR of 100, 40, and 20. MOLLI-5 yields a systematic error in T_1 estimations, which is corrected in MyoMapNet.

used to characterize per slice and per patient T_1 estimated by two different methods (abbreviated MOLLI vs. standard MOLLI, and MyoMapNet vs. standard MOLLI) and reported as the mean difference of T_1 estimations and 95% limits of agreements.

Group differences in per-slice T_1 measurements were assessed using linear mixed-effects models with compound symmetry covariance structure [148]. In these models, the pair-wise group difference was fitted as the outcome, and the subject was included as a random intercept. The average and standard deviation of T_1 were compared between two methods using the paired Student's t-test. Bonferroni correction was utilized to account for three pair-wise group comparisons. All tests were two-sided and the nominal level of statistical significance was 0.0167.

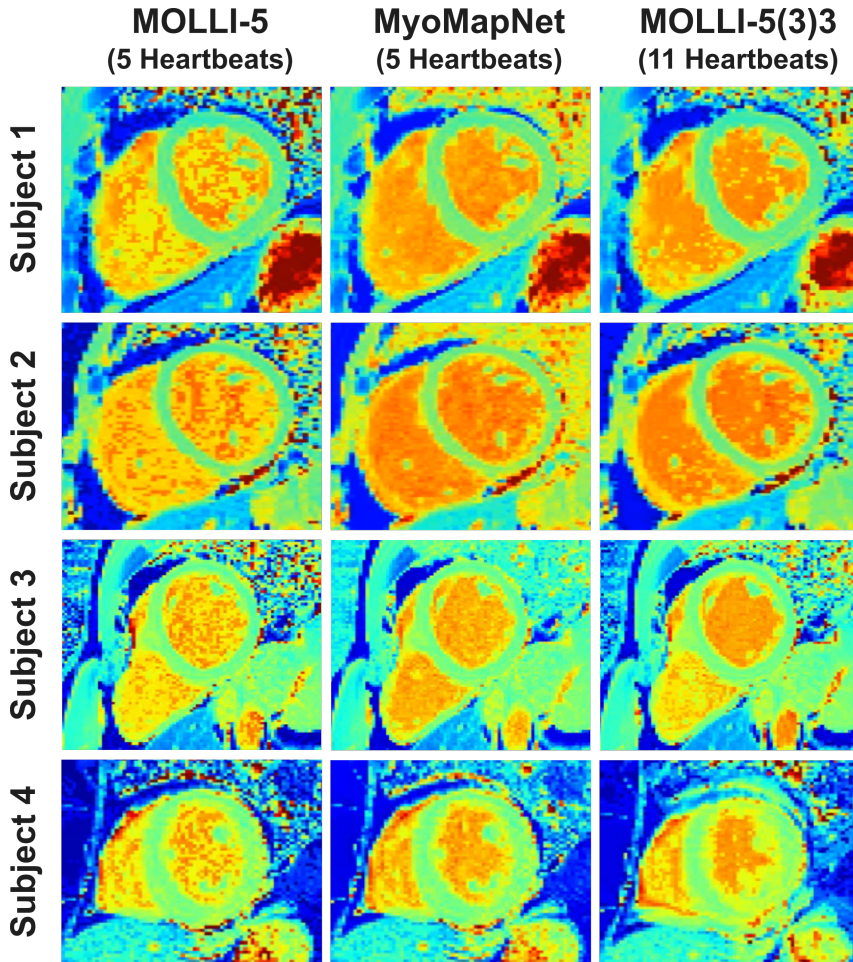


Figure 5.7: Native T_1 maps from four patients, reconstructed using MOLLI-5 (using only 5 T_1 weighted images with 3-parameter fitting), MyoMapNet, and MOLLI-5(3)3 with a 3-parameter fitting model. MyoMapNet yield maps with more homogenous signal compared to MOLLI-5.

5.3. RESULTS

5.3.1. NETWORK OPTIMIZATION

The native T_1 estimation errors between MyoMapNet and standard MOLLI-5(3)3 in the validation dataset at different loss functions, number of layers, and number of nodes per layer (18 networks in total) are summarized in Table 5.2. In general, MAE loss showed consistently lower errors than MSE at different network sizes and was therefore used to train all MyoMapNet models. For MAE, small changes in T_1 estimation errors were reported between MyoMapNet and MOLLI-5(3)3 at different network sizes with slightly

lower STD for bigger networks. MyoMapNet of 5 hidden layers ($M_l = 2$) and 400, 400, 200, 200, and 100 nodes ($S=2$) at each layer with a total of 305,401 trainable parameters, was therefore used for all T_1 estimation models to balance between small estimation errors and lower chances of overfitting due to increased number of parameters.

Table 5.2: Mean difference (\pm STD) in T_1 values between MyoMapNet and MOLLI-5(3)3 at different loss functions (MSE, and MAE), network depth (3, 5, and 7 layers) and network size ($S=1, 2$, and 3).

	MSE Loss			MAE Loss		
	3 layers	5 layers	7 layers	3 layers	5 layers	7 layers
S=1	0 \pm 25	12 \pm 30	9 \pm 24	3 \pm 27	5 \pm 24	5 \pm 24
S=2	12 \pm 23	5 \pm 24	5 \pm 22	6 \pm 24	3 \pm 24	4 \pm 22
S=3	11 \pm 23	18 \pm 21	-2 \pm 24	3 \pm 24	3 \pm 23	3 \pm 22

5.3.2. NUMERICAL SIMULATIONS

Figure 5.6 shows the differences in estimated T_1 between the MOLLI-5 (left) and MyoMapNet (right) vs MOLLI-5(3)3, simulated at SNR levels of 100, 40, and 20. For higher SNR, the estimated T_1 values using MOLLI-5 exhibit a systematic error as a function of T_1 values. For the same SNR, MyoMapNet shows no systematic error for different T_1 values. As SNR decreases, there is an increase in the error of estimated T_1 values using both techniques, but with lower error in MyoMapNet (0 \pm 15 ms, 95% CI [-0.3, 0.1]) compared to MOLLI-5 (-3 \pm 32 ms, and 95% CI [-4, -3]; $P < 0.001$) relative to MOLLI-5(3)3 at SNR=40. At SNR=20, the mean difference between MyoMapNet and MOLLI-5(3)3 was (0 \pm 31ms, 95% CI [-1, 1]) compared to MOLLI-5 (-3 \pm 54 ms, 95% CI [-4, -3]; $P < 0.001$).

5.3.3. IN-VIVO STUDIES

Figure 5.7 shows example native T_1 maps reconstructed with the MOLLI-5(3)3, MOLLI-5, and MyoMapNet in four subjects. The T_1 maps using MyoMapNet showed sharp myocardial T_1 boundaries with more homogeneous T_1 estimations similar to that of MOLLI-5(3)3 maps when compared to the MOLLI-5 method. This inhomogeneity in MOLLI-5 T_1 estimations is more apparent in the blood pool, affecting the accuracy and precisions of the estimated T_1 values.

The mean T_1 values and precision for myocardial native and post-contrast T_1 , and ECV maps are summarized in Table 5.3. MyoMapNet yields T_1 and ECV values similar to those of the standard MOLLI methods with lower estimation errors compared to abbreviated MOLLI methods (1230 \pm 63, 1200 \pm 45, and 1199 \pm 46 ms for native T_1 values; 548 \pm 63,

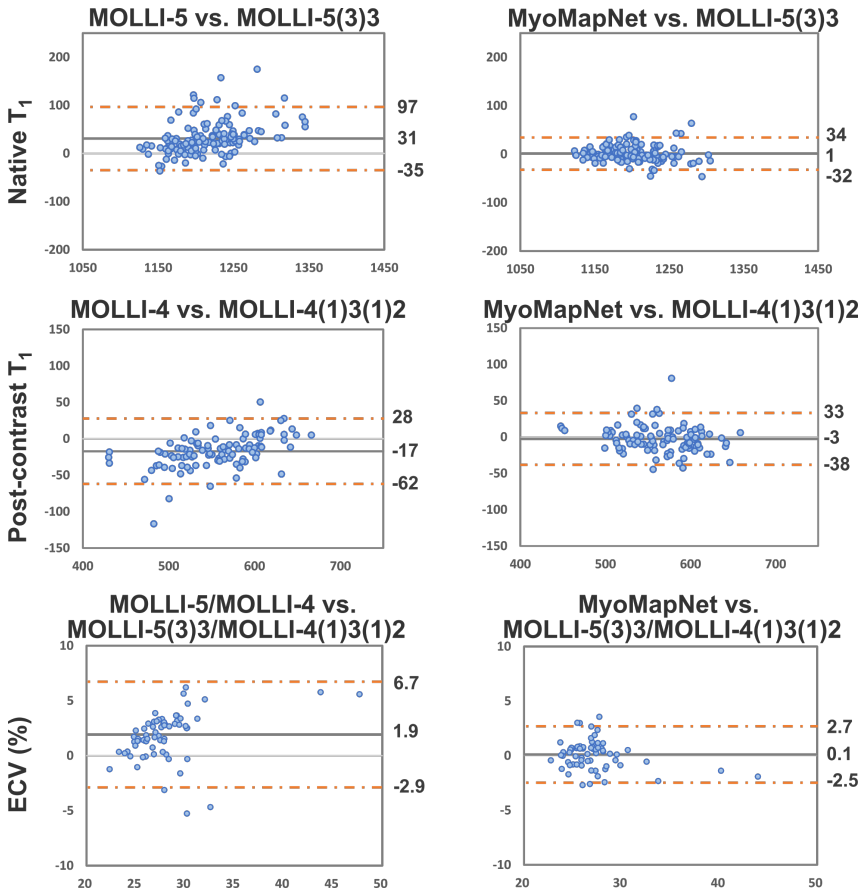


Figure 5.8: Bland-Altman plots showing the mean difference and 95% limits of agreement for global native, post-contrast T_1 , and ECV for the abbreviated MOLLI-5/MOLLI-4 vs. standard MOLLI-5(3)3/MOLLI-4(1)3(1)2 (left column) and MyoMapNet vs. standard MOLLI-5(3)3/MOLLI-4(1)3(1)2 (right column). Each dot represents the values calculated from one patient.

563±45, and 565±47 ms for post-contrast T_1 , and 29.3±5.6, 27.3±3.5, and 27.1±4% for ECV values using abbreviated MOLLI, MyoMapNet, and standard MOLLI methods, respectively). For native T_1 precision, the average precision of MyoMapNet T_1 estimations (120 ms, 95% CI [117, 122]) was superior to MOLLI-5 (148 ms, 95% CI [144, 151]; $P < 0.01$) and inferior to standard MOLLI-5(3)3 (112 ms, 95% CI [109, 114]; $P < 0.01$). In post-contrast T_1 , the average precision of MyoMapNet T_1 estimations (44 ms, 95% CI [42, 45]) was similar to the standard MOLLI-4(1)3(1)2 (43 ms, 95% CI [41, 44]; $P = 0.05$) and significantly higher than MOLLI-4 (52 ms, 95% CI [50, 54]; $P < 0.01$).

Bland-Altman plots for T_1 , post-contrast T_1 , and ECV for three different approaches (Figure 5.8) show similar measurements for MyoMapNet when compared to MOLLI,

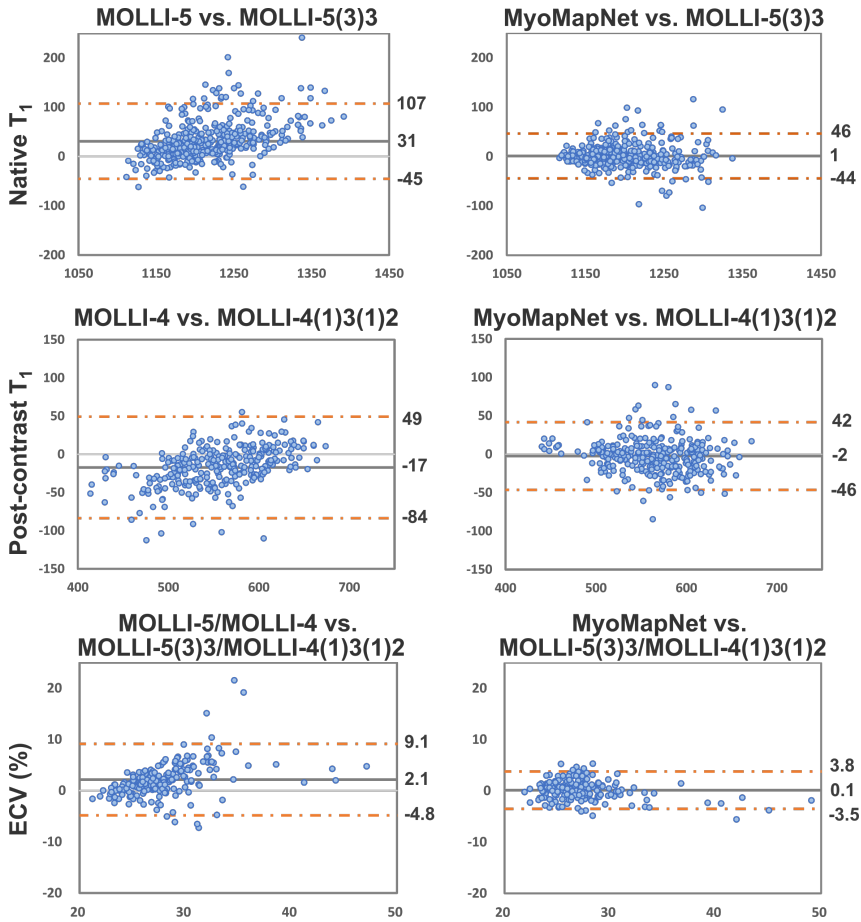


Figure 5.9: Bland-Altman plots showing per slice analysis of the mean difference and 95% limits of agreement for native, post-contrast T_1 , and ECV for the abbreviated MOLLI-5/MOLLI-4 vs. standard MOLLI-5(3)3/MOLLI-4(1)3(1)2 (left column) and MyoMapNet vs. standard MOLLI-5(3)3/MOLLI-4(1)3(1)2 (right column). Each dot represents the values calculated from one slice.

with increased measurement error for abbreviated MOLLI. Similar results were observed for per slice analysis of the three methods (Figure 5.9).

5.3.4. T_1 MAP RECONSTRUCTION TIME

The duration for estimating T_1 maps was 24.2 ± 0.5 sec by a 3-parameter fitting model without motion correction using Matlab on CPU, and 2 ± 0.01 ms by MyoMapNet using Python on GPU.

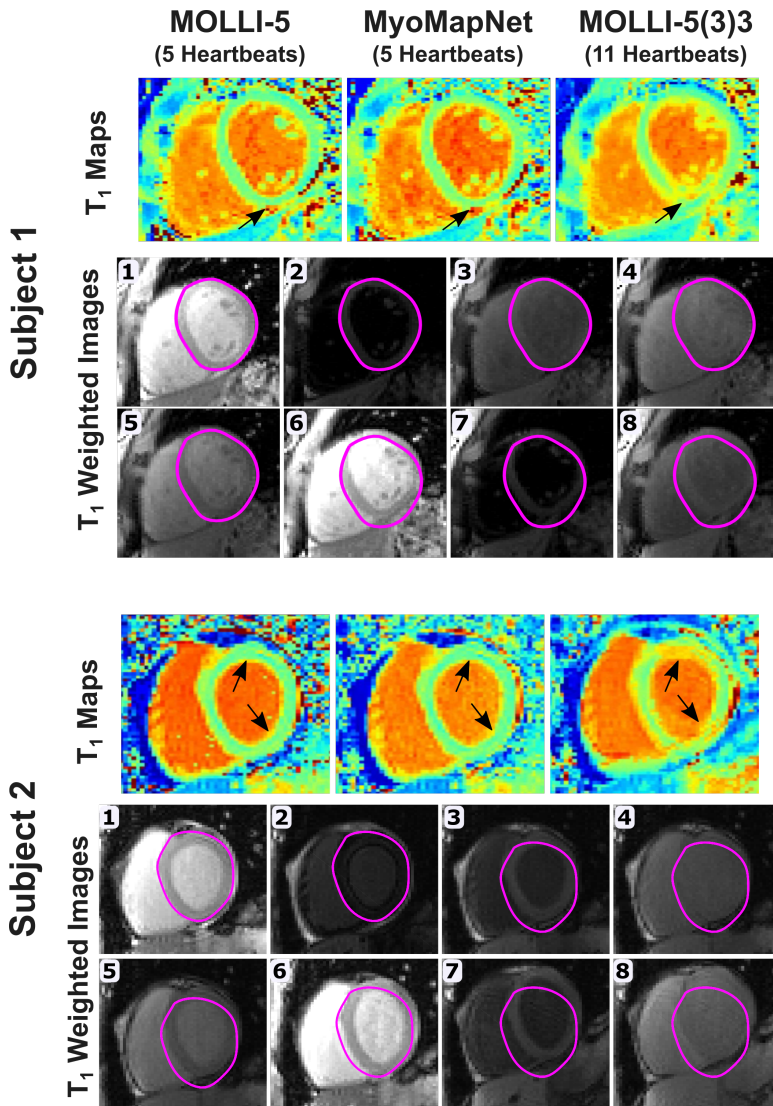


Figure 5.10: Myocardial T_1 maps calculated using MOLLI-5 with a 3-parameter fitting model, MyoMapNet, and MOLLI-5(3)3, demonstrating the impact of respiratory motion (black arrows) in two subjects. The epicardial delineation of image #1 was copied to all other T_1 -weighted images to show the degree of motion between images. Both subjects were instructed to hold their breath during the scan.

5.4. DISCUSSION

In this study, we evaluated the potential of a fully connected neural network for native and post-contrast myocardial T_1 and ECV mapping from 4-5 T_1 weighted images, reducing the scan time of myocardial T_1 mapping by 50% without compromising accuracy or

precision.

Respiratory motion in myocardial tissue mapping causes artifacts that adversely impact the quantification of tissue relaxation times. To minimize respiratory motion artifacts, imaging during breath-holding or use of respiratory slice tracking have been used [111–113, 128, 149–152]. For MOLLI, images for each slice are collected in a single breath-hold. However, even with breath-holding, patients often have respiratory motion-induced drift, which creates artifacts in maps. Therefore, respiratory motion correction is still being recommended [2]. Similarly, for free-breathing tissue characterization, while slice tracking reduced through-plane motion, motion correction is necessary to align images [112, 113]. Furthermore, motion correction will improve the reproducibility and robustness of tissue mapping [113]. One of the advantages of MyoMapNet is reducing the sensitivity to respiratory motion. Figure 5.10 shows example images demonstrating the presence of motion in standard MOLLI data, despite breath-holding. In this study, we used retrospectively collected data and were not able to perform a head-to-head comparison of the impact of shorter scan time on the motion. Further studies are warranted to further investigate the potential advantages of MyoMapNet in reducing motion sensitivity.

Table 5.3: Mean difference (\pm STD) in T_1 values between MyoMapNet and MOLLI-5(3)3 at different loss functions (MSE, and MAE), network depth (3, 5, and 7 layers) and network size (S=1, 2, and 3).

	Myocardial T_1 and ECV			Precision		
	Abrv. MOLLI	MyoMapNet	Std. MOLLI	Abrv. MOLLI	MyoMapNet	Std. MOLLI
Native T_1 (ms)	1230 \pm 63* \S	1200 \pm 45	1199 \pm 46	148 \pm 34* \S	120 \pm 27*	112 \pm 27
Post-contrast T_1 (ms)	548 \pm 63* \S	563 \pm 45	565 \pm 47	52 \pm 11* \S	44 \pm 11	43 \pm 10
ECV (%)	29 \pm 6* \S	27 \pm 4	27 \pm 4	-	-	-

¹Abrv. MOLLI: MOLLI-5 for Native T_1 or MOLLI-4 for Post-contrast T_1 ; Std. MOLLI: MOLLI-5(3)3 for Native T_1 or MOLLI-4(1)3(1)2 for Post-contrast T_1 ; *p-value < 0.01 when compared to Std. MOLLI; \S p-value < 0.01 when compared to MyoMapNet.

The numerical simulations of native T_1 MOLLI with SNR=100 showed systematic errors as a function of the T_1 value increments associated with MOLLI-5 relative to the standard MOLLI-5(3)3 estimations. The MyoMapNet learns a correction function to minimize such systematic errors and create unbiased T_1 estimations at different ranges of T_1 values. As more noise was added to the T_1 -weighted signals, the MOLLI-5 exhibited higher T_1 estimation errors. MyoMapNet significantly reduces the errors associated

with noise, while correcting for systematic errors. Similar observations were seen in the in-vivo data for native and post-contrast T_1 mapping, where MyoMapNet showed significantly lower T_1 and ECV estimation errors compared to the abbreviated MOLLI methods.

Machine learning is rapidly improving the workflow of myocardial tissue characterization in CMR [153]. Recent studies have demonstrated the potential for deep learning in automating analysis workflow and quality control [154, 155]. These methods could automatically perform motion correction, segmentation, and parameter quantification, thereby reducing the burden and observer-related variability of manual analysis. The MyoMapNet could be easily integrated with an automated analysis and quality control method to simplify the workflow.

In this study, we reduced the number of T_1 -weighted images to 4-5 images for estimating T_1 values without rigorously studying the impact of the number of T_1 -weighted images. Further studies are warranted to investigate the optimal number of T_1 -weighted images for myocardial T_1 mapping. For MOLLI, after LL, samplings along the relaxation curve are separated by cardiac cycle. The choice of inversion time can potentially impact the accuracy and precision of tissue mapping [122]. Hence, the effective LL times are determined by the RR interval length. In a single LL experiment, only the first T_1 -weighted image has a short LL time ($<RR$ interval length), while the rest of the images have a long LL time and hence are less sensitive to T_1 . This is more prominent in post-contrast T_1 mapping where T_1 times range from 100 to 600 ms, which will impact the quality of the T_1 map. Other acquisition schemes, such as 4(1)1 for native T_1 , or 3(1)1 or 2(1)2 for post-contrast T_1 , could add another LL anchor at the beginning of the relaxation curve to increase the susceptibility of T_1 , without increasing the scan time more, which necessitates further investigation.

The fully-connected neural network architecture adopted in MyoMapNet was more convenient for the pixel-wise, short, fixed-length input data (10 in native or 8 in post-contrast T_1 MOLLI) than convolutional-based neural networks to learn features from all combinations of the input data with a maximum receptive field. Similar fully-connected based architectures were utilized for simultaneous calculation of T_1 and T_2 maps from MR fingerprinting acquisitions in cardiac and brain imaging [144, 156]. On the other hand, a one-dimensional convolutional neural network was used to estimate T_1 and T_2 maps from a relatively longer input of 220 signal intensity values and inversion time stamps of BLESSPC acquisitions [146]. Other architectures for MyoMapNet can be investigated for T_1 estimations in future studies. MyoMapNet was also successful in estimating T_1 values in two MOLLI sequences, MOLLI-5(3)3, and MOLLI-4(1)3(1)2, which indicates its flexibility and potential generalizability to other T_1 and T_2 sequences. Future studies are warranted to investigate the generalizability of MyoMapNet to alternative T_1

and T_2 sequences.

Our study has several limitations. MyoMapNet was validated using retrospectively acquired data derived from standard MOLLI-5(3)3 and MOLLI-4(1)3(1)2, instead of collecting dedicated data with 4-5 T_1 -weighted images. We only evaluated MyoMapNet using MOLLI data, a similar concept can be investigated for other T_1 mapping sequences. We did not perform any motion correction in T_1 mapping. We used MOLLI sequence for training, and it is widely known that MOLLI has intrinsic under-estimation. Further studies should be pursued to investigate the potential of MyoMapNet to improve measurement accuracy. We used a large dataset of patients with different clinical indications, therefore the clinical utility of MyoMapNet was not studied. Finally, data from a single vendor and field strength was used for training and the generalizability of the trained network for other field strengths or MR vendor should be studied.

5

5.5. CONCLUSION

The MyoMapNet enables fast and precise myocardial T_1 mapping quantification from only 4-5 T_1 -weighted images acquired after a single look-locker sequence, leading to shorter scan time and rapid map reconstruction.

6

DISCUSSION AND CONCLUSIONS

The methods presented in this thesis demonstrate that deep learning (DL) can be applied to accelerate the acquisition of different cardiac MRI sequences, such as dynamic cine imaging for assessing the cardiac function parameters, 3D LGE imaging for myocardial viability assessment, and cardiac T1 mapping for myocardial tissue characterization. DL models exploit a priori knowledge of MR images and undersampling artifact characteristics by learning complex image representations in form of trainable parameters. These learnable parameters can be then utilized to recover the original image quality during the reconstruction process. Generally in all presented methods, a deep learning model was built to learn a mapping function between an accelerated version of the cardiac MRI data and a reference version of high quality by utilizing a large number of trainable parameters in the training phase. These parameters are then used to rapidly reconstruct new accelerated datasets. However, in each study, a different architecture was built and optimized for each imaging sequence separately to exploit its properties and efficiently reconstruct its data, such that:

In the first study, a deep complex convolutional network of U-net architecture was utilized to improve 3D LGE MR image reconstruction from undersampled acquisitions. Although the readily available large datasets of magnitude images are appealing for developing and testing new DL-based techniques, the phase component of MR images also carries important information in the reconstruction process that cannot be ignored. The efficient utilization of phase information in this study via a complex-valued network that preserves the complex nature of the MRI data throughout the reconstruction pipeline allows efficient artifact removal, faster convergence, and better generalization characteristics. This network has therefore enabled superior performance compared to real-valued networks and faster reconstruction of accelerated 3D MRI datasets than compressed-sensing reconstruction methods (i.e. more than 300 fold of acceleration in reconstruction time).

In the second study, a multi-domain network that processes the highly accelerated multi-coil dynamic cardiac MRI data in the spatio-frequency, time, and image domains to recover image quality. This network was designed for efficient radial-view sharing in the k-space via 3D convolutional kernels performed in the k-space, as well as exploiting the spatio-temporal correlations among neighboring time frames. It also builds over the complex-valued network presented in the first study where the complex-valued dynamic data were processed the complex domain throughout the entire reconstruction pipeline. To enable further acceleration, MD-CNN also exploits the redundant information in the multi-coil acquisitions. This architecture enables the efficient reconstruction of highly undersampled radial dynamic imaging with 14 radial views only (i.e. equivalent to 23-folds of acceleration). Using MD-CNN, the entire cardiac cycle, covered by 25 frames, can be captured in a single heartbeat, allowing a substantial reduction in scan time.

In the third study, a fully-connected neural network was utilized to construct accurate T1 maps for the myocardium with more than 50% reduction in breath-holding and scan times. The reduction in breath-holding time is important for patients with breathing difficulties to avoid motion artifacts in the reconstructed maps. This network substantially reduces the reconstruction time to only a few milliseconds compared to conventional curve-fitting methods. This is another example of how DL can reduce the scan and processing times compared to conventional methods.

These studies demonstrate the important role played by DL in accelerating the acquisition of different cardiac MRI sequences with minimal processing times. They also show the potential of DL and neural networks to be easily adapted for accelerating other imaging sequences and modalities. The availability of large training datasets, advanced hardware processing units, and deep learning software packages can also allow fast adoption of these methods in the cardiac MRI workflow to minimize scan time and improve the utility of cardiac MRI.

7

OUTLOOK

In this thesis, we have presented different applications in which DL was successfully able to produce good image quality from accelerated cardiac MRI acquisitions. These studies also highlighted the potential of the DL approach in accelerating different cardiac MRI sequences and paved the way for future studies to successfully transfer these methods into clinical workflow.

A DL approach mainly relies on the availability of large training datasets that adequately represent the possible variations in a specific imaging sequence. A representative dataset includes cases with anatomical variations of the heart due to different diseases, image acquisition variations due to different MRI field strengths, manufacturers, or different pulse sequence optimizations at different clinical centers, ... etc. In our studies, the DL models were trained and validated using relatively large datasets with different cardiac diseases, which included: (a) 3D LGE datasets from 219 patients (17,003 images) with and without myocardial scar in the first study, (b) dynamic cardiac MRI images in 108 patients with various heart conditions and healthy volunteers to train the multi-domain network in the second study, and (c) Myocardial T1 mapping images in 717 patients with various cardiac diseases in the third study. However, for each study, the utilized dataset was acquired at the same center using MRI scanner of the same field strength and manufacturer. To ensure a robust performance independently on the used scanner, pulse sequence optimizations, or anatomical variations among patients, future studies are warranted to train and validate these models on larger datasets that comprehensively include patients with all possible cardiac diseases, different field strengths, multiple manufacturers and clinical centers.

In image reconstruction tasks, DL-based approaches require a dataset with pairs of undersampled and fully-sampled images during the training process. In the first study, acquiring fully-sampled 3D LGE datasets was challenging due to imaging and physiological limitations, and hence the training was performed using a reconstructed datasets by compressed-sensing from undersampled acquisition. The lack of fully-sampled data in this study resulted in suboptimal image quality produced by the presented DL model. A possible way to circumvent the lack of fully-sampled data can be accomplished by using an unsupervised or self-supervised training scheme where the conventional reconstruction approaches can be integrated into a training-based framework to improve the produced image quality. On the other hand, to ensure realistic undersampling artifacts in the accelerated data, prospectively undersampled datasets are often required. In the second and third study, only fully-sampled datasets were acquired and the undersampled version was created by including only a few samples from the fully-sampled acquisitions. Although this approach can produce realistic undersampling artifacts similar to prospective undersampling, future studies that include prospectively accelerated data in the training are warranted.

Current DL models are mainly trained and validated using dedicated graphical processing units (GPUs) to minimize the processing time. However, most of the MRI scanners are not equipped with GPUs in their reconstruction hardware units which can limit the performance of these methods. Several available software packages allow the integration of MRI scanners with external processing units with dedicated GPUs to perform the reconstruction. To utilize the presented methods in the clinical workflow, future efforts can be made towards this goal.

BIBLIOGRAPHY

REFERENCES

- [1] H. Wang, M. Naghavi, C. Allen, R. M. Barber, A. Carter, D. C. Casey, F. J. Charlson, A. Z. Chen, M. M. Coates, M. Coggeshall, L. Dandona, D. J. Dicker, H. E. Erskine, J. A. Haagsma, C. Fitzmaurice, K. Foreman, M. H. Forouzanfar, M. S. Fraser, N. Fullman, E. M. Goldberg, N. Graetz, J. A. Haagsma, S. I. Hay, C. Huynh, C. O. Johnson, N. J. Kassebaum, X. R. Kulikoff, M. Kutz, H. H. Kyu, H. J. Larson, J. Leung, S. S. Lim, M. Lind, R. Lozano, N. Marquez, J. Mikesell, A. H. Mokdad, M. D. Mooney, G. Nguyen, E. Nsoesie, D. M. Pigott, C. Pinho, G. A. Roth, L. Sandar, N. Silpakit, A. Sligar, R. J.D. Sorensen, J. Stanaway, C. Steiner, S. Teeple, R. A. White, H. C. Williams, J. Q. Wong, A. D. Woolf, D. Xavier, G. Xu, B. Yakob, L. L. Yan, P. Yip, N. Yonemoto, G. Yonga, M. Z. Younis, Z. Zaidi, M. E. Zaki, F. Zannad, D. E. Zavala, H. Zeeb, D. Zonies, and L. J. Zuhlke. Global, regional, and national life expectancy, all-cause mortality, and cause-specific mortality for 249 causes of death, 1980–2015: a systematic analysis for the Global Burden of Disease Study 2015. *The Lancet*, 388(10053):1459–1544, oct 2016.
- [2] Daniel R. Messroghli, James C. Moon, Vanessa M. Ferreira, Lars Grosse-Wortmann, Taigang He, Peter Kellman, Julia Mascherbauer, Reza Nezafat, Michael Salerno, Erik B. Schelbert, Andrew J. Taylor, Richard Thompson, Martin Ugander, Ruud B. van Heeswijk, and Matthias G. Friedrich. Clinical recommendations for cardiovascular magnetic resonance mapping of T1, T2, T2* and extracellular volume: A consensus statement by the Society for Cardiovascular Magnetic Resonance (SCMR) endorsed by the European Association for Cardiovascular Imaging (EACVI). *Journal of Cardiovascular Magnetic Resonance*, 19(1):75, dec 2017.
- [3] Florian Von Knobelsdorff-Brenkenhoff and Jeanette Schulz-Menger. Role of cardiovascular magnetic resonance in the guidelines of the European Society of Cardiology. *Journal of Cardiovascular Magnetic Resonance*, 18(1), jan 2016.
- [4] Paul A. Iaizzo. *Handbook of cardiac anatomy, physiology, and devices: Second edition*. Humana Press, 2005.

- [5] Stephen M. Factor, Maria A. Lamberti-Abadi, and Jacobo Abadi. *Handbook of Pathology and Pathophysiology of Cardiovascular Disease*. Springer Science & Business Media, 2006.
- [6] The Heart: Structure and Function; http://www.brainkart.com/article/The-Heart-Structure-and-Function_21076/, 2021.
- [7] Cardiac muscle; https://en.wikipedia.org/wiki/Cardiac_muscle, 2021.
- [8] Robert G Weintraub, Christopher Semsarian, and Peter Macdonald. Dilated cardiomyopathy. *The Lancet*, 390(10092):400–414, jul 2017.
- [9] Heinz Peter Schultheiss, De Lisa Fairweather, Alida L.P. Caforio, Felicitas Escher, Ray E. Hershberger, Steven E. Lipshultz, Peter P. Liu, Akira Matsumori, Andrea Mazzanti, John McMurray, and Silvia G. Priori. Dilated cardiomyopathy. *Nature Reviews Disease Primers*, 5(1), dec 2019.
- [10] A. Luk, E. Ahn, G. S. Soor, and J. Butany. Dilated cardiomyopathy: A review. *Journal of Clinical Pathology*, 62(3):219–225, mar 2009.
- [11] Elizabeth M. McNally and Luisa Mestroni. Dilated cardiomyopathy: Genetic determinants and mechanisms. *Circulation Research*, 121(7):731–748, sep 2017.
- [12] Ravi G. Assomull, Sanjay K. Prasad, Jonathan Lyne, Gillian Smith, Elizabeth D. Burman, Mohammed Khan, Mary N. Sheppard, Philip A. Poole-Wilson, and Dudley J. Pennell. Cardiovascular Magnetic Resonance, Fibrosis, and Prognosis in Dilated Cardiomyopathy. *Journal of the American College of Cardiology*, 48(10):1977–1985, nov 2006.
- [13] Heiko Mahrholdt, Anja Wagner, Robert M. Judd, Udo Sechtem, and Raymond J. Kim. Delayed enhancement cardiovascular magnetic resonance assessment of non-ischaemic cardiomyopathies. *European Heart Journal*, 26(15):1461–1474, aug 2005.
- [14] Katherine C. Wu, Robert G. Weiss, David R. Thiemann, Kakuya Kitagawa, Andre Schmidt, Darshan Dalal, Shenghan Lai, David A. Bluemke, Gary Gerstenblith, Eduardo Marban, Gordon F. Tomaselli, and João A.C. Lima. Late Gadolinium Enhancement by Cardiovascular Magnetic Resonance Heralds an Adverse Prognosis in Nonischemic Cardiomyopathy. *Journal of the American College of Cardiology*, 51(25):2414–2421, jun 2008.
- [15] Shiro Nakamori, Kaoru Dohi, Masaki Ishida, Yoshitaka Goto, Kyoko Imanaka-Yoshida, Taku Omori, Itaru Goto, Naoto Kumagai, Naoki Fujimoto, Yasutaka

- Ichikawa, Kakuya Kitagawa, Norikazu Yamada, Hajime Sakuma, and Masaaki Ito. Native T1 Mapping and Extracellular Volume Mapping for the Assessment of Diffuse Myocardial Fibrosis in Dilated Cardiomyopathy. *JACC: Cardiovascular Imaging*, 11(1):48–59, jan 2018.
- [16] Ali J. Marian and Eugene Braunwald. Hypertrophic cardiomyopathy: Genetics, pathogenesis, clinical manifestations, diagnosis, and therapy. *Circulation Research*, 121(7):749–770, sep 2017.
- [17] Jeffrey B. Geske, Steve R. Ommen, and Bernard J. Gersh. Hypertrophic Cardiomyopathy: Clinical Update. *JACC: Heart Failure*, 6(5):364–375, may 2018.
- [18] Barry J. Maron. Clinical Course and Management of Hypertrophic Cardiomyopathy. *New England Journal of Medicine*, 379(7):655–668, aug 2018.
- [19] Bernard J. Gersh, Barry J. Maron, Robert O. Bonow, Joseph A. Dearani, Michael A. Fifer, Mark S. Link, Srihari S. Naidu, Rick A. Nishimura, Steve R. Ommen, Harry Rakowski, Christine E. Seidman, Jeffrey A. Towbin, James E. Udelson, and Clyde W. Yancy. 2011 ACCF/AHA guideline for the diagnosis and treatment of hypertrophic cardiomyopathy: Executive summary: A report of the American College of cardiology foundation/American heart association task force on practice guidelines. *Circulation*, 124(24):2761–2796, dec 2011.
- [20] Brian A. Houston and Gerin R. Stevens. Hypertrophic cardiomyopathy: A review. *Clinical Medicine Insights: Cardiology*, 8:53–65, 2015.
- [21] Andre Rudolph, Hassan Abdel-Aty, Steffen Bohl, Philipp Boye, Anja Zagrosek, Rainer Dietz, and Jeanette Schulz-Menger. Noninvasive Detection of Fibrosis Applying Contrast-Enhanced Cardiac Magnetic Resonance in Different Forms of Left Ventricular Hypertrophy. Relation to Remodeling. *Journal of the American College of Cardiology*, 53(3):284–291, jan 2009.
- [22] James C.C. Moon, Emma Reed, Mary N. Sheppard, Andrew G. Elkington, Siew Yen Ho, Margaret Burke, Mario Petrou, and Dudley J. Pennell. The histologic basis of late gadolinium enhancement cardiovascular magnetic resonance in hypertrophic cardiomyopathy. *Journal of the American College of Cardiology*, 43(12):2260–2264, jun 2004.
- [23] Peter P. Swoboda, Adam K. McDiarmid, Stephen P. Page, John P. Greenwood, and Sven Plein. Role of T1 mapping in inherited cardiomyopathies. *European Cardiology Review*, 11(2):96–101, 2016.

- [24] L. M. Iles, A. H. Ellims, H. Llewellyn, J. L. Hare, D. M. Kaye, C. A. McLean, and A. J. Taylor. Histological Validation of Cardiac Magnetic Resonance Analysis of Regional and Diffuse Interstitial Myocardial Fibrosis. *European Heart Journal - Cardiovascular Imaging*, 16(1):14–22, jan 2015.
- [25] C J Salton, M L Chuang, C J O'Donnell, M J Kupka, M G Larson, K V Kissinger, R R Edelman, D Levy, and W J Manning. Gender Differences and Normal Left Ventricular Anatomy in An adult Population Free of Hypertension. A Cardiovascular Magnetic Resonance Study of the Framingham Heart Study Offspring Cohort. *Journal of the American College of Cardiology*, 39(6):1055–1060, 2002.
- [26] Aram V. Chobanian, George L. Bakris, Henry R. Black, William C.ushman, Lee A. Green, Joseph L. Izzo, Daniel W. Jones, Barry J. Materson, Suzanne Oparil, Jackson T. Wright, and Edward J. Roccella. Seventh report of the Joint National Committee on Prevention, Detection, Evaluation, and Treatment of High Blood Pressure. *Hypertension*, 42(6):1206–1252, dec 2003.
- [27] Sophie Mavrogeni, Vasiliki Katsi, Vasiliki Vartela, Michel Noutsias, George Markousis-Mavrogenis, Genovefa Kolovou, and Athanasios Manolis. The emerging role of Cardiovascular Magnetic Resonance in the evaluation of hypertensive heart disease. *BMC Cardiovascular Disorders*, 17(1), may 2017.
- [28] Raymond Y. Kwong, Michael Jerosch-Herold, and Bobak Heydari. *Cardiovascular Magnetic Resonance Imaging*. Contemporary Cardiology. Springer New York, New York, NY, 2 edition, 2019.
- [29] Matt A. Bernstein, Kevin F. King, and Xiaohong Joe Zhou. *Handbook of MRI Pulse Sequences*. Elsevier Inc., sep 2004.
- [30] John P. Ridgway. Cardiovascular magnetic resonance physics for clinicians: Part i, 2010.
- [31] Robert W. Brown, Yu Chung N. Cheng, E. Mark Haacke, Michael R. Thompson, and Ramesh Venkatesan. *Magnetic Resonance Imaging: Physical Principles and Sequence Design*, volume 1. John Wiley & Sons Ltd, Chichester, UK, apr 2014.
- [32] Jesse Hamilton, Dominique Franson, and Nicole Seiberlich. Recent advances in parallel imaging for MRI. *Progress in Nuclear Magnetic Resonance Spectroscopy*, 101:71–95, aug 2017.
- [33] John I. Jackson, Craig H. Meyer, Dwight G. Nishimura, and Albert Macovski. Selection of a Convolution Function for Fourier Inversion Using Gridding. *IEEE Transactions on Medical Imaging*, 10(3):473–478, 1991.

- [34] James G. Pipe and Padmanabhan Menon. Sampling density compensation in MRI: Rationale and an iterative numerical solution. *Magnetic Resonance in Medicine*, 41(1):179–186, 1999.
- [35] Kenneth O. Johnson and James G. Pipe. Convolution kernel design and efficient algorithm for sampling density correction. *Magnetic Resonance in Medicine*, 61(2):439–447, feb 2009.
- [36] Nicholas R. Zwart, Kenneth O. Johnson, and James G. Pipe. Efficient sample density estimation by combining gridding and an optimized kernel. *Magnetic Resonance in Medicine*, 67(3):701–710, 2012.
- [37] G. H. Glover and J. M. Pauly. Projection Reconstruction Techniques for Reduction of Motion Effects in MRI. *Magnetic Resonance in Medicine*, 28(2):275–289, 1992.
- [38] John M. Pauly. Reconstruction of Non-Cartesian Data. [Http://Www.Stanford.Edu/Class/Ee369C/Notes/Non Cart Rec](Http://Www.Stanford.Edu/Class/Ee369C/Notes/Non%20Cart%20Rec), 7:39–54, 2007.
- [39] Stefanie Winkelmann, Tobias Schaeffter, Thomas Koehler, Holger Eggers, and Olaf Doessel. An optimal radial profile order based on the golden ratio for time-resolved MRI. *IEEE Transactions on Medical Imaging*, 26(1):68–76, jan 2007.
- [40] Katherine L Wright, Jesse I Hamilton, Mark A Griswold, Vikas Gulani, and Nicole Seiberlich. Non-Cartesian parallel imaging reconstruction. *Journal of magnetic resonance imaging*, 40(5):1022–40, 2014.
- [41] Li Feng, Robert Grimm, Kai Tobias Block, Hersh Chandarana, Sungheon Kim, Jian Xu, Leon Axel, Daniel K. Sodickson, and Ricardo Otazo. Golden-angle radial sparse parallel MRI: Combination of compressed sensing, parallel imaging, and golden-angle radial sampling for fast and flexible dynamic volumetric MRI. *Magnetic Resonance in Medicine*, 72(3):707–717, sep 2014.
- [42] Li Feng, Leon Axel, Hersh Chandarana, Kai Tobias Block, Daniel K. Sodickson, and Ricardo Otazo. XD-GRASP: Golden-angle radial MRI with reconstruction of extra motion-state dimensions using compressed sensing. *Magnetic Resonance in Medicine*, 75(2):775–788, feb 2016.
- [43] V. Rasche, R. W. De Boer, D. Holz, and R. Proksa. Continuous radial data acquisition for dynamic MRI. *Magnetic Resonance in Medicine*, 34(5):754–761, nov 1995.
- [44] Shuo Zhang, Kai Tobias Block, and Jens Frahm. Magnetic resonance imaging in real time: Advances using radial FLASH. *Journal of Magnetic Resonance Imaging*, 31(1):101–109, jan 2010.

- [45] James R. MacFall, Norbert J. Pelc, and Robert M. Vavrek. Correction of spatially dependent phase shifts for partial Fourier imaging. *Magnetic Resonance Imaging*, 6(2):143–155, 1988.
- [46] G. McGibney, M. R. Smith, S. T. Nichols, and A. Crawley. Quantitative evaluation of several partial fourier reconstruction algorithms used in mri. *Magnetic Resonance in Medicine*, 30(1):51–59, 1993.
- [47] D. A. Feinberg, J. D. Hale, J. C. Watts, L. Kaufman, and A. Mark. Halving MR imaging time by conjugation: Demonstration at 3.5 kG. *Radiology*, 161(2):527–531, 1986.
- [48] Mark A. Griswold, Peter M. Jakob, Robin M. Heidemann, Mathias Nittka, Vladimir Jellus, Jianmin Wang, Berthold Kiefer, and Axel Haase. Generalized Autocalibrating Partially Parallel Acquisitions (GRAPPA). *Magnetic Resonance in Medicine*, 47(6):1202–1210, 2002.
- [49] Michael Lustig and John M. Pauly. SPIRiT: Iterative self-consistent parallel imaging reconstruction from arbitrary k-space. *Magnetic Resonance in Medicine*, 64(2):457–471, aug 2010.
- [50] K P Pruessmann, M Weiger, M B Scheidegger, and P Boesiger. SENSE: sensitivity encoding for fast MRI. *Magnetic resonance in medicine*, 42(5):952–62, nov 1999.
- [51] Nicole Seiberlich, Philipp Ehses, Jeff Duerk, Robert Gilkeson, and Mark Griswold. Improved radial GRAPPA calibration for real-time free-breathing cardiac imaging. *Magnetic Resonance in Medicine*, 65(2):492–505, 2011.
- [52] Klaas P. Pruessmann, Markus Weiger, Peter Bornert, and Peter Boesiger. Advances in sensitivity encoding with arbitrary k-space trajectories. *Magnetic Resonance in Medicine*, 46(4):638–651, oct 2001.
- [53] Anagha Deshmane, Vikas Gulani, Mark A. Griswold, and Nicole Seiberlich. Parallel MR imaging. *Journal of Magnetic Resonance Imaging*, 36(1):55–72, jul 2012.
- [54] MA Griswold, RM Heidemann, and PM Jakob. Direct parallel imaging reconstruction of radially sampled data using GRAPPA with relative shifts. In *International Society for Magnetic Resonance in Medicine (ISMRM)*, 2003.
- [55] Keith Heberlein and Xiaoping Hu. Auto-calibrated parallel spiral imaging. *Magnetic Resonance in Medicine*, 55(3):619–625, 2006.
- [56] Mark Murphy, Marcus Alley, James Demmel, Kurt Keutzer, Shreyas Vasanawala, and Michael Lustig. Fast lFix ME!-SPIRiT compressed sensing parallel imaging

- MRI: scalable parallel implementation and clinically feasible runtime. *IEEE transactions on medical imaging*, 31(6):1250–1262, jun 2012.
- [57] Martin Uecker, Peng Lai, Mark J. Murphy, Patrick Virtue, Michael Elad, John M. Pauly, Shreyas S. Vasanawala, and Michael Lustig. ESPIRiT - An eigenvalue approach to autocalibrating parallel MRI: Where SENSE meets GRAPPA. *Magnetic Resonance in Medicine*, 71(3):990–1001, mar 2014.
- [58] Aurelien Bustin, Niccolo Fuin, Rene M. Botnar, and Claudia Prieto. From Compressed-Sensing to Artificial Intelligence-Based Cardiac MRI Reconstruction. *Frontiers in Cardiovascular Medicine*, 7:17, feb 2020.
- [59] David L. Donoho. Compressed sensing. *IEEE Transactions on Information Theory*, 52(4):1289–1306, apr 2006.
- [60] Michael Lustig, David Donoho, and John M. Pauly. Sparse MRI: The application of compressed sensing for rapid MR imaging. *Magnetic Resonance in Medicine*, 58(6):1182–1195, dec 2007.
- [61] Michael Lustig, David L. Donoho, Juan M. Santos, and John M. Pauly. Compressed sensing MRI: A look at how CS can improve on current imaging techniques. *IEEE Signal Processing Magazine*, 25(2):72–82, 2008.
- [62] Mehmet Akcakaya, Tamer A. Basha, Beth Goddu, Lois A. Goepfert, Kraig V. Kissinger, Vahid Tarokh, Warren J. Manning, and Reza Nezafat. Low-dimensional-structure self-learning and thresholding: Regularization beyond compressed sensing for MRI Reconstruction. *Magnetic Resonance in Medicine*, 66(3):756–767, 2011.
- [63] Li Feng, Monvadi B. Srichai, Ruth P. Lim, Alexis Harrison, Wilson King, Ganesh Adluru, Edward V.R. Dibella, Daniel K. Sodickson, Ricardo Otazo, and Daniel Kim. Highly accelerated real-time cardiac cine MRI using k-t SPARSE-SENSE. *Magnetic Resonance in Medicine*, 70(1):64–74, jul 2013.
- [64] Tomoyuki Kido, Teruhito Kido, Masashi Nakamura, Kouki Watanabe, Michaela Schmidt, Christoph Forman, and Teruhito Mochizuki. Compressed sensing real-time cine cardiovascular magnetic resonance: Accurate assessment of left ventricular function in a single-breath-hold. *Journal of Cardiovascular Magnetic Resonance*, 18(1):50, aug 2016.
- [65] Seunghoon Nam, Mehmet Akcakaya, Tamer Basha, Christian Stehning, Warren J. Manning, Vahid Tarokh, and Reza Nezafat. Compressed sensing reconstruction

- for whole-heart imaging with 3D radial trajectories: A graphics processing unit implementation. *Magnetic Resonance in Medicine*, 69(1):91–102, 2013.
- [66] Kyong Hwan Jin, Dongwook Lee, and Jong Chul Ye. A General Framework for Compressed Sensing and Parallel MRI Using Annihilating Filter Based Low-Rank Hankel Matrix. *IEEE Transactions on Computational Imaging*, 2(4):480–495, aug 2016.
- [67] F. Liu, Y. Duan, B. S. Peterson, and A. Kangarlu. Compressed sensing MRI combined with SENSE in partial k-space. *Physics in Medicine and Biology*, 57(21), 2012.
- [68] Ricardo Otazo, Daniel Kim, Leon Axel, and Daniel K. Sodickson. Combination of compressed sensing and parallel imaging for highly accelerated first-pass cardiac perfusion MRI. *Magnetic Resonance in Medicine*, 64(3):767–776, 2010.
- [69] Jose Caballero, Anthony N. Price, Daniel Rueckert, and Joseph V. Hajnal. Dictionary Learning and Time Sparsity for Dynamic MR Data Reconstruction. *IEEE Transactions on Medical Imaging*, 33(4):979–994, apr 2014.
- [70] Saiprasad Ravishankar and Yoram Bresler. MR image reconstruction from highly undersampled k-space data by dictionary learning. *IEEE Transactions on Medical Imaging*, 30(5):1028–1041, 2011.
- [71] Ying Song, Zhen Zhu, Yang Lu, Qiegen Liu, and Jun Zhao. Reconstruction of magnetic resonance imaging by three-dimensional dual-dictionary learning. *Magnetic Resonance in Medicine*, 71(3):1285–1298, mar 2014.
- [72] Zhifang Zhan, Jian Feng Cai, Di Guo, Yunsong Liu, Zhong Chen, and Xiaobo Qu. Fast Multiclass Dictionaries Learning with Geometrical Directions in MRI Reconstruction. *IEEE Transactions on Biomedical Engineering*, 63(9):1850–1861, sep 2016.
- [73] Michal Aharon, Michael Elad, and Alfred Bruckstein. K-SVD: An algorithm for designing overcomplete dictionaries for sparse representation. *IEEE Transactions on Signal Processing*, 54(11):4311–4322, nov 2006.
- [74] Shanshan Wang, Sha Tan, Yuan Gao, Qiegen Liu, Leslie Ying, Taohui Xiao, Yuanyuan Liu, Xin Liu, Hairong Zheng, and Dong Liang. Learning Joint-Sparse Codes for Calibration-Free Parallel MR Imaging. *IEEE Transactions on Medical Imaging*, 37(1):251–261, jan 2018.
- [75] Daniel Weller. Reconstruction with dictionary learning for accelerated parallel magnetic resonance imaging. In *Proceedings of the IEEE Southwest Symposium*

- on Image Analysis and Interpretation*, volume 2016-April, pages 105–108. Institute of Electrical and Electronics Engineers Inc., apr 2016.
- [76] Mehmet Akcakaya, Steen Moeller, Sebastian Weingartner, and Kamil Uğurbil. Scan-specific robust artificial-neural-networks for k-space interpolation (RAKI) reconstruction: Database-free deep learning for fast imaging. *Magnetic Resonance in Medicine*, 81(1):439–453, jan 2019.
- [77] Kerstin Hammernik, Teresa Klatzer, Erich Kobler, Michael P. Recht, Daniel K. Sodickson, Thomas Pock, and Florian Knoll. Learning a variational network for reconstruction of accelerated MRI data. *Magnetic Resonance in Medicine*, 79(6):3055–3071, 2018.
- [78] Andreas Hauptmann, Simon Arridge, Felix Lucka, Vivek Muthurangu, and Jennifer A. Steeden. Real-time cardiovascular MR with spatio-temporal artifact suppression using deep learning—proof of concept in congenital heart disease. *Magnetic Resonance in Medicine*, 81(2):1143–1156, feb 2019.
- [79] Chen Qin, Jo Schlemper, Jose Caballero, Anthony N. Price, Joseph V. Hajnal, and Daniel Rueckert. Convolutional Recurrent Neural Networks for Dynamic MR Image Reconstruction. *IEEE Transactions on Medical Imaging*, 38(1):280–290, jan 2019.
- [80] Jo Schlemper, Jose Caballero, Joseph V. Hajnal, Anthony N. Price, and Daniel Rueckert. A Deep Cascade of Convolutional Neural Networks for Dynamic MR Image Reconstruction. *IEEE Transactions on Medical Imaging*, 37(2):491–503, feb 2018.
- [81] Shanshan Wang, Huitao Cheng, Leslie Ying, Taohui Xiao, Ziwen Ke, Xin Liu, Hairong Zheng, and Dong Liang. DeepcomplexMRI: Exploiting deep residual network for fast parallel MR imaging with complex convolution. *Magnetic Resonance Imaging*, 68:136–147, jun 2019.
- [82] Shanshan Wang, Ziwen Ke, Huitao Cheng, Sen Jia, Leslie Ying, Hairong Zheng, and Dong Liang. DIMENSION: Dynamic MR imaging with both k-space and spatial prior knowledge obtained via multi-supervised network training. *NMR in Biomedicine*, page e4131, sep 2019.
- [83] Morteza Mardani, Enhao Gong, Joseph Y. Cheng, Shreyas S. Vasanawala, Greg Zaharchuk, Lei Xing, and John M. Pauly. Deep Generative Adversarial Neural Networks for Compressive Sensing (GANCS) MRI. *IEEE Transactions on Medical Imaging*, 38(1):167–179, 2018.

- [84] Tran Minh Quan, Thanh Nguyen-Duc, and Won-Ki Jeong. Compressed Sensing MRI Reconstruction Using a Generative Adversarial Network With a Cyclic Loss. *IEEE transactions on medical imaging*, 37(6):1488–1497, jun 2018.
- [85] Guang Yang, Simiao Yu, Hao Dong, Greg Slabaugh, Pier Luigi Dragotti, Xujiong Ye, Fangde Liu, Simon Arridge, Jennifer Keegan, Yike Guo, David Firmin, Jennifer Keegan, Greg Slabaugh, Simon Arridge, Xujiong Ye, Yike Guo, Simiao Yu, Fangde Liu, David Firmin, Pier Luigi Dragotti, Guang Yang, and Hao Dong. DAGAN: Deep De-Aliasing Generative Adversarial Networks for Fast Compressed Sensing MRI Reconstruction. *IEEE Transactions on Medical Imaging*, 37(6):1310–1321, jun 2018.
- [86] Andreas Kofler, Marc Dewey, Tobias Schaeffter, Christian Wald, and Christoph Kolbitsch. Spatio-Temporal Deep Learning-Based Undersampling Artefact Reduction for 2D Radial Cine MRI with Limited Training Data. *IEEE Transactions on Medical Imaging*, 39(3):703–717, mar 2020.
- [87] Godwin Constantine, Kesavan Shan, Scott D. Flamm, and Mohan U. Sivananthan. Role of MRI in clinical cardiology. *Lancet*, 363(9427):2162–2171, jun 2004.
- [88] Sohrab Fratz, Taylor Chung, Gerald F. Greil, Margaret M. Samyn, Andrew M. Taylor, Emanuela R. Valsangiacomo Buechel, Shi Joon Yoo, and Andrew J. Powell. Guidelines and protocols for cardiovascular magnetic resonance in children and adults with congenital heart disease: SCMR expert consensus group on congenital heart disease. *Journal of Cardiovascular Magnetic Resonance*, 15(1):51, 2013.
- [89] W. Gregory Hundley, David A. Bluemke, J. Paul Finn, Scott D. Flamm, Mark A. Fogel, Matthias G. Friedrich, Vincent B. Ho, Michael Jerosch-Herold, Christopher M. Kramer, Warren J. Manning, Manesh Patel, Gerald M. Pohost, Arthur E. Stillman, Richard D. White, Pamela K. Woodard, Robert A. Harrington, Jeffrey L. Anderson, Eric R. Bates, Charles R. Bridges, Mark J. Eisenberg, Victor A. Ferrari, Cindy L. Grines, Mark A. Hlatky, Alice K. Jacobs, Sanjay Kaul, Robert C. Lichtenberg, Jonathan R. Lindner, David J. Moliterno, Debabrata Mukherjee, Robert S. Rosenson, Richard S. Schofield, Samuel J. Shubrooks, James H. Stein, Cynthia M. Tracy, Howard H. Weitz, and Deborah J. Wesley. ACCF/ACR/AHA/NASCI/SCMR 2010 expert consensus document on cardiovascular magnetic resonance: A report of the american college of cardiology foundation task force on expert consensus documents. *Circulation*, 121(22):2462–2508, jun 2010.
- [90] Rosa Maria Menchon-Lara, Federico Simmross-Wattenberg, Pablo Casaseca-de-la Higuera, Marcos Martin-Fernandez, and Carlos Alberola-Lopez. Reconstruction techniques for cardiac cine MRI. *Insights into Imaging*, 10(1), dec 2019.

- [91] James C. Carr, Orlando Simonetti, Jeff Bundy, Debiao Li, Scott Pereles, and J. Paul Finn. Cine MR angiography of the heart with segmented true fast imaging with steady-state precession. *Radiology*, 219(3):828–834, 2001.
- [92] Christopher M. Kramer, Jörg Barkhausen, Chiara Bucciarelli-Ducci, Scott D. Flamm, Raymond J. Kim, and Eike Nagel. Standardized cardiovascular magnetic resonance imaging (CMR) protocols: 2020 update. *Journal of Cardiovascular Magnetic Resonance*, 22(1):17, feb 2020.
- [93] Andrew D. Scott, Jennifer Keegan, and David N. Firmin. Motion in cardiovascular MR imaging. *Radiology*, 250(2):331–351, feb 2009.
- [94] David A. Bluemke, Jerrold L. Boxerman, Ergin Atalar, and Elliot R. McVeigh. Segmented K-space cine breath-hold cardiovascular MR imaging: Part 1. Principles and technique. *American Journal of Roentgenology*, 169(2):395–400, 1997.
- [95] Martin Krämer, Karl Heinz Herrmann, Judith Biermann, and Jurgen R. Reichenbach. Retrospective reconstruction of cardiac cine images from golden-ratio radial MRI using one-dimensional navigators. *Journal of Magnetic Resonance Imaging*, 40(2):413–422, 2014.
- [96] Andrew C. Larson, Richard D. White, Gerhard Laub, Elliot R. McVeigh, Debiao Li, and Orlando P. Simonetti. Self-Gated Cardiac Cine MRI. *Magnetic Resonance in Medicine*, 51(1):93–102, 2004.
- [97] Dana C. Peters, Reza Nezafat, Holger Eggers, Christian Stehning, and Warren J. Manning. 2D free-breathing dual navigator-gated cardiac function validated against the 2D breath-hold acquisition. *Journal of Magnetic Resonance Imaging*, 28(3):773–777, sep 2008.
- [98] Hassan Haji-Valizadeh, Amir A. Rahsepar, Jeremy D. Collins, Elwin Bassett, Tamara Isakova, Tobias Block, Ganesh Adluru, Edward V.R. DiBella, Daniel C. Lee, James C. Carr, and Daniel Kim. Validation of highly accelerated real-time cardiac cine MRI with radial k-space sampling and compressed sensing in patients at 1.5T and 3T. *Magnetic Resonance in Medicine*, 79(5):2745–2751, may 2018.
- [99] Dirk Voit, Shuo Zhang, Christina Unterberg-Buchwald, Jan M. Sohns, Joachim Lotz, and Jens Frahm. Real-time cardiovascular magnetic resonance at 1.5 T using balanced SSFP and 40 ms resolution. *Journal of Cardiovascular Magnetic Resonance*, 15(1):79, sep 2013.

- [100] Raymond J. Kim, Edwin Wu, Allen Rafael, Enn-Ling Chen, Michele A. Parker, Orlando Simonetti, Francis J. Klocke, Robert O. Bonow, and Robert M. Judd. The Use of Contrast-Enhanced Magnetic Resonance Imaging to Identify Reversible Myocardial Dysfunction. *New England Journal of Medicine*, 343(20):1445–1453, nov 2000.
- [101] W. Patricia Ingkanisorn, Kenneth L. Rhoads, Anthony H. Aletras, Peter Kellman, and Andrew E. Arai. Gadolinium delayed enhancement cardiovascular magnetic resonance correlates with clinical measures of myocardial infarction. *Journal of the American College of Cardiology*, 43(12):2253–2259, jun 2004.
- [102] Lubna Choudhury, Heiko Mahrholdt, Anja Wagner, Kelly M. Choi, Michael D. Elliott, Francis J. Klocke, Robert O. Bonow, Robert M. Judd, and Raymond J. Kim. Myocardial scarring in asymptomatic or mildly symptomatic patients with hypertrophic cardiomyopathy. *Journal of the American College of Cardiology*, 40(12):2156–2164, dec 2002.
- [103] Christopher M. Kramer, Jörg Barkhausen, Scott D. Flamm, Raymond J. Kim, and Eike Nagel. Standardized cardiovascular magnetic resonance (CMR) protocols 2013 update. *Journal of Cardiovascular Magnetic Resonance*, 15(1):91, dec 2013.
- [104] Christopher J. McGann, Eugene G. Kholmovski, Robert S. Oakes, Joshua J.E. Blauer, Marcos Daccarett, Nathan Segerson, Kelly J. Airey, Nazem Akoum, Eric Fish, Troy J. Badger, Edward V.R. DiBella, Dennis Parker, Rob S. MacLeod, and Nassir F. Marrouche. New Magnetic Resonance Imaging-Based Method for Defining the Extent of Left Atrial Wall Injury After the Ablation of Atrial Fibrillation. *Journal of the American College of Cardiology*, 52(15):1263–1271, oct 2008.
- [105] Mehmet Akcakaya, Hussein Rayatzadeh, Tamer A. Basha, Susie N. Hong, Raymond H. Chan, Kraig V. Kissinger, Thomas H. Hauser, Mark E. Josephson, Warren J. Manning, and Reza Nezafat. Accelerated Late Gadolinium Enhancement Cardiac MR Imaging with Isotropic Spatial Resolution Using Compressed Sensing: Initial Experience. *Radiology*, 264(3):691–699, sep 2012.
- [106] Christine L Jellis and Deborah H Kwon. Myocardial T1 mapping: modalities and clinical applications. *Cardiovascular diagnosis and therapy*, 4(2):126–137, 2014.
- [107] Andrew J. Taylor, Michael Salerno, Rohan Dharmakumar, and Michael Jerosch-Herold. T1 Mapping Basic Techniques and Clinical Applications. *JACC: Cardiovascular Imaging*, 9(1):67–81, jan 2016.

- [108] Philip Haaf, Pankaj Garg, Daniel R. Messroghli, David A. Broadbent, John P. Greenwood, and Sven Plein. Cardiac T1 Mapping and Extracellular Volume (ECV) in clinical practice: A comprehensive review. *Journal of Cardiovascular Magnetic Resonance*, 18(1):89, nov 2016.
- [109] Stefan K. Piechnik, Vanessa M. Ferreira, Erica DallArmellina, Lowri E. Cochlin, Andreas Greiser, Stefan Neubauer, and Matthew D. Robson. Shortened Modified Look-Locker Inversion recovery (ShMOLLI) for clinical myocardial T1 mapping at 1.5 and 3 T within a 9 heartbeat breathhold. *Journal of Cardiovascular Magnetic Resonance*, 12(1):69, 2010.
- [110] Kelvin Chow, Jacqueline A. Flewitt, Jordin D. Green, Joseph J. Pagano, Matthias G. Friedrich, and Richard B. Thompson. Saturation recovery single-shot acquisition (SASHA) for myocardial T1 mapping. *Magnetic Resonance in Medicine*, 71(6):2082–2095, 2014.
- [111] Sebastian Weingartner, Sebastien Roujol, Mehmet Akcakaya, Tamer A. Basha, and Reza Nezafat. Free-breathing multislice native myocardial T1 mapping using the slice-interleaved T1 (STONE) sequence. *Magnetic Resonance in Medicine*, 74(1):115–124, jul 2015.
- [112] Hossam El-Rewaidy, Maryam Nezafat, Jihye Jang, Shiro Nakamori, Ahmed S. Fahmy, and Reza Nezafat. Nonrigid Active Shape Model-Based Registration Framework for Motion Correction of Cardiac T1 Mapping. *Magnetic Resonance in Medicine*, 80(2):780–791, aug 2018.
- [113] Sebastien Roujol, Tamer A. Basha, Sebastian Weingartner, Mehmet Akcakaya, Sophie Berg, Warren J. Manning, and Reza Nezafat. Impact of motion correction on reproducibility and spatial variability of quantitative myocardial T2 mapping. *Journal of Cardiovascular Magnetic Resonance*, 17(1), jun 2015.
- [114] Hossam El-Rewaidy, Ulf Neisius, Jennifer Mancio, Selcuk Kucukseymen, Jennifer Rodriguez, Amanda Paskavitz, Bjoern Menze, and Reza Nezafat. Deep complex convolutional network for fast reconstruction of 3D late gadolinium enhancement cardiac MRI. *NMR in Biomedicine*, 33(7):e4312, apr 2020.
- [115] Hossam El-Rewaidy, Ahmed S. Fahmy, Farhad Pashakhanloo, Xiaoying Cai, Selcuk Kucukseymen, Ibolya Csecs, Ulf Neisius, Hassan Haji-Valizadeh, Bjoern Menze, and Reza Nezafat. Multi-domain convolutional neural network (MD-CNN) for radial reconstruction of dynamic cardiac MRI. *Magnetic Resonance in Medicine*, 85(3):1195–1208, mar 2021.

- [116] Michelle Fitts, Elodie Breton, Eugene G. Kholmovski, Derek J. Dossdall, Sathya Vijayakumar, Kyung P. Hong, Ravi Ranjan, Nassir F. Marrouche, Leon Axel, and Daniel Kim. Arrhythmia insensitive rapid cardiac T1 mapping pulse sequence. *Magnetic Resonance in Medicine*, 70(5):1274–1282, nov 2013.
- [117] Rui Guo, Xiaoying Cai, Selcuk Kucukseymen, Jennifer Rodriguez, Amanda Paskavitz, Patrick Pierce, Beth Goddu, and Reza Nezafat. Free-breathing whole-heart multi-slice myocardial T1 mapping in 2 minutes. *Magnetic Resonance in Medicine*, 85(1):89–102, jan 2021.
- [118] Bhairav B. Mehta, Xiao Chen, Kenneth C. Bilchick, Michael Salerno, and Frederick H. Epstein. Accelerated and navigator-gated look-locker imaging for cardiac T1 estimation (ANGIE): Development and application to T1 mapping of the right ventricle. *Magnetic Resonance in Medicine*, 73(1):150–160, jan 2015.
- [119] Daniel R. Messroghli, Aleksandra Radjenovic, Sebastian Kozerke, David M. Higgins, Mohan U. Sivananthan, and John P. Ridgway. Modified Look-Locker inversion recovery (MOLLI) for high-resolution T1 mapping of the heart. *Magnetic Resonance in Medicine*, 52(1):141–146, jul 2004.
- [120] Sebastien Roujol, Sebastian Weingartner, Murilo Foppa, Kelvin Chow, Keigo Kawaji, Long H. Ngo, Peter Kellman, Warren J. Manning, Richard B. Thompson, and Reza Nezafat. Accuracy, precision, and reproducibility of four T1 mapping sequences: A head-to-head comparison of MOLLI, ShMOLLI, SASHA, and SAPPHIRE. *Radiology*, 272(3):683–689, 2014.
- [121] Sebastian Weingartner, Mehmet Akcakaya, Tamer Basha, Kraig V. Kissinger, Beth Goddu, Sophie Berg, Warren J. Manning, and Reza Nezafat. Combined saturation/inversion recovery sequences for improved evaluation of scar and diffuse fibrosis in patients with arrhythmia or heart rate variability. *Magnetic Resonance in Medicine*, 71(3):1024–1034, 2014.
- [122] Mehmet Akcakaya, Sebastian Weingartner, Sebastien Roujol, and Reza Nezafat. On the selection of sampling points for myocardial T1 mapping. *Magnetic Resonance in Medicine*, 73(5):1741–1753, 2015.
- [123] Rui Guo, Zhensen Chen, Daniel A. Herzka, Jianwen Luo, and Haiyan Ding. A three-dimensional free-breathing sequence for simultaneous myocardial T1 and T2 mapping. *Magnetic Resonance in Medicine*, 81(2):1031–1043, feb 2019.
- [124] Peter Kellman and Michael S. Hansen. T1 mapping in the heart: Accuracy and precision. *Journal of Cardiovascular Magnetic Resonance*, 16(1):2, jan 2014.

- [125] Sofia Kvernby, Marcel J. van Bertus Warntjes, Henrik Haraldsson, Carl Johan Carlhäll, Jan Engvall, and Tino Ebbers. Simultaneous three-dimensional myocardial T1 and T2 mapping in one breath hold with 3D-QALAS. *Journal of cardiovascular magnetic resonance*, 16(1):102, 2014.
- [126] Giovanna Nordio, Aurelien Bustin, Markus Henningsson, Imran Rashid, Amedeo Chiribiri, Tevfik Ismail, Freddy Odille, Claudia Prieto, and Rene Michael Botnar. 3D SASHA myocardial T1 mapping with high accuracy and improved precision. *Magnetic Resonance Materials in Physics, Biology and Medicine*, 32(2):281–289, apr 2019.
- [127] Giovanna Nordio, Markus Henningsson, Amedeo Chiribiri, Adriana D.M. Villa, Torben Schneider, and Rene M. Botnar. 3D myocardial T1 mapping using saturation recovery. *Journal of Magnetic Resonance Imaging*, 46(1):218–227, 2017.
- [128] Giovanna Nordio, Torben Schneider, Gastao Cruz, Teresa Correia, Aurelien Bustin, Claudia Prieto, Rene M. Botnar, and Markus Henningsson. Whole-heart T1 mapping using a 2D fat image navigator for respiratory motion compensation. *Magnetic Resonance in Medicine*, 83(1):178–187, jan 2020.
- [129] Haikun Qi, Aurelien Bustin, Gastao Cruz, Olivier Jaubert, Huijun Chen, Rene M. Botnar, and Claudia Prieto. Free-running simultaneous myocardial T1/T2 mapping and cine imaging with 3D whole-heart coverage and isotropic spatial resolution. *Magnetic Resonance Imaging*, 63:159–169, nov 2019.
- [130] Jiaxin Shao, Dapeng Liu, Kyunghyun Sung, Kim Lien Nguyen, and Peng Hu. Accuracy, precision, and reproducibility of myocardial T1 mapping: A comparison of four T1 estimation algorithms for modified look-locker inversion recovery (MOLLI). *Magnetic Resonance in Medicine*, 78(5):1746–1756, nov 2017.
- [131] Sebastian Weingartner, Mehmet Akcakaya, Sebastien Roujol, Tamer Basha, Cory Tschabrunn, Sophie Berg, Elad Anter, and Reza Nezafat. Free-breathing combined three-dimensional phase sensitive late gadolinium enhancement and T1 mapping for myocardial tissue characterization. *Magnetic Resonance in Medicine*, 74(4):1032–1041, 2015.
- [132] Sebastian Weingartner, Mehmet Akcakaya, Sebastien Roujol, Tamer Basha, Christian Stehning, Kraig V. Kissinger, Beth Goddu, Sophie Berg, Warren J. Manning, and Reza Nezafat. Free-breathing post-contrast three-dimensional T1 mapping: Volumetric assessment of myocardial T1 values. *Magnetic Resonance in Medicine*, 73(1):214–222, jan 2015.

- [133] Christos G. Xanthis, Sebastian Bidhult, Andreas Greiser, Kelvin Chow, Richard B. Thompson, Håkan Arheden, and Anthony H. Aletras. Simulation-based quantification of native T1 and T2 of the myocardium using a modified MOLLI scheme and the importance of Magnetization Transfer. *Magnetic Resonance Imaging*, 48:96–106, may 2018.
- [134] Mehmet Akcakaya, Sebastian Weingartner, Tamer A. Basha, Sebastien Roujol, Steven Bellm, and Reza Nezafat. Joint myocardial T1 and T2 mapping using a combination of saturation recovery and T2-preparation. *Magnetic Resonance in Medicine*, 76(3):888–896, sep 2016.
- [135] Rui Guo, Xiaoying Cai, Selcuk Kucukseymen, Jennifer Rodriguez, Amanda Paskavitz, Patrick Pierce, Beth Goddu, Richard B. Thompson, and Reza Nezafat. Free-breathing simultaneous myocardial T1 and T2 mapping with whole left ventricle coverage. *Magnetic Resonance in Medicine*, 85(3), mar 2020.
- [136] Sofia Kvernby, Marcel Warntjes, Jan Engvall, Carl Johan Carlhäll, and Tino Ebbers. Clinical feasibility of 3D-QALAS – Single breath-hold 3D myocardial T1- and T2-mapping. *Magnetic Resonance Imaging*, 38:13–20, may 2017.
- [137] Jesse I. Hamilton, Yun Jiang, Yong Chen, Dan Ma, Wei Ching Lo, Mark Griswold, and Nicole Seiberlich. MR fingerprinting for rapid quantification of myocardial T1, T2, and proton spin density. *Magnetic Resonance in Medicine*, 77(4):1446–1458, apr 2017.
- [138] O. Jaubert, G. Cruz, A. Bustin, T. Schneider, P. Koken, M. Doneva, D. Rueckert, R. M. Botnar, and C. Prieto. Free-running cardiac magnetic resonance fingerprinting: Joint T1/T2 map and Cine imaging. *Magnetic Resonance Imaging*, 68:173–182, may 2020.
- [139] Anthony G. Christodoulou, Jaime L. Shaw, Christopher Nguyen, Qi Yang, Yibin Xie, Nan Wang, and Debiao Li. Magnetic resonance multitasking for motion-resolved quantitative cardiovascular imaging. *Nature Biomedical Engineering*, 2(4):215–226, apr 2018.
- [140] Peter Kellman, Andrew E. Arai, and Hui Xue. T1 and extracellular volume mapping in the heart: Estimation of error maps and the influence of noise on precision. *Journal of Cardiovascular Magnetic Resonance*, 15(1):56, 2013.
- [141] Marshall S. Sussman and Bernd J. Wintersperger. Modified look-locker inversion recovery (MOLLI) T1 mapping with inversion group (IG) fitting – A method for improved precision. *Magnetic Resonance Imaging*, 62:38–45, oct 2019.

- [142] Marshall S. Sussman, Issac Y. Yang, Kai Ho Fok, and Bernd J. Wintersperger. Inversion group (IG) fitting: A new T1 mapping method for modified look-locker inversion recovery (MOLLI) that allows arbitrary inversion groupings and rest periods (including no rest period). *Magnetic Resonance in Medicine*, 75(6):2332–2340, jun 2016.
- [143] Luigia DErrico, Marshall S. Sussman, Kate Hanneman, and Bernd J. Wintersperger. Precision-optimized single protocol pre-/post-contrast modified-look locker inversion T1 mapping using composite inversion group fitting. *Magnetic Resonance Imaging*, 74:195–202, dec 2020.
- [144] Jesse I. Hamilton, Danielle Currey, Sanjay Rajagopalan, and Nicole Seiberlich. Deep learning reconstruction for cardiac magnetic resonance fingerprinting T1 and T2 mapping. *Magnetic Resonance in Medicine*, 2020.
- [145] Maryam Nezafat, Hossam El-Rewaify, Selcuk Kucukseymen, Thomas H Hauser, and Ahmed S Fahmy. Deep convolution neural networks based artifact suppression in under-sampled radial acquisitions of myocardial T1 mapping images. *Physics in Medicine & Biology*, 65(22):225024, nov 2020.
- [146] Jiaxin Shao, Vahid Ghodrati, Kim Lien Nguyen, and Peng Hu. Fast and accurate calculation of myocardial T1 and T2 values using deep learning Bloch equation simulations (DeepBLESS). *Magnetic Resonance in Medicine*, 84(5):2831–2845, nov 2020.
- [147] Olympia Gatsoni, Anthony H. Aletras, Einar Heiberg, and Klas Berggran. T1 Mapping By Means Of Deep Learning Neural Networks Using Both Saturation Recovery and Inversion Recovery Data. In *Society for Cardiovascular Magnetic Resonance (SCMR)*, Orlando, FL, 2020.
- [148] Douglas Bates, Martin Mächler, Benjamin M. Bolker, and Steven C. Walker. Fitting linear mixed-effects models using lme4. *Journal of Statistical Software*, 67(1):1–48, oct 2015.
- [149] Kirsten M. Becker, Edyta Blaszczyk, Stephanie Funk, Andre Nuesslein, Jeanette Schulz-Menger, Tobias Schaeffter, and Christoph Kolbitsch. Fast myocardial T1 mapping using cardiac motion correction. *Magnetic Resonance in Medicine*, 83(2):438–451, feb 2020.
- [150] Michael A. Bush, Yue Pan, Ning Jin, Yingmin Liu, Juliet Varghese, Rizwan Ahmad, and Orlando P. Simonetti. Prospective correction of patient-specific respira-

- tory motion in myocardial T1 and T2 mapping. *Magnetic Resonance in Medicine*, 85(2):855–867, feb 2021.
- [151] Hui Xue, Saurabh Shah, Andreas Greiser, Christoph Guetter, Arne Littmann, Marie Pierre Jolly, Andrew E. Arai, Sven Zuehlsdorff, Jens Guehring, and Peter Kellman. Motion correction for myocardial T1 mapping using image registration with synthetic image estimation. *Magnetic Resonance in Medicine*, 67(6):1644–1655, 2012.
- [152] Yanjie Zhu, Jinkyu Kang, Chong Duan, Maryam Nezafat, Ulf Neisius, Jihye Jang, and Reza Nezafat. Integrated motion correction and dictionary learning for free-breathing myocardial T1 mapping. *Magnetic Resonance in Medicine*, 81(4):2644–2654, apr 2019.
- [153] Tim Leiner, Daniel Rueckert, Avan Suinesiaputra, Bettina Baessler, Reza Nezafat, Ivana Isgum, and Alistair A Young. Machine learning in cardiovascular magnetic resonance: Basic concepts and applications. *Journal of Cardiovascular Magnetic Resonance*, 21(1), oct 2019.
- [154] A.S. Fahmy, H. El-Rewaidy, M. Nezafat, S. Nakamori, and R. Nezafat. Automated analysis of cardiovascular magnetic resonance myocardial native T1 mapping images using fully convolutional neural networks. *Journal of Cardiovascular Magnetic Resonance*, 21(1):7, 2019.
- [155] Qiang Zhang, Evan Hann, Konrad Werys, Cody Wu, Iulia Popescu, Elena Lukaschuk, Ahmet Barutcu, Vanessa M. Ferreira, and Stefan K. Piechnik. Deep learning with attention supervision for automated motion artefact detection in quality control of cardiac T1-mapping. *Artificial Intelligence in Medicine*, 110, nov 2020.
- [156] Ouri Cohen, Bo Zhu, and Matthew S. Rosen. MR fingerprinting Deep RecOnstruction Network (DRONE). *Magnetic Resonance in Medicine*, 80(3):885–894, 2018.

LIST OF FIGURES

2.1	Heart structures [6].	6
2.2	The heart wall [7].	7
2.3	MRI Magnetization [28].	9
2.4	MRI Excitation [28].	9
2.5	T_1 Relaxation [30].	10
2.6	T_2 Relaxation [30].	11
2.7	Image Acquisition [28].	12
2.8	Image Reconstruction.	12
2.9	Examples of different cartesian and non-cartesian k-space trajectories. Solid and dotted trajectory arrows indicate the location of acquired and skipped k-space lines, respectively (a) Fully-sampled Cartesian trajectory and its corresponding artifact-free image (b) Uniformly undersampled Cartesian trajectory with an acceleration factor of R=3 produce coherent aliasing artifacts in the image domain. (c) Variable-density Cartesian sampling and the corresponding incoherent imaging artifacts. (d) Radial data can be undersampled by skipping radial spokes with streaking artifacts in the reconstructed image. (e) Spiral k-space undersampled by skipping spiral arms, which produces incoherent swirling artifacts [32].	14
2.10	Partial Fourier.	15
2.11	Parallel Imaging: SENSE reconstruction.	16
2.12	Compressed Sensing [58].	17
2.13	Deep neural networks for accelerating MRI acquisition.	18
2.14	Cine imaging: (a) Axial plane. (b) Vertical long-axis plane. (c) Horizontal long-axis plane. (d) Short-axis plane. (e) Four-chamber plane [90].	20
2.15	Myocardial Late Gadolinium Enhancement (LGE) sequence.	21
2.16	Myocardial T_1 Mapping.	23

- 3.1 CNet pipeline: (a) 3D MR data from 32 coils acquired in the k-space, $K(k_x, k_y, k_z, 32)$, with pseudorandom under-sampling pattern. Multi-coil data is transformed to the image domain by 3D inverse fast Fourier transform (IFFT), then combined using B1 weighted reconstruction and coil sensitivity information to produce a single 3D complex data volume in the image domain, $I(I_x, I_y, I_z)$. (b) Each slice is fed into cascaded complex convolutional layers with kernel size 3×3 with contractive and expansive paths. The contractive path includes convolutional layers with different kernel amounts (i.e. 64, 128, and 256) interleaved with 3 under-sampling stages using complex convolutional layers with a stride of 2 to extract high-level features at multi-resolution levels. The feature maps passed through a bottleneck convolutional layer of 512. The expansive path gradually restores the original resolution of the data through three upsampling stages; in each, the analogous feature maps from both paths (i.e. contractive and expansive) at each level are concatenated. Complex convolutional layers with a similar number of kernels as the contractive path was applied at each level. This network results in complex-valued 2D image at the last layer. The magnitude of the complex-valued output is compared to the LOST-reconstructed reference magnitude image to calculate the mean squared error (MSE) loss. All convolutional layers are followed by radial batch normalization and complex ReLU, with the exception of the last convolutional layer. 31
- 3.2 Numerical example of (a) Real-valued and (b) Complex-valued convolution operations. Complex-valued convolution operation is calculated by four real-valued convolution operations. In complex convolution, the input image (I), kernel (k), and output feature maps (f) are complex values with real and imaginary components. The real component of the output maps is described as $\Re(f) = \Re(k) \otimes \Re(I) - \Im(k) \otimes \Im(I)$, and imaginary components as $\Im(f) = \Re(k) \otimes \Im(I) + \Im(k) \otimes \Re(I)$, where \otimes represents convolution operations. 32

3.3 Effect of complex and radial data/batch normalization (BN) methods on complex data samples. Probability distribution function (PDF) of the real, imaginary, and magnitude of the original complex image (a, d, and g, respectively), result of complex BN on the original data sample (b, e, and h, respectively), and result of the proposed radial BN on the original data sample (c, f, and i, respectively). The magnitude PDF resulted from complex BN has substantially altered shape than that of the original data or radial BN result PDFs (3rd row), due to shifting the real and imaginary distributions of the data separately to have zero mean; where pixels with small values change its polarity (orange curve in h). The fourth row shows the corresponding 2D magnitude images of another original data sample and its corresponding complex and radial BNed data (j, k, and l, respectively). (m) Random complex data sample points represented by magnitude and phase in the polar coordinates. Performing the complex BN on this data sample resulted in distorted phase information (magenta circles in n) due to shifting the real and imaginary distributions independently to zero mean. Radial BN maintained the phase information and the relative differences in magnitude between the data points similar to that of the original data (o). 33

3.4 Four LGE images from different patients reconstructed using realNet, CNet and LOST with different acceleration rates $R_p=3$ and $R_p=5$. Arrows indicate areas of scar. 35

3.5 LOST, CNet, and realNet-reconstructed images of two patients (first and third rows). The corresponding error maps of CNet and realNet –reconstructed images w.r.t. the LOST reference are shown (second and fourth rows). 36

3.6 Representative LGE image at prospective acceleration rate $R_p=3$ and retrospective acceleration rates $R_r=4, 5,$ and 6 reconstructed by CNet compared to LOST reference, realNet and zero-filled images at each acceleration rate. Image quality is restored with minimal noise and blurring artifacts in CNet-reconstructed images similar to that of the reference images. Scar-blood contrast is also maintained at higher acceleration rates. 37

3.7 Representative LGE image at prospective acceleration rate $R_p=5$ and retrospective acceleration rates $R_r=6, 7,$ and 8 reconstructed by CNet compared to LOST reference, realNet and zero-filled images at each acceleration rate. Image quality is restored with minimal noise and blurring artifacts in CNet-reconstructed images similar to that of the reference images. Scar-blood contrast is also maintained at higher acceleration rates. 38

3.8 Analysis of CNet network performance: (a) structure similarity index measure (SSIM) and (b) mean squared error (MSE) at all epochs of the training and testing phases in the prospective (i.e. D0) and retrospective (i.e. D1, D2, and D3) under-sampled datasets. 39

3.9 Quantitative analysis of scar percentage: (a) correlation of per-slice scar percentage between CNet and LOST, (b) Bland-Altman plot of differences in per-slice scar percentage between CNet and LOST w.r.t the average scar percentage of the two methods, (c) correlation of the per-patient scar percentage between CNet and LOST, and (d) Error of per-patient scar percentage calculated from CNet-reconstructed images w.r.t LOST in the prospective (i.e. D0) and retrospective under-sampled datasets (i.e. D1, D2, and D3). 40

3.10 (Figure S1) RealNet architecture. Real and imaginary components of complex image data are fed as 2-channel input into real-valued convolutional layers with kernel size 3×3 with contractive and expansive paths. The contractive path includes convolutional layers of different kernel amounts (i.e. 128, 256, and 320) interleaved with 3 under-sampling stages using a convolutional layers with a stride =2 to extract high-level features at multi-resolution levels. The feature maps passed through a bottleneck convolutional layer of 640 kernels. The expansive path gradually restores the original resolution of the data through three upsampling stages; in each, the analogous feature maps from both contractive and expansive paths at each level are concatenated. Real-valued convolutional layers with a similar number of kernels in the contractive path are applied at each level. The network output is a single channel magnitude image. All convolutional layers are followed by batch normalization and ReLU, with the exception of the last convolutional layer. 42

3.11 (Figure S2) ResNet architecture. The complex-valued input image is fed into an input complex convolutional layer of 64 7×7 features. Five residual blocks are deployed with 64, 128, 256, 128, and 64 3×3 kernels, respectively. The processed feature maps are combined at output layer of 1 7×7 complex convolutional kernels to generate complex artifact-free image at the network output. Radial batch normalization and complex ReLU are applied after each convolutional layer. 42

3.12 (Figure S3) Mean squared error (MSE) for CNet in (a) training and (b) testing datasets with and without radial batch normalization layers. Radial BN accelerates and stabilizes CNet convergence. 43

3.13 (Figure S4) Representative feature maps for the same image after applying the kernels of the first complex convolutional layer: (a) magnitude, and (b) the corresponding phase part of each feature map. 43

4.1 Proposed multi-domain convolutional neural network (MD-CNN) pipeline. K-space data from N_c coils acquired with radial trajectories are gridded onto the cartesian grid using NUFFT. To reconstruct the frame (red), multi-coil 2D k-space data from N_{tw} adjacent time frames (yellow) are fed into the MD-CNN. The output of the MD-CNN is a coil-combined reconstructed image for the target frame. MD-CNN consists of two subnetworks: k-space and image-domain. The k-space subnetwork takes complex-valued 2D k-space input data of size (N_c, N_{tw}, N_x, N_y) to be processed by two identical residual blocks. Each block consists of three complex convolutional layers with 3D kernels of size $(3 \times 5 \times 5)$. Each convolutional layer is followed by a complex rectified linear unit (XReLU) for activation. The resulting k-space data is transformed into the image domain by inverse Fast Fourier Transform (IFFT). In the image subnetwork, data are fed into two convolutional layers with 3D kernels of size $(3 \times 3 \times 3)$ to exploit spatio-temporal correlations. The time dimension in the resulting 3D feature maps are flattened into channels to produce 2D feature maps of size (N_c, N_{tw}, N_x, N_y) . A 2D U-net is then used to process the 2D feature maps from N_c coils and N_{tw} frames to reconstruct a coil-combined reconstructed image. 50

4.2 Radial undersampling using uniform-angle rotating radial trajectories. (a) an undersampled uniform radial trajectory of 14 spokes is selected from the acquired highly-sampled radial data (196 spokes). The radial trajectory in a frame p is rotated with an angle $\theta_p = \frac{p\pi}{N_v N_{tw}}$, where N_v is the number of views per frame (e.g. 14 spokes), and N_{tw} is the number of neighboring time frames (e.g. 7 frames). (b) the undersampled radial lines from N_{tw} consecutive time frames have a uniform angular-spacing trajectory that allow optimal k-space coverage for data sharing. 51

4.3	Performance of the k-space subnetwork in two subjects. The k-space data is shown at different stages of the network: the gridded input k-space, after the 1 st and 2 nd residual blocks of the k-space subnetwork, the k-space of MD-CNN reconstruction, and the k-space of the reference image (rows 1 and 3). The corresponding images are also shown (rows 2 and 4). K-space gaps are gradually filled and the corresponding streaking artifacts of input images are suppressed after k-space interpolation in 1 st and 2 nd k-space blocks (columns 2 and 3). The final MD-CNN reconstructed images have further reduced artifacts and improved image quality similar to the reference images. The k-space of the input, k-space block-1, and kspace block-2 are taken from a single coil. All k-space data are presented on a logarithmic scale.	54
4.4	Representative reconstructions by NUFFT, kt-RASPS, U-net, and MD-CNN compared to the reference images for two subjects at end-diastolic and end-systolic phases, as well as x-t plots across all time frames.	55
4.5	Representative reconstruction by MD-CNN at different undersampling rates: 14, 16, and 20 spokes per frame compared to reference image. X-t plots of the reconstructed images at each undersampling rate (bottom row) shows the temporal fidelity across all time frames. Temporal fidelity increases as undersampling decreases (magenta arrows)..	55
4.6	Quantification of the left ventricular (LV) edge sharpness at six myocardial segments in GRAS, MD-CNN, and reference images. (a) Sample reconstructed images at end-systole by the three methods (kt-RASPS, MD-CNN, and Reference) showing the six segments at which LV sharpness was quantified and the intensity profiles corresponding to each segment of the sample images. (b) The bull's eye plot shows the value of the quantified LV edge sharpness at the six different segments of the myocardium with mean±SD calculated over all time frames of the testing dataset.	56
4.7	Bland-Altman plots showing inter-observer agreement of three comparisons: Reader#1 vs. Reader#2, Reader#2 vs. Reader#3, and Reader#1 vs. Reader#3 of the extracted LV myocardial areas in kt-RASPS, MD-CNN, and reference images. Biases and limits of agreement for each comparison are reported in Table 4.4.	58
4.8	(Figure S1) Mean squared error (MSE) for MD-CNN images in the training and testing datasets at each of the 250 training epochs.	61

4.9 (Figure S2) Sample reconstructed images at end-systole by the three methods (kt-RASPS, MD-CNN, and Reference) showing the six segments at which LV sharpness was quantified and the intensity profiles corresponding to each segment of the sample images. 62

5.1 MOLLI-5(3)3 sequence (a) and associated signal recovery (b): two look-locker inversion pulses are performed to acquire eight T_1 -weighted images with a recovery period of 3 heartbeats between look-lockers. In MyoMapNet, images collected after the first inversion pulse are used for estimating the T_1 values. 66

5.2 MOLLI-4(1)3(1)2 sequence (a) and associated signal recovery (b): three look-locker inversion pulses are performed to acquire nine T_1 -weighted images with a recovery period of one heartbeat between look-lockers. In MyoMapNet, images collected after the first look-locker are used for estimating the T_1 values. 67

5.3 MyoMapNet architecture: MyoMapNet uses a fully-connected neural network for estimating pixel-wise T_1 values from T_1 -weighted images collected after a single look-locker inversion pulse (i.e. the first 5 images of MOLLI-5(3)3 or first 4 images of MOLLI-4(1)3(1)2). For each voxel, the signal values from 5 T_1 -weighted images are concatenated with their corresponding look-locker times and used as the network input (i.e. 10×1) for native T_1 mapping. The input values are fed to a fully-connected network with 5 hidden layers with 400, 400, 200, 200, and 100 nodes each layer, respectively. The output is the estimated T_1 value at each voxel. 68

5.4 Flowchart for MyoMapNet training, testing, and parameter-tuning validation splits in the native, post-contrast, and simulated T_1 datasets. ECV values were evaluated in 75 subjects who had both native and post-contrast T_1 data available in the testing dataset. 71

5.5 Example native T_1 maps with left ventricular myocardial segmentation used for analyzing T_1 estimations by MyoMapNet, MOLLI-5, and standard MOLLI-5(3)3. 71

5.6 Bland-Altman plots showing the mean difference and 95% limits of agreement between the simulated T_1 values by the MOLLI-5 vs. MOLLI-5(3)3 (left column) and MyoMapNet vs. MOLLI-5(3)3 (right column) for SNR of 100, 40, and 20. MOLLI-5 yields a systematic error in T_1 estimations, which is corrected in MyoMapNet. 72

- 5.7 Native T_1 maps from four patients, reconstructed using MOLLI-5 (using only 5 T_1 weighted images with 3-parameter fitting), MyoMapNet, and MOLLI-5(3)3 with a 3-parameter fitting model. MyoMapNet yield maps with more homogenous signal compared to MOLLI-5. 73
- 5.8 Bland-Altman plots showing the mean difference and 95% limits of agreement for global native, post-contrast T_1 , and ECV for the abbreviated MOLLI-5/MOLLI-4 vs. standard MOLLI-5(3)3/MOLLI-4(1)3(1)2 (left column) and MyoMapNet vs. standard MOLLI-5(3)3/MOLLI-4(1)3(1)2 (right column). Each dot represents the values calculated from one patient. 75
- 5.9 Bland-Altman plots showing per slice analysis of the mean difference and 95% limits of agreement for native, post-contrast T_1 , and ECV for the abbreviated MOLLI-5/MOLLI-4 vs. standard MOLLI-5(3)3/MOLLI-4(1)3(1)2 (left column) and MyoMapNet vs. standard MOLLI-5(3)3/MOLLI-4(1)3(1)2 (right column). Each dot represents the values calculated from one slice. 76
- 5.10 Myocardial T_1 maps calculated using MOLLI-5 with a 3-parameter fitting model, MyoMapNet, and MOLLI-5(3)3, demonstrating the impact of respiratory motion (black arrows) in two subjects. The epicardial delineation of image #1 was copied to all other T_1 -weighted images to show the degree of motion between images. Both subjects were instructed to hold their breath during the scan. 77

LIST OF TABLES

3.1	Mean-squared error (MSE) and structural-similarity index (SSIM) quantities for zero-filled, CNet and real-valued network (realNet) images, in the prospective (D0) and retrospective under-sampled (D1, D2, and D3) datasets.	39
3.2	Qualitative assessment (per-patient) of overall image quality, presence of LGE scars, and the preferred method for diagnosis of LGE images reconstructed using LOST, CNet, and realNet methods from three readers.	39
4.1	Quantitative assessment of image quality by mean-squared error (MSE), structural-similarity index measure (SSIM), and LV myocardial sharpness for kt-RASPS, 3D U-net and MD-CNN reconstructed images with respect to the reference. All values are reported as mean \pm SD.	56
4.2	Qualitative assessment of LV border sharpness at end-diastolic and end-systolic cardiac phases, temporal fidelity of myocardial wall motion, and residual artifacts in kt-RASPS, MD-CNN, and reference images.	57
4.3	DICE index and percentage error of LV myocardial and endocardial areas at end-diastolic and end-systolic phases extracted from kt-RASPS and MD-CNN images with respect to reference images.	57
4.4	(Table S2) Biases and limits of agreement of the Bland-Altman plots for inter-observer agreement of 3 comparisons: Reader#1 vs. Reader#2, Reader#2 vs. Reader#3, and Reader#1 vs. Reader#3 of the extracted LV myocardial areas in kt-RASPS, MD-CNN, and reference images.	61
5.1	Number of parameters at different MyoMapNet depth (3, 5, and 7 layers) and network size (S=1, 2, and 3).	69
5.2	Mean difference (\pm STD) in T_1 values between MyoMapNet and MOLLI-5(3)3 at different loss functions (MSE, and MAE), network depth (3, 5, and 7 layers) and network size (S=1, 2, and 3).	74
5.3	Mean difference (\pm STD) in T_1 values between MyoMapNet and MOLLI-5(3)3 at different loss functions (MSE, and MAE), network depth (3, 5, and 7 layers) and network size (S=1, 2, and 3).	78

LIST OF PUBLICATIONS

1. **Hossam El-Rewaify**, Ahmed S Fahmy, Farhad Pashakhanloo, Xiaoying Cai, Selcuk Kucukseymen, Ibolya Csecs, Ulf Neisius, Hassan Haji-Valizadeh, Bjoern Menze, Reza Nezafat, "*Multi-Domain Convolutional Neural Network (MD-CNN) For Radial Reconstruction of Dynamic Cardiac MRI*," *Magnetic Resonance in Medicine*, 2021;85:1195–1208.
2. **Hossam El-Rewaify**, Ulf Neisius, Jennifer Mancio, Selcuk Kucukseymen, Jennifer Rodriguez, Amanda Paskavitz, Bjoern Menze, Reza Nezafat, "*Deep Complex Convolutional Network for Fast Reconstruction of 3D Late Gadolinium Enhancement Cardiac MRI*," *NMR in Biomedicine*, 2020;33(7):e4312.
3. **Hossam El-Rewaify**, Ulf Neisius, Shiro Nakamori, Long Ngo, Jennifer Rodriguez, Warren J. Manning, Reza Nezafat, "*Characterization of interstitial diffuse fibrosis patterns using texture analysis of myocardial native T1 mapping*," *Plos One*, 2020;15:e0233694.
4. **Hossam El-Rewaify***, Ulf Neisius*, Shiro Nakamori, Jennifer Rodriguez, Warren J. Manning, Reza Nezafat "*Radiomic analysis of native myocardial T1 imaging discriminates between hypertensive heart disease and hypertrophic cardiomyopathy*," *JACC: Cardiovascular Imaging*, 2019;12:1946–1954.
*Authors contributed equally.
5. **Hossam El-Rewaify***, Ulf Neisius*, Selcuk Kucukseymen, Connie Tsao, Jennifer Mancio, Shiro Nakamori, Warren Manning, Reza Nezafat, "*Texture signatures of native myocardial T1 as novel imaging markers for identification of hypertrophic cardiomyopathy patients without scar*," *Journal of Magnetic Resonance Imaging*, 2020;52:906–919.
*Authors contributed equally.
6. **Hossam El-Rewaify**, Maryam Nezafat, Jihye Jang, Shiro Nakamori, Ahmed S Fahmy, Reza Nezafat, "*Non-rigid Active Shape Model-based Registration Framework for Motion Correction of Cardiac T1 Mapping*," *Magnetic Resonance in Medicine*, 2018 Aug;80(2):780-791.
7. **Hossam El-Rewaify**, Ahmed S. Fahmy, Ayman M. Khalifa, El-Sayed H. Ibrahim, "*Multiple two-dimensional active shape model framework for right ventricular segmentation*," *Magnetic Resonance Imaging*, 2022;85:177-185.
8. Rui Guo, **Hossam El-Rewaify**, Salah Assana, Xiaoying Cai, Amine Amyar, Kelvin Chow, Xiaoming Bi, Tuyen Yankama, Julia Cirillo, Patrick Pierce, Beth Goddu, Long Ngo, Reza Nezafat "*Accelerated Cardiac T1 Mapping in Four Heartbeats with Inline MyoMapNet: A*

- Deep Learning-Based T1 Estimation Approach*" Journal of Cardiovascular Magnetic Resonance, 2022.
9. Maryam Nezafat, **Hossam El-Rewaidy**, Selcuk Kucukseymen, Thomas Hauser, Ahmed S Fahmy, "*Deep Convolution Neural Networks Based Artifact Suppression in Under-sampled Radial Acquisitions of Myocardial T1 mapping images,*" Physics in Medicine and Biology, 2020;65:225024.
 10. Jihye Jang, **Hossam El-Rewaidy**, Long H Ngo, Jennifer Mancio, Ibolya Csecs, Jennifer Rodriguez, Patrick Pierce, Beth Goddu, Ulf Neisius, Warren Manning, Reza Nezafat. "*Sensitivity of Myocardial Radiomic Features to Imaging Parameters in Cardiac MR Imaging,*" Journal of Magnetic Resonance Imaging, 2021.
 11. Ahmed S. Fahmy, **Hossam El-Rewaidy**, Maryam Nezafat, Shiro Nakamori, Reza Nezafat, "*Automated Analysis of Myocardial Native T1 Mapping Images Using Fully Convolutional Neural Networks,*" Journal of Cardiovascular Magnetic Resonance, 2019;21:7.
 12. Shiro Nakamori, Ahmed Fahmy, Jihye Jang, **Hossam El-Rewaidy**, Ulf Neisius, Jennifer Rodriguez, Sophie Berg, Beth Goddu, Patrick Pierce, Thomas Hauser, Long H. Ngo, Warren J Manning, Reza Nezafat, "*Changes in Myocardial T1 and T2 After Supine Exercise Stress in Healthy and Ischemic Myocardium: A Pilot Study,*" JACC: Cardiovascular Imaging, 2020;13:667-680.
 13. Ulf Neisius, Lana Myerson, Ahmed S. Fahmy, Shiro Nakamori, **Hossam El-Rewaidy**, Gargi Joshi, Chong Duan, Warren J. Manning, and Reza Nezafat. "*Cardiovascular magnetic resonance feature tracking strain analysis for discrimination between hypertensive heart disease and hypertrophic cardiomyopathy,*" PloS one, 2019;14(8):e0221061
 14. Burhaneddin Yaman, Chetan Shenoy, Zilin Deng, Steen Moeller, **Hossam El-Rewaidy**, Reza Nezafat, Mehmet Akcakaya, "*Self-Supervised Physics-Guided Deep Learning Reconstruction for High-Resolution 3D LGE CMR,*" IEEE International Symposium on Biomedical Imaging (ISBI), Nice, France, 2021.
 15. **Hossam El-Rewaidy**, Rui Guo, Amanda Paskavitz, Tuyen Yankama, Long Ngo, Bjoern Menze, Reza Nezafat, "*MyoMapNet: Accelerated Modified Look-Locker Inversion Recovery Myocardial T1 Mapping via Neural Networks,*" Magnetic Resonance in Medicine, 2021. (*submitted*)